Numerical Study of Liquid Fuel Atomization, Evaporation and Combustion

Jian WEN

2022

Numerical Study of Liquid Fuel Atomization, Evaporation and Combustion

Jian WEN

A thesis submitted to Kyoto University
for the degree of Doctor of Philosophy in Engineering

2022

Acknowledgments

The research described in this thesis was carried out in the Department of Mechanical Engineering and Science at Kyoto University's Graduate School of Engineering, under the supervision of Professor Ryoichi Kurose. The author would like to express his most heartfelt gratitude to the professor for all the helpful suggestions to his study, and constant encouragement.

The author gives his thanks to Professor Hideshi Hanazaki and Professor Hiroshi Iwai for many valuable and critical comments to his study.

The author shows his appreciation to Professor Ryoichi Kurose from the bottom of his heart for many useful discussions, comments and suggestions for his research, and for the top-notch education.

The author shows his appreciation to Professor Mitsuhiro Matsumoto for many useful discussions for his study.

The author is deeply grateful to Prof. Yong Hu of Sichuan University for many useful discussions, comments and suggestions for his study, and encouragement.

The author thanks Prof. Abhishek Lakshman Pillai, Dr. Zhicheng Yuan, Mr. Reo Kai, Mr. Akihiro Nakanishi, Mr. Jun Nagao, Mr. Hiroki Muramatsu, Mr. Kenya Kitada and the past and present members of Thermal Science and Engineering Laboratory for their help in his research.

The author thanks Mr. Takayuki Nishiie and Mr. Jun Iino of Numerical Flow Designing Co., Ltd (NuFD) for their useful advice and help in his research.

The author thanks Prof. Assaad Masri of the University of Sydney for his useful advice and help in his research.

This research was partially supported by MEXT (Ministry of Education, Culture, Sports, Science and Technology) as "Program for Promoting Researches on the Supercomputer Fugaku" (Digital Twins of Real World's Clean Energy Systems with Integrated Utilization of Super-simulation and AI) and by JSPS KAKENHI Grant Number 19H02076. The author is also grateful to CSC (China Scholarship Council) for the financial support provided through the CSC Scholarship Program.

Finally, the author would like to express the deepest appreciation to his parents for the infinite support and constant affection.

Contents

Chapter 1

Introduction

1.1 Background and motivation for this study

The Paris Agreement has achieved a worldwide acceptance that greenhouse gases such as carbon dioxide (CO_2) have to be limited and balanced to relax the rise of global temperature due to the increased effects of global warming and the energy crisis. Therefore, serious environmental regulations have been implemented by each member country to achieve carbon neutrality. Compared to carbon offsetting such as tree planting, reducing CO_2 emissions is more efficient, for which renewable energy sources such as hydro, wind, and solar are promising. However, the supply of the renewable energy tends to be unstable, as it is easily affected by the environment and climate. Although nuclear power is an alternate solution, the issues of radioactive waste disposal and political factors such as Japan limit it. Hence, it is very difficult to employ such applications, and reducing CO_2 emissions from conventional energy generators such as power plants and engines is still effective. Therefore, it is important especially for electric, automobile and aviation companies to achieve higher combustion efficiency. The combustion configurations have various scenarios based on the fuel state, such as coal, gasoline, diesel, and biofuels. Spray combustion is among the widest applications of combustion configurations used in gas turbines, automobile engines, aircraft engines, rocket engines and so on, which includes extremely complex physical phenomena, starting from liquid fuel at-

omization along with droplet evaporation, and evaporated fuel-air mixing, ending up in combustion. Therefore, the complexity involved makes it difficult to clarify the detailed mechanism and relevant models underlying spray atomization and combustion.

As mentioned by Masri [1], studies on spray combustion are generally classified as dense and dilute spray conditions. For the dense spray condition which is often observed in or just after the atomization process, many generated droplets make it difficult for experimental diagnostics to acquire sufficient information [2] and for numerical simulations to be validated by comparing with the reliable experimental data, making the behavior unclear. Hence, the dense spray combustion scene remains vague. For the dilute spray condition, on the other hand, generated droplets are easily captured using advanced experimental diagnostics and then the behavior is getting clear [3–38]. In the numerical simulations for the dilute spray condition, fuel sprays are regarded as parcels and then easily solved by using the Lagrangian approach to consider the interaction with the surrounding gas phase without considering the atomization. However, this Lagrangian approach has difficulty in providing the initial droplet size distribution near the nozzle exit owing to the abundance of interplayed phenomena, namely, the process of spray atomization, including primary breakup, secondary breakup, and droplet coalescence/collision [39–47].

To effectively investigate the spray combustion behavior both in dense and dilute spray conditions, Masri et al. [72–74] at the University of Sydney recently designed a canonical platform that can supply various spray inlet conditions, which is called the Sydney Piloted Needle Burner (hereinafter referred to as the Sydney Burner) to stabilize repeatable turbulent spray flames by placing two concentric tubes within the pilot annulus. By varying the recess distance, which refers to the distance between the liquid fuel jet nozzle and the pilot outlet, different types of sprays can be reproduced. However, there have been no attempts to use a numerical simulation to couple the combustion process with the beforehand atomization process so far.

For aircraft engines, a crossflow-type spray [50], whose mechanism is quite different from that of a straight-jet-type spray [51] in automobile internal combustion engines, is

commonly used. The direction of the airstream is perpendicular to the injected liquid jet such that the atomization process involves a large mass, momentum, and energy exchange between the liquid and gas phases, leading to large deformation of the liquid-gas interface and generation of droplets. Despite the difficulties in observing the atomization process in the vicinity of the fuel nozzle because of the limitations of optical methods, where many droplets are generated and block the light paths except for the windward side and sides of the liquid jet, a number of researchers have attempted to investigate the liquid jet trajectory [42, 52, 53], breakup mode associated with aerodynamic Weber number [52, 54, 55], and downstream droplet behavior [56, 57]. Nevertheless, the atomization behavior in the vicinity of the fuel nozzle has not been fully understood yet especially under the real pressure conditions in aircraft engines around 2.0–3.0 MPa, due to the difficulties of the experiments.

To understand the atomization process of spray combustion, especially in such crossflow, simulation studies have become popular because of the extremely enhanced computational ability in this age. Detailed numerical simulation has become a valuable method for investigating liquid jet atomization physics owing to its first-principle nature. Furthermore, the numerical simulation enables the study of the dense spray region, which presents the difficulty of optical experimental measurements. During the atomization process, the deformation of the liquid–gas interface has a significant influence on the liquid jet breakup and droplet generation. In general, the volume of fluid (VOF) method [58] and level-set method [59] are widely used in numerical simulations to capture the liquid–gas interface. However, both methods have a drawback in that these methods are strongly dependent on the computational grid size, especially for capturing the generation process of small droplets, which denotes a much higher computational cost. Therefore, an alternative method called Eulerian-Lagrangian (E-L) method, in which Eulerian droplets are transformed into Lagrangian droplets, has been developed to reduce the computational cost [60, 61].

In previous simulation studies on crossflow atomization, the aerodynamic Weber number [62, 63, 65], liquid–gas momentum flux ratio, liquid–gas density ratio [41, 43,

66, 67], and liquid–gas viscosity ratio [63] have been proven significant factors for spray atomization. The simulation results are generally in good agreement with the experimental results [50, 52, 53]. However, these studies have seldom considered the evaporation effects of liquid fuels. Recently, Umemura et al. [44] investigated the atomization process of a straight liquid jet, considering evaporation and combustion. In addition, Barata [68] studied the evaporating Lagrangian droplet behaviors in crossflow. Li et al. [69] investigated the evaporation process of droplets in the downstream region in crossflow, neglecting the surface evaporation of liquid jet owing to its larger volume–area ratio compared to the droplets, using the E-L method. However, no study has investigated the atomization–evaporation process of liquid fuel jets in crossflows, especially in the vicinity of the fuel nozzle, using the E-L method. In addition, Song et al. [53] found that the conclusions of studies such as that of liquid jet trajectory and droplet size, which are constrained to low ambient pressure conditions, are questionable by investigating the main characteristics of liquid jet atomization in crossflows at an elevated ambient pressure. Therefore, a reliable model of the atomization process in relevant engine applications is urgently needed, which could be investigated via numerical simulation.

The liquid jet atomization process is considered to affect the combustion instability, which poses primary technical challenges for engine design because of its capacity to cause catastrophic damage to the combustor and other engine components [23]. In addition, the thermoacoustic induced by unstable combustion could also affect the liquid jet atomization process, providing positive or negative feedback to dampen or amplify the combustion instability. Therefore, a comprehensive understanding of the complex coupled process of spray atomization and combustion could be an effective method for controlling combustion instability [47]. Research on crossflow atomization in the context of oscillating inflow conditions is generally limited to experimental work because the numerical simulation requires a much higher computational cost. However, in experimental studies, different phenomena were observed in different groups. Bunce et al. [70] pointed out the distinctive variance of spray coverage at different phases of the oscillation, as well as the frequency dependence on the crossflow oscillation. In addi-

tion, Song et al. [57, 71] conducted several experimental studies on spray atomization in crossflows by adopting different crossflow frequencies, deriving completely different conclusions from those of Bunce et al. [70]. Therefore, the detailed mechanism of the interaction between atomization and crossflow oscillation in the dense spray area illustrates a complex phenomenon and vague understanding due to the complexity of its flow field and the limitations of experimental measurements. Regarding the numerical simulation, the accurate prediction of such a complicated atomization pattern is still a challenge for the current computational models, although there are few numerical simulations [47] investigating the influence of the oscillating airflow conditions on the atomization–evaporation process in crossflows by applying atomization models.

The purpose of the present study is, therefore, to investigate the mechanism of spray combustion coupled with the beforehand liquid jet atomization process through numerical simulations. First, a detailed numerical simulation of the atomization–evaporation process of a liquid fuel jet in several different steady crossflows under elevated ambient pressure using an E-L method is performed. Thereafter, the liquid jet trajectory, primary breakup behavior, vortex morphology, droplet size distributions, and evaporation effects under different breakup mode regimes, that is, different aerodynamic Weber number conditions, are investigated. Second, a detailed numerical simulation of the atomization–evaporation process of a liquid fuel jet in an oscillating crossflow under an elevated ambient pressure using an E-L method is performed, and the liquid jet trajectory, vortex development, droplet, and fuel vapor distributions are investigated in a series of time sequences in comparison to those in a steady crossflow to clarify the effects of air flow oscillation, resulting from combustion instability, on the atomization–evaporation process. Finally, a large eddy simulation (LES) flamelet modeling of a turbulent dense spray flame coupled with a detailed high-resolution VOF simulation of liquid fuel atomization is performed, and the liquid jet atomization behavior, droplet spatial distribution, and breakup length of atomization are investigated in the atomization computation. Finally, the gas temperature and droplet size distributions are investigated in comparison with the experimental data in the combustion computation.

1.2 Thesis outline

This thesis consists of five chapters.

Chapter 1, the present chapter, describes the background, motivation, purpose for the study, and outline of this thesis.

Chapter 2 describes the characteristics of the atomization–evaporation process of a liquid fuel jet in several different steady crossflows under elevated ambient pressure. The liquid jet trajectory, primary breakup behavior, vortex development and morphology, droplet size distribution, and evaporation effects under different breakup mode regimes (i.e., different aerodynamic Weber number conditions) are investigated using a detailed numerical simulation. As the liquid of the fuel jet, kerosene is used. As the gas of crossflow, air is used under an elevated ambient pressure of 3.0 MPa, which is close to the practical conditions of aircraft engines [23]. For the calculation of the atomization–evaporation process, a coupled level set and volume of fluid (CLSVOF) method is used to capture the liquid–gas interface. A continuum surface force (CSF) model proposed by Brackbill et al. [75] is used to calculate the surface tension at the liquid–gas interface. An E-L tagging method that could transform Eulerian droplets into Lagrangian droplets, proposed by Herrmann [41] and Zuzio et al. [61], is utilized to reduce the computational cost. A non-equilibrium Langmuir-Knudsen evaporation model is used to consider the evaporation effects of the transformed Lagrangian droplets.

Chapter 3 describes the characteristics of the atomization–evaporation process of a liquid fuel jet in an oscillating crossflow under elevated ambient pressure in comparison to those in a steady crossflow. The liquid jet trajectory, vortex development and morphology, droplet size, and fuel vapor distributions in the oscillating crossflow are investigated using a detailed numerical simulation. For the oscillating crossflow, the oscillation frequency is set to 500 Hz, which is similar to a previous study on combustion instability [23]. The physical properties of the liquid fuel and carrier crossflow are the same as those in the steady crossflow, and so are the numerical simulation methods and settings.

Chapter 4 describes the characteristics of the atomization–combustion process of liq-

uid fuel jets in the configuration of Sydney Burner in comparison with the experimental data. Acetone and air in the atmospheric ambient pressure are used as the fuel and oxidizer, respectively. For the calculation of atomization, a high-resolution interface capturing (HRIC) scheme is implemented in the VOF method to capture the liquid–gas interface. For the calculation of combustion, a non-adiabatic flamelet/progress variable (NAFPV) approach is used to model the turbulence–chemistry interaction. For the coupling of the atomization–combustion computation, the atomization–combustion coupling (ACC) plane is used to save the output of the atomization computation (i.e., the profiles of transformed Lagrangian droplets and gas velocity) in a database and serve as inlet boundary conditions for the combustion computation.

Chapter 5 summarizes all the investigations carried out in this study and provides recommendations for possible future extensions of the present study.

References

[1] A. Masri. Turbulent combustion of sprays: from dilute to dense. *Combust. Sci. Tech.*, 188:1619–1639, 2016.

[2] M. Linne. Imaging in the optically dense regions of a spray: a review of developing techniques. *Prog. Energy Combust. Sci.*, 39:403–440, 2013.

[3] H. Chiu and T. Liu. Group combustion of liquid droplets. *Combust. Sci. Technol.*, 17:127–142, 1997.

[4] A. Umemura. Interactive droplet vaporization and combustion: approach from asymptotics. *Prog. Energy Combust. Sci.*, 20:325–372, 1994.

[5] S. Li. Spray stagnation flames. *Prog. Energy Combust. Sci.*, 23:303–347, 1997.

[6] E. Gutheil and W. Sirignano. Counterflow spray combustion modeling with detailed transport and detailed chemistry. *Combust. Flame*, 113:92–105, 1998.

[7] A. Klimenko and R. Bilger. Conditional moment closure for turbulent combustion. *Prog. Energy Combust. Sci.*, 25:25–62, 1999.

[8] V. Gopalakrishnan and J. Abraham. Effects of multicomponent diffusion on predicted ignition characteristics of a n-heptane diffusion flame. *Combust. Flame*, 136:557–566, 2004.

[9] H. Pitsch and M. Ihme. An unsteady/flamelet progress variable method for les of non-premixed turbulent combustion. *AIAA Paper*, 2005–557, 2005.

[10] J. Reveillon and L. Vervisch. Analysis of weakly turbulent dilute-spray flames and spray combustion regimes. *J. Fluid Mech.*, 537:317–347, 2005.

[11] M. Nakamura, F. Akamatsu, R. Kurose, and M. Katsuki. Combustion mechanism of liquid fuel spray in a gaseous flame. *Phys. Fluids*, 17:1–14, 2005.

[12] J. Reveillon and F. Demoulin. Evaporating droplets in turbulent reacting flows. *Proc. Combust. Inst.*, 31:2319–2326, 2007.

[13] H. Watanabe, R. Kurose, S. Huang, and F. Akamatsu. Characteristics of flamelets in spray flames formed in a laminar counterflow. *Combust. Flame*, 148:234–248, 2007.

[14] N. Abani, A. Munnannur, and R. Reitz. Reduction of numerical parameter dependencies in diesel spray models. *J. Eng. Gas Turb. Power*, 130:032809, 2008.

[15] Y. Baba and R. Kurose. Analysis and flametlet modelling for spray combustion. *J. Fluid. Mech.*, 612:45–79, 2008.

[16] M. Ihem and Y. See. Prediction of autoignition in a lifted methane/air flame using an unsteady flamelet/progress variable model. *Combust. Flame*, 157:1850–1862, 2010.

[17] R. Bilger. A mixture fraction framework for the theory and modeling of droplets and sprays. *Combust. Flame*, 158:191–202, 2011.

[18] K. Luo, H. Pitsch, M. Pai, and O. Desjardins. Direct numerical simulations and analysis of three-dimensional n-heptane spray flames in a model swirl combustor. *Proc. Combust. Inst.*, 33:2143–2152, 2011.

[19] M. Turner, S. Sazhin, J. Healey, C. Crua, and S. Martynov. A breakup model for transient diesel fuel sprays. *Fuel*, 97:288–305, 2012.

[20] C. Bajaj, M. Ameen, and J. Abraham. Evaluation of an unsteady flamelet progress variable model for autoignition and flame lift-off in diesel jets. *Combust. Sci. Tech.*, 185:454–472, 2013.

[21] S. Ukai, A. Kronenburg, and O. Stein. Les-cmc of a dilute acetone spray flame. *Proc. Combust. Inst.*, 34:1643–1650, 2013.

[22] S. De and S. Kim. Large eddy simulation of dilute reacting sprays: droplet evaporation and scalar mixing. *Combust. Flame*, 160:2048–2066, 2013.

[23] S. Tachibana, K. Saito, T. Yamamoto, M. Makida, T. Kitano, and R. Kurose. Experimental and numerical investigation of thermos-acoustic instability in a liquid-fuel aero-engine combustor at elevated pressure: validity of large-eddy simulation of spray combustion. *Combust. Flame*, 162:2621–2637, 2015.

[24] T. Kitano, K. Kaneko, R. Kurose, and S. Komori. Large-eddy simulations of gas- and liquid-fueled combustion instabilities in back-step flows. *Combust. Flame*, 170:63–78, 2016.

[25] L. Ma and D. Roekaerts. Numerical study of the multi-flame structure in spray combustion. *Proc. Combust. Inst.*, 36:2603–2613, 2017.

[26] B. Wang, A. Kronenburg, G. Tufano, and O. Stein. Fully resolved dns of droplet array combustion in turbulent convective flows and modelling for mixing field in inter-droplet space. *Combust. Flame*, 189:347–366, 2018.

[27] A. Pillai and R. Kurose. Combustion noise analysis of a turbulent spray flame using a hybrid dns/ape-rf approach. *Combust. Flame*, 200:168–191, 2019.

[28] Y. Hu and R. Kurose. Nonpremixed and premixed flamelets les of partially premixed spray flames using a two-phase transport equation of progress variable. *Combust. Flame*, 188:227–242, 2018.

[29] Y. Hu and R. Kurose. Partially premixed flamelet in les of acetone spray flames. *Proc. Combust. Inst.*, 37:3327–3334, 2019.

[30] Y. Hu, R. Kai, R. Kurose, E. Gutheil, and H. Olguin. Large eddy simulation of a partially pre-vaporized ethanol reacting spray using the multiphase dtf/flamelet model. *Int. J. Multiphas. Flow*, 125:103216, 2020.

[31] Y. Hardalupas, A. Taylor, and J. Whitelaw. Mass flux, mass fraction and concentration of liquid fuel in a swirl-stabilized flame. *Int. J. Multiphas. Flow*, 20:233–259, 1994.

[32] G. Chen and A. Gomes. Dilute laminar spray diffusion flames near the transition from group combustion to individual droplet burning. *Comsbut. Flame*, 110:392–404, 1997.

[33] M. Alden, J. Bood, Z. Li, and M. Richter. Visualization and understanding of combustion processes using spatially and temporally resolved laser diagnostic techniques. *Proc. Combust. Inst.*, 33:69–97, 2011.

[34] D. Cavaliere, J. Kariuki, and E. Mastorakos. A comparison of the blow-off behaviour of swirl-stabilized premixed, non-premixed and spray flames. *Flow Turb. Combust.*, 91:347–372, 2013.

[35] M. Chrigui, J. Gounder, A. Sadiki, J. Janicka, and A. Masri. Acetone droplet behavior in reacting and non reacting turbulent flow. *Flow Turb. Combust.*, 90:419–447, 2013.

[36] A. Verdier, J. Santiago, A. Vandel, G. Godard, G. Cabot, and B. Renou. Local extinction mechanisms analysis of spray jet flame using high speed diagnostics. *Combust. Flame*, 193:440–452, 2018.

[37] I. Mulla, G. Godard, G. Cabot, F. Grisch, and B. Renou. Quantitative imaging of nitric oxide concentration in a turbulent -heptane spray flame. *Combust. Flame*, 203:217–229, 2019.

[38] H. Luo, C. Wang, K. Nishida, Y. Ogata, and R. Chen. Characteristics of droplet behaviors after the end of injection in a high-pressure constant volume chamber. *Fuel*, 267:117291, 2020.

[39] D. Guildenbecher, C. Lopez-Rivera, and P. Sojka. Secondary atomization. *Exp. Fluids*, 46:371–402, 2009.

[40] X. Jiang, G. Siamas, K. Jagus, and T. Karyiannis. Physical modelling and advanced simulations of gas-liquid two-phase jet flows in atomization and sprays. *Prog. Energy Combust. Sci.*, 36:131–167, 2010.

[41] M. Herrmann. Detailed numerical simulations of the primary atomization of a turbulent liquid jet in crossflow. *J. Eng. Gas Turbines Power*, 132:061506, 2010.

[42] N. Ashgriz. Atomization of a liquid jet in a crossflow. *AIP Conf. Proc.*, 1440:33–46, 2012.

[43] X. Li and M. Soteriou. Detailed numerical simulation of liquid jet atomization in crossflow of increasing density. *Int. J. Multiphas. Flow*, 104:214–232, 2018.

[44] A. Umemura and J. Shinjo. Detailed sgs atomization model and its implementation to two-phase flow les. *Combust. Flame*, 195:232–252, 2018.

[45] T.-W. Lee, J. Park, and R. Kurose. Determination of the drop size during atomization and liquid jets in cross flows. *Atomiz. Sprays*, 28:241–254, 2018.

[46] J. Wen, Y. Hu, A. Nakanishi, and R. Kurose. Atomization and evaporation process of liquid fuel jets in crossflows: A numerical study using eulerian/lagrangian method. *Int. J. Multiphas. Flow*, 103331, 2020.

[47] A. Pillai, J. Nagao, R. Awane, and R. Kurose. Influences of liquid fuel atomization and flow rate fluctuations on spray combustion instabilities in a backward-facing step combustor. *Combust. Flame*, 220:337–356, 2020.

[48] T. Kitano, T. Tsuji, R. Kurose, and S. Komori. Effect of pressure oscillations on flashback characteristics in a turbulent channel flow. *Energy. Fuel*, 29:6815–6822, 2015.

[49] H. Watanabe, R. Kurose, S. Komori, and H. Pitsch. Effects of radiation on spray flame characteristics and soot formation. *Combust. Flame*, 152:2–13, 2008.

[50] P. Wu, K. Kirkendall, R. Fuller, and A. Nejad. Breakup processes of liquid jets in subsonic crossflows. *J. Propuls. Power*, 13:64–73, 1997.

[51] K. Brinckman, A. Hosangadi, V. Ahuja, S. Dash, and G. Feldman. A cfd methodology for liquid jet breakup and vaporization predictions in compressible flows. *AIAA ASME*, AIAA2008–1023, 2008.

[52] K. Sallam, C. Aalburg, and G. Faeth. Breakup of round nonturbulent liquid jets in gaseous crossflow. *AIAA J.*, 42:2529–2540, 2004.

[53] J. Song, C. Cain, and J. Lee. Liquid jets in subsonic air crossflow at elevated pressure. *J. Eng. Gas Turb. Power Trans Asme*, 041502, 2015.

[54] S. Freitag and C. Hassa. Spray characteristics of a kerosene jet in cross flow of air at elevated pressure. *ILASS2008*, ILASS08–12–1, 2008.

[55] S. Tambe, S. Jeng, H. Mongia, and G. Hsiao. Liquid jets in subsonic crossflow. *43rd AIAA ASME*, AIAA2005–731, 2005.

[56] P. Eriksson, R. Orbay, and J. Klingmann. Experimental investigations of a low weber liquid spray in air cross flow. *ICLASS2006*, ICLASS06–277, 2006.

[57] J. Song and J. Lee. Characterization of spray formed by liquid jet injected into oscillating air crossflow. *Proc. ASME Turb. Expo. 2015*, GT 2015–43726, 2015.

[58] C. Hirt and B. Nichols. Volume of fluid (vof) method for the dynamics of free boundaries. *J. Comput. Phys.*, 39:201–225, 1981.

[59] S. Osher and J. Sethian. Fronts propagating with curvature-dependent speed: Algorithms based on hamilton-jacobi formulations. *J. Comput. Phys.*, 79:12–49, 1988.

[60] M. Herrmann. A parallel eulerian interface tracking/lagrangian point particle multiscale coupling procedure. *J. Comput. Phys.*, 229:745–759, 2010.

[61] D. Zuzio, J. Estivalèzes, and B. DiPierro. An improved multiscale eulerian-lagrangian method for simulation of atomization process. *Comput. Fluids*, 176:285–301, 2018.

[62] X. Li and M. Soteriou. High fidelity simulation and analysis of liquid jet atomization in a gaseous crossflow at intermediate weber numbers. *Phys. Fluids*, 28:082101, 2016.

[63] X. Li, H. Gao, and M. Soteriou. Investigation of the impact of high liquid viscosity on jet atomization in crossflow via high-fidelity simulations. *Phys. Fluids*, 29:082103, 2017.

[64] R. Prakash, S. Jain, J. Lovett, B. Raghunandan, R. Ravikrishna, and G. Tomar. Detailed numerical simulation of atomization of a liquid jet in a swirling gas crossflow. *Atomiz. Sprays*, 2019.

[65] J. Leparoux, R. Mercier, V. Moureau, and H. Musaefendic. Primary atomization simulation applied to a jet in crossflow aeronautical injector with dynamic mesh adaption. *ICLASS2018*, 2018.

[66] S. Ghods. *Detailed numerical simulation of liquid jet in crossflow atomization with high density ratios*. PhD thesis, Arizona State University, Tempe, USA, 2013.

[67] M. Herrmann. The influence of density ratio on the primary atomization of a turbulent liquid jet in crossflow. *P. Combust. Inst.*, 33:2079–2088, 2011.

[68] J. Barata. Modelling of biofuel droplets dispersion and evaporation. *Renew. Energy*, 33:769–779, 2008.

[69] X. Li, M. Soteriou, M. Arienti, and M. Sussman. High-fidelity simulation of atomization and evaporation in a liquid jet in cross-flow. *49th AIAA Aerospace Sciences Meeting including the New Horizons Forum and Aerospace Exposition*, AIAA2011–99, 2011.

[70] K. Bunce, J. Lee, and D. Santavicca. Characterization of liquid jets-in-crossflow under high temperature, high velocity non-oscillating and oscillating flow conditions. *44th AIAA ASME*, AIAA2006–1225, 2006.

[71] J. Song, C. Ramasubramanian, and J. Lee. Response of liquid jet to modulated crossflow. *Atomiz. Sprays*, 24:129–154, 2014.

[72] J. Gounder, A. Kourmatzis, and A. Masri. Turbulent piloted dilute spray flames: flow fields and droplet dynamics. *Combust. Flame*, 159:3372–3397, 2012.

[73] L. M. Thomas, A. Lowe, A. Satija, and A. Masri. Five khz thermometry in turbulent spray flames using chirped-probe pulse femtosecond cars, part i: Processing and interference analysis. *Combust. Flame*, 200:405–416, 2019.

[74] A. Lowe, L. Thomas, A. Satija, R. Lucht, and A. Masri. Five khz thermometry in turbulent spray flames using chirped-probe pulse femtosecond cars, part ii: Structure of reaction zones. *Combust. Flame*, 200:417–432, 2019.

[75] J. Brackbill, D. Kothe, and C. Zemach. A continuum method for modeling surface tension. *J. Comput. Phys.*, 100:335–354, 1992.

Chapter 2

Volume of fluid (VOF) simulation of atomization and evaporation of liquid fuel jets in crossflows: Proposal of Eulerian-Lagrangian method

2.1 Introduction

In this chapter, the atomization-evaporation process of a liquid fuel jet in the vicinity of a fuel nozzle in several different steady crossflows under the elevated ambient pressure is investigated by a detailed numerical simulation using an E-L framework. Spray atomization is considered to have significant influences on the consequent phenomena such as combustion, thermoacoustic instability, emission formation as well as combustion noise, which have been proved in our previous works [1–4].

For spray atomization under the atmospheric ambient pressure, Wu et al. [5] derived an analytical solution of liquid jet trajectories and breakup points in subsonic crossflows, which is validated experimentally by Sallam et al. [6]. Also, Sallam et al. [6] illustrated a

detailed insight into atomization characteristics including breakup mode regimes, onset of the ligament and droplet formation, droplet velocities after breakup as well as liquid jet trajectories of round non-turbulent liquid jets in subsonic crossflows at normal temperature and ambient pressure. Spray atomization in crossflows is further investigated by experiments under various conditions [7–9]. However, only the liquid jet trajectory is precisely confirmed to be decided by the liquid-gas momentum flux ratio and aerodynamic Weber number, and the detailed primary breakup behaviors remain unclarified. In contrast to the experimental approaches, numerical simulations with high-fidelity are performed under different conditions [10–15], which are not only in good agreement with experimental studies, but also illustrated detailed mechanism of primary breakup behaviors within various liquid-gas density ratios as well as viscosity ratios.

However, Song et al. [16] pointed out those conclusions obtained from the low pressure conditions could not be applicative for the cases under the elevated ambient pressure conditions which are close to real engine conditions. Measurements are generally constrained to the laboratory conditions and have difficulties in providing the practical pressure condition of real aircraft engines. Still, many groups achieved to enlarge the ambient pressure to tens of atmospheric pressure [16–19]. An obvious difference in the conclusions is the liquid jet trajectory. Besides the liquid-gas momentum flux ratio and aerodynamic Weber number found in the normal ambient pressure and temperature, the liquid-gas viscosity ratio as well as density ratio are found becoming dominant in the liquid jet development.

Most recently, some new numerical methods are proposed to endure extremely large liquid-gas density ratio [20–22] and weakly compressibility of gas phase [23] such that the detailed mechanism of spray atomization under the elevated ambient pressure and temperature could be further clarified by numerical approaches in the future.

The purpose of this chapter is, therefore, to investigate the atomization-evaporation process of a liquid fuel jet in the vicinity of a fuel nozzle in several different steady crossflows under the elevated ambient pressure by a detailed numerical simulation using an E-L framework, in which the Eulerian framework is applied for both gas and liquid con-

tinuum fluid phases, and the Lagrangian framework is applied for the dispersed droplets generated by the atomization process. A CLSVOF method is utilized to capture the liquid-gas interface to obtain accurate surface tension with a CSF model. The evaporation of droplets is considered by a non-equilibrium Langmuir-Knudsen evaporation model [24–27].

2.2 Numerical simulation methods

2.2.1 Governing equations for Eulerian framework

Both liquid and gas phases are solved in the Eulerian framework and are treated as incompressible fluids. The governing equations used in the present calculation are the conservation equations of mass, momentum, energy, and mass fraction of chemical species applied to a detailed numerical simulation using in-house code, FK^3 [4, 28–30].

$$\rho \nabla \cdot \boldsymbol{u} = S_\rho, \tag{2.1}$$

$$\rho(\frac{\partial \boldsymbol{u}}{\partial t} + \boldsymbol{u} \cdot \nabla \boldsymbol{u}) = -\nabla P + \nabla \cdot \boldsymbol{\tau} + \boldsymbol{F}_\sigma + S_{\rho u}, \tag{2.2}$$

$$\rho[\frac{\partial h}{\partial t} + \nabla \cdot (\boldsymbol{u}h)] = \nabla \cdot (\frac{\lambda}{c_p} \nabla h) + S_{\rho h}, \tag{2.3}$$

$$\rho[\frac{\partial Y_k}{\partial t} + \nabla \cdot (\boldsymbol{u}Y_k)] = \nabla \cdot (D_k \nabla Y_k) + S_{\rho Y_k}. \tag{2.4}$$

Here, ρ is the density, $\boldsymbol{u}$ the velocity, P the pressure, μ the viscosity, $\boldsymbol{\tau}$ the viscous stress tensor, $\boldsymbol{F}_\sigma$ the source term of surface tension, h the enthalpy, λ and c_p are the thermal conductivity and specific heat capacity at constant pressure, respectively. Y_k and D_k are the mass fraction and mass diffusion coefficient of the chemical species k, respectively. Eqs. 2.1 and 2.2 are employed for both gas and liquid phases, while Eqs. 2.3 and 2.4 are only employed for the gas phase.

Density ρ and viscosity μ are calculated by the Heaviside function H_Γ, which is given

as follows.

$$\rho = \rho_l H_\Gamma(\varphi) + \rho_g[1 - H_\Gamma(\varphi)], \tag{2.5}$$

$$\mu = \mu_l H_\Gamma(\varphi) + \mu_g[1 - H_\Gamma(\varphi)], \tag{2.6}$$

$$H_\Gamma(\varphi) = \begin{cases} 0 & (\varphi < -\Gamma), \\ \frac{1}{2}[1 + \frac{\varphi}{\Gamma} + \frac{1}{\pi} sin(\frac{\pi\varphi}{\Gamma})] & (|\varphi| \leqslant \Gamma), \\ 1 & (\varphi > \Gamma). \end{cases} \tag{2.7}$$

Here, subscripts g and l are used to describe the gas phase and liquid phase, respectively. φ is the levelset function, which will be described later. The interface thickness in the present calculation is set to be 2Γ and $\Gamma = 1.5\Delta$. Δ is the mesh size.

S_ρ, $S_{\rho u}$, $S_{\rho h}$, and $S_{\rho Y_k}$ are the source terms of mass, momentum, energy, and chemical species, respectively, for the interaction effects between gas phase and fuel droplets by applying the particle-source-in-cell (PSI-Cell) method [31], and are calculated as follows.

$$S_\rho = -\frac{1}{\Delta V} \sum_N \frac{dm_d}{dt}, \tag{2.8}$$

$$S_{\rho u} = -\frac{1}{\Delta V} \sum_N \frac{dm_d \boldsymbol{u}_d}{dt}, \tag{2.9}$$

$$S_{\rho h} = -\frac{1}{\Delta V} \sum_N \frac{dm_d h_d}{dt}, \tag{2.10}$$

$$S_{\rho Y_k} = -\frac{1}{\Delta V} \sum_N \frac{dm_d}{dt} \quad \text{for} \quad Y_k = Y_F. \tag{2.11}$$

Here, ΔV is the volume of the unit grid, N is the number of droplets in the grid, and m_d, $\boldsymbol{u}_d$, and h_d are the mass, velocity, and enthalpy of the droplet, respectively.

2.2.2 Governing equations for Lagrangian framework

In this chapter, two sets of governing equations are applied for the cases whether the evaporation effect is considered for the Lagrangian droplets or not. First, the numerical simulations with different liquid jet inlet velocity profiles are validated by applying the Lagrangian framework without considering evaporation of droplets to decide the velocity

profile that should be applied for the further evaporation investigation. Secondary atomization and dense particulate effects of droplets in the atomization process are neglected because both the local aerodynamic Weber number and volumetric loading of droplets in crossflows are small. A non-equilibrium Langmuir-Knudsen evaporation model is used for capturing the evaporation process of the fuel droplets because the non-equilibrium effects are more important for droplets with diameter less than 50 µm [24, 25]. The verification and validation of the evaporation model in this chapter have already been investigated in our previous works [26, 27].

To track the profiles of droplets such as the position, velocity, temperature, and mass of each droplet, governing equations with a non-equilibrium Langmuir-Knudsen model for droplet evaporation are given as follows [24–27].

$$\frac{d\boldsymbol{x}_d}{dt} = \boldsymbol{u}_d, \tag{2.12}$$

$$\frac{d\boldsymbol{u}_d}{dt} = \frac{f_1}{\tau_d}(\boldsymbol{u} - \boldsymbol{u}_d), \tag{2.13}$$

$$\frac{dT_d}{dt} = \frac{Nu}{3Pr}\frac{c_p}{c_{p,d}}\frac{f_2}{\tau_d}(T - T_d) + \frac{1}{m_d}\frac{dm_d}{dt}\frac{L_V}{c_{p,d}}, \tag{2.14}$$

$$\frac{dm_d}{dt} = \dot{m}_d. \tag{2.15}$$

Here, $\boldsymbol{x}_d$, $\boldsymbol{u}_d$, T_d, and m_d are the position, velocity, temperature, and mass of the Lagrangian droplet, respectively. T is the gas temperature, $c_{p,d}$ the specific heat capacity of the droplet at constant pressure, L_V the latent heat of evaporation at T_d. f_1 and τ_d are the drag coefficient [32] and response time for the droplet, respectively, calculated as follows.

$$f_1 = \begin{cases} 1 & (Re_d \leqslant 1), \\ (1 + 0.15Re_d^{0.678}) & (Re_d > 1), \end{cases} \tag{2.16}$$

$$\tau_d = \frac{\rho_d d_d^2}{18\mu}. \tag{2.17}$$

Here, $Re_d = \rho_d u_d d_d/\mu$ is the Reynolds number of the droplet, d denotes the diameter, and the subscript d is used to describe the droplet.

Especially, Eqs. 2.12 and 2.13 are for the droplet with and without considering evaporation, whereas Eqs. 2.14 and 2.15 are only for the droplet with considering

evaporation. The Prandtl number (Pr) and Nusselt number (Nu) in Eq. 2.14 are given as follows.

$$Pr = \frac{\mu c_p}{\lambda}, \quad Nu = 2 + 0.552 Re_{sl}^{1/2} Pr^{1/3}. \tag{2.18}$$

Here, $Re_{sl} = \rho u_{sl} d_d / \mu$ is the Reynolds number calculated by the slip velocity $u_{sl} = |\boldsymbol{u} - \boldsymbol{u}_d|$. The correction coefficients of Stokes drag, f_1, and heat transfer, f_2, for the evaporation of the fuel droplet [33, 34] are evaluated as follows.

$$f_1 = \frac{1 + 0.0545 Re_{sl} + 0.1 Re_{sl}^{1/2}(1 - 0.03 Re_{sl})}{1 + b|Re_b|^c}, \quad f_2 = \frac{\beta}{e^\beta - 1}, \tag{2.19}$$

$$b = 0.06 + 0.077 \exp(-0.4 Re_{sl}), \quad c = 0.4 + 0.77 \exp(-0.04 Re_{sl}). \tag{2.20}$$

Here, $Re_b = \rho u_b d_d / \mu$ is the Reynolds number calculated by using the blowing velocity, $u_b = \dot{m}_d / (\pi d_d^2 \rho)$. β is the non-dimensional evaporation parameter given as

$$\beta = -\frac{3 Pr \tau_d}{2} \frac{\dot{m}_d}{m_d}. \tag{2.21}$$

The evaporation rate $\dot{m}_d$ could be calculated by the non-equilibrium Langmuir-Knudsen evaporation model which neglects the effect of temperature gradient inside the droplet.

$$\dot{m}_d = -\frac{m_d}{\tau_d} \frac{Sh}{3Sc} \ln(1 + B_M). \tag{2.22}$$

Here, Sc and Sh denote the Schmidt number and Sherwood number given as

$$Sc = \frac{\mu}{\rho D_k}, \quad Sh = 2 + 0.552 Re_{sl}^{1/2} Sc^{1/3}. \tag{2.23}$$

and B_M denotes the mass transfer number and is given as

$$B_M = \frac{Y_{F,s} - Y_F}{1 - Y_{F,s}}. \tag{2.24}$$

Here, Y_F is the mass fraction of fuel vapor, and $Y_{F,s}$ is the fuel vapor surface mass fraction given as follows.

$$Y_{F,s} = \frac{X_{F,s}}{X_{F,s} + (1 - X_{F,s})\overline{W}/W_F}, \tag{2.25}$$

$$X_{F,s} = \frac{P_{sat}}{P} - \frac{2 L_K}{d_d} \beta. \tag{2.26}$$

Here, $X_{F,s}$ is the mole fraction of fuel vapor at droplet surface for which the non-equilibrium effects are accounted for using the Langmuir-Knudsen evaporation law. P_{sat} the saturated vapor pressure, P the pressure of the carrier gas, $\overline{W}$ the averaged molecular weight of the carrier gas, W_F the molecular weight of the fuel vapor. L_K is the Knudsen layer thickness, given as

$$L_K = \frac{\mu(2\pi T_d R/W_F)^{1/2}}{ScP}. \tag{2.27}$$

Here, R is the universal gas constant, $R = 8.314\text{J}/(\text{mol}\cdot\text{K})$, and the saturated vapor pressure is given as

$$P_{sat} = P_{atm}\exp[\frac{L_V W_F}{R}(\frac{1}{T_B} - \frac{1}{T_d})]. \tag{2.28}$$

Here, P_{atm} is the atmospheric pressure, T_B is the fuel boiling temperature. L_V is assumed to be constant, and the gas is assumed to be ideal gas by using Clausius-Clapeyron equation. The latent heat of fuel, L_V, is estimated by using the Watson equation [35] given as

$$L_V = L_{V,T_{B,atm}}(\frac{T_c - T_d}{T_c - T_{B,atm}})^{0.38}. \tag{2.29}$$

Here, $L_{V,T_{B,atm}}$ is the latent heat at normal boiling temperature, T_c the critical temperature, and $T_{B,atm}$ the normal boiling point.

2.2.3 CLSVOF method

In this chapter, the liquid jet atomization process in crossflows is focused. Thus, the liquid-gas interface should be accurately captured to solve the source term of surface tension in Navier-Stokes equation. For the analysis of free surface flow, interface tracking and capturing methods are generally applied for simulation. Front tracking method is considered as an efficient method to track the interface for two-phase flows by reconstructing the marker function instead of advection, thus having much complexity [36]. Interface capturing methods such as VOF and levelset methods are always applied to deal with the violent interface deformation in the atomization process.

The present calculation aims to couple the levelset method with the VOF method to capture the liquid-gas interface. The method is so-called CLSVOF method, which is an Eulerian method. To grasp the extremely complex interface deformation in the crossflow atomization process, VOF method with good volume conservation for the calculation of the interface advection is thus applied. The WLIC scheme is implemented for the VOF reconstruction and the VOF value is saved at the cell center, such that it could be regarded as the cell-averaged value. Eq. 2.30 is used as the advection equation of the VOF function to calculate the advection for each step [37–39].

$$\frac{\partial \psi}{\partial t} + \nabla \cdot (\boldsymbol{u}\psi) - \psi \nabla \cdot \boldsymbol{u} = 0. \tag{2.30}$$

Here, ψ is the VOF function to represent the liquid volume fraction at the center of grid. Its value is taken from 0 to 1. $\psi = 0$ means that in the grid, only the gas phase exists, and $\psi = 1$ means that the grid is filled by the liquid phase. In the present calculation, $\psi = 0.5$ is considered to be the liquid-gas interface. Because of the inaccuracy of smoothly capturing the interface, the VOF function is coupled with the levelset function, which could define the distance to the interface [40, 41]. The levelset method has advantages for computing the interface curvature and normal vectors such that the surface tension could be precisely calculated.

The initial value of the levelset function is defined as

$$\varphi^n = (\psi^n - \psi_{\text{interface}}) \cdot \Gamma (\equiv \varphi_0^n). \tag{2.31}$$

Here, $\psi_{\text{interface}} = 0.5$ is considered to be the interface, and $\Gamma = 1.5\Delta$, Δ is the grid size, the superscript n means the time step. Since the levelset function is a distance function, it should hold the property of $|\nabla\varphi| = \text{const}$ in the whole domain. Then the levelset function is processed to satisfy the condition called reinitialization given as follows.

$$\frac{\partial \varphi^n}{\partial \tau} + S(\varphi_0^n) \frac{\nabla \varphi_0^n}{|\nabla \varphi^n|} \cdot \nabla \varphi^n = S(\varphi_0^n), \tag{2.32}$$

$$\varphi_0^n = \varphi^n|_{\tau=0}, \tag{2.33}$$

$$S(\varphi_0^n) = \frac{\varphi_0^n}{\sqrt{(\varphi_0^n)^2 + \Gamma^2}}. \tag{2.34}$$

Here, τ is the artificial time step. Note that the subscript 0 indicates the first step of the iteration of the reinitialization [40, 41]. After the reinitialization process, the source term of surface tension could be calculated by the CSF model [39, 42] given as follows.

$$\boldsymbol{F}_\sigma = \sigma\kappa\boldsymbol{n}_\varphi\delta_\Gamma(\varphi), \tag{2.35}$$

$$\delta_\Gamma(\varphi) = \begin{cases} 0 & (|\varphi| \geqslant \Gamma), \\ \frac{1}{2\Gamma}[1 + cos(\frac{\pi\varphi}{\Gamma})][1 + \frac{\varphi}{\Gamma} + \frac{1}{\pi}sin(\frac{\pi\varphi}{\Gamma})] & (|\varphi| < \Gamma), \end{cases} \tag{2.36}$$

$$\boldsymbol{n}_\varphi = \frac{\nabla\varphi}{|\nabla\varphi|}, \tag{2.37}$$

$$\kappa = \frac{1}{|\nabla\varphi|}(\frac{\nabla\varphi}{|\nabla\varphi|} \cdot \nabla|\nabla\varphi| - \nabla \cdot \nabla\varphi). \tag{2.38}$$

Here, σ is the surface tension, κ the local curvature of the interface, $\boldsymbol{n}_\varphi$ the local normal vector of the interface. Both $\boldsymbol{n}_\varphi$ and κ are calculated by the levelset function φ. Even though CSF model applied in the CLSVOF method may lead to the spurious currents [43], this issue is ignored due to the low liquid-gas density ratio because of the elevated pressure. For the present calculation, surface tension is only considered at the liquid-gas interface where a smoothed Delta function δ_Γ is used, which modified the standard CSF model to improve the stability [39].

2.2.4 Eulerian-Lagrangian coupling

The Eulerian method, that is the CLSVOF method, could hardly capture the behavior of very small droplets unless the equivalent mesh size is applied in the computation. Thus, an extremely high computational cost is required to perform the atomization process with high fidelity. The Lagrangian method is considered an effective way to reduce the computational cost by dealing with the dispersed droplets using the Lagrangian method and tracking them in the Lagrangian framework as state in Section 2.2.2.

2.2.4.1 Eulerian-Lagrangian tagging method

The Eulerian droplet is required to be transformed into a Lagrangian droplet once the droplet is generated and disperses away from the liquid jet. Therefore, an Eulerian-

Lagrangian tagging (referred to as E-L tagging, hereafter) method is employed to detect the Eulerian droplet and transform it into Lagrangian droplet for each step. To simply explain the E-L tagging method employed in the present study, 2-dimensional schematics are given as shown in Fig. 2.1. First, a threshold for the tagging method should be artificially given, with which the cells satisfying the judgement would be tagged and then become one part of a transformed Lagrangian droplet. In the present study, the volume fraction of liquid phase ψ, is used for the tagging method, and hence the threshold for ψ is set as ψ_{cri}.

For a cell satisfying $\psi > \psi_{cri}$, it would be tagged by a red marker as shown in Fig. 2.1(a). The surrounding cells are then checked and also the cells satisfying $\psi > \psi_{cri}$ are tagged by blue markers, which represent the edge of the tagged droplet as shown in Fig. 2.1(b). Later on, the cells neighboring the edge of the tagged droplet are checked and tagged by blue markers to represent the new edge of the tagged droplet, and the original blue markers are switched to red markers to represent the inside of the tagged droplet as shown in Fig. 2.1(c). By looping the steps from (b) to (c), a droplet would be filled by red markers and no further neighboring cells could be tagged by blue markers, then all markers are switched to red markers as shown in Fig. 2.1(d), which would later be tagged by a specific marker such as 1 shown in Fig. 2.1(e). By employing the steps from (a) to (d), all the dispersed Eulerian components would be tagged by the specific markers such as 1, 2, and 3, as shown in Fig. 2.1(e). Then the details of each tagged Eulerian component would be further checked. For example, for 3 in Fig. 2.1(e), some cells in it are neighboring the wall boundary such that the detailed information could not be further checked, which makes 3 unable to be recognized as a Lagrangian droplet as shown in Fig. 2.1(f). Some more complex situations are provided in Fig. 2.1(g), for example, how to deal with the cells marked by the question marks since they should belong to two individual droplets, or how to deal with the dispersed component with extremely slim structure marked by the red rectangle. Therefore, for more interests of this tagging method, please refer to the work of Herrmann [44] and Zuzio et al. [45].

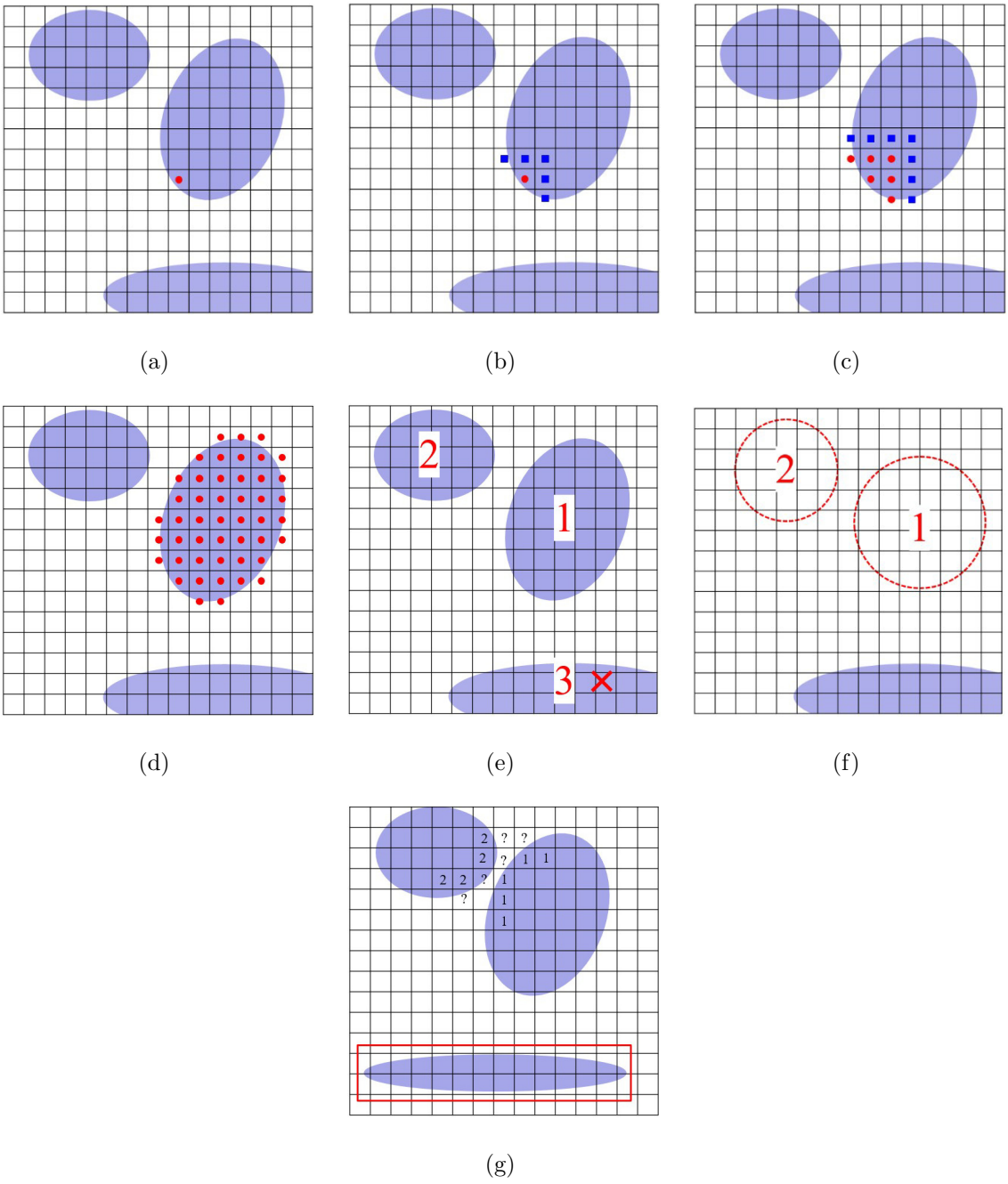

Figure 2.1: Algorithm of E-L tagging method.

In this chapter, the threshold of the detected VOF value ψ_{cri} is set to be 0.01, that is, once the volume fraction of the liquid phase in the grid cell is larger than 0.01, it would be tagged and become one part of a droplet. The validation of the E-L tagging

method is provided in Appendix A.

2.2.4.2 Transformation to Lagrangian droplets

The profiles of tagged Eulerian droplets such as position, velocity, temperature, and mass need to be accurately transformed into Lagrangian droplets within the E-L tagging method. The volume and center of gravity of each tagged Eulerian droplet are calculated by the VOF values and the following equations.

$$V_d = \Delta V \sum_{ii} \psi_{ii}, \tag{2.39}$$

$$\boldsymbol{x}_d = \Delta V \frac{1}{V_d} \sum_{ii} x_{ii} \psi_{ii}. \tag{2.40}$$

Here, ii is the number of the grids in the droplet. For the transformed Lagrangian droplet, the velocity is given at the gravity center and value is obtained by averaging the Eulerian velocity [45]. The temperature is given by using the liquid phase temperature and the mass is calculated by the volume without considering the density change of the liquid fuel.

Based on the calculated droplet volume V_d, the transformed Lagrangian droplets need to satisfy the following equation.

$$V_d \leqslant \frac{4}{3}\pi r_{\text{trans}}^2, \tag{2.41}$$

Here, r_{trans} is the maximum radius of the Lagrangian droplets, and $r_{\text{trans}} = 10$ µm because the CSF model employed in the CLSVOF method could hardly calculate the droplets precisely within a diameter smaller than 3 grids. The surface tension is calculated by the local normal vector and local curvature with a Delta function at the liquid-gas interface, both of which are calculated by the local levelset value as suggested by Eqs. 2.35-2.38. However, the thickness of liquid-gas interface is artificially set to be 3 grids for the level function as suggested by Eq. 2.30 and thus make it difficult to calculate the density and viscosity as suggested by Eqs. 2.5-2.7. Therefore, the accuracy for the droplet calculation is limited to 3 grids.

In addition, to avoid incorrectly transforming the elongated Eulerian phase such as ligaments to Lagrangian droplets, the droplet sphericity is set as a criterion, defined as $\alpha = r_{max}/\max[\Delta x, r_{eff}]$. Here, r_{max} is the maximum distance to the center of mass for the liquid structure and r_{eff} is the effective radius corresponding to the volume of the liquid phase. The transformation could only occur when $\alpha \leqslant \alpha_{cri}$, where α_{cri} is set as 2 [46]. If the droplet is small enough, the further breakup could not occur due to the higher surface tension compared to the aerodynamic force.

2.2.4.3 Droplet collision on the liquid-gas interface

To capture the accurate atomization behavior properly, the collision between Lagrangian droplets and the liquid-gas interface is considered. The schematic for the collision process is shown in Fig. 2.2 with the following equations [45].

$$\boldsymbol{u}_d \cdot \nabla\varphi > 0, \tag{2.42}$$

$$|\varphi_d| < \frac{d_d}{2}. \tag{2.43}$$

Here, $\boldsymbol{u}_d$ is the velocity of the Lagrangian droplet, φ_d the levelset value at the droplet center of gravity $\boldsymbol{x}_d$ interpolated by φ. Since the levelset value of the interface is set as 0, the droplet collision occurs if the distance of droplet center to the interface is less than the radius of the droplet, with the velocity direction to the interface. While the droplet is re-impacting on the interface, the VOF value will be re-built based on the center of gravity to conserve the mass and momentum, which is determined by the droplet size. Two kinds of droplets with diameter larger and smaller than mesh size are reconstructed respectively, which could be found in Zuzio's work [45].

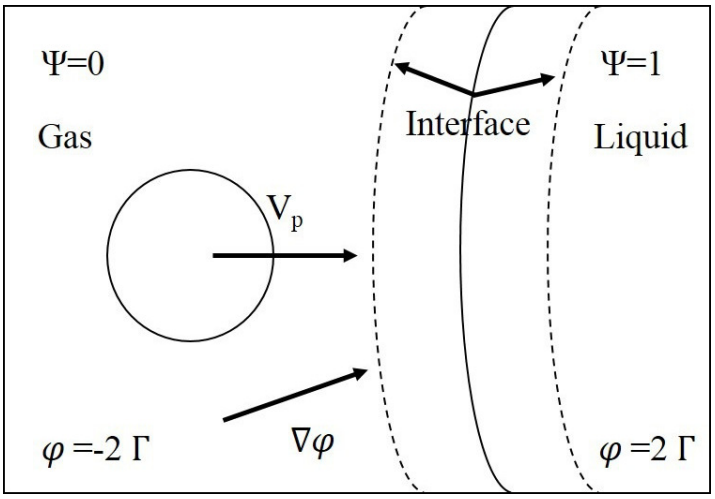

(a)

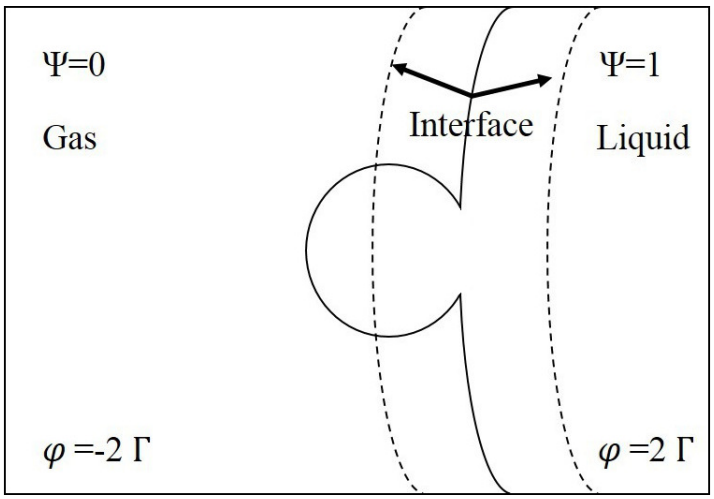

(b)

Figure 2.2: Schematics of collision between Eulerian liquid-gas interface and a Lagrangian droplet: (a) before collision, (b) after collision. Solid line indicates liquid-gas interface of $\varphi = 0$, and dashed line indicates maximum and minimum iso-values of levelset function.

2.3 Computational setup

2.3.1 Primary breakup mode in crossflow atomization

The primary breakup is the process in which the injected liquid jet is pushed by the perpendicular gaseous flow and finally deforms into droplets. The generated droplets often again collapse into smaller droplets by the aerodynamic force which is called secondary breakup. Then, the generated droplets evaporate and become fuel vapor for the final chemical reaction as shown in Fig. 2.3.

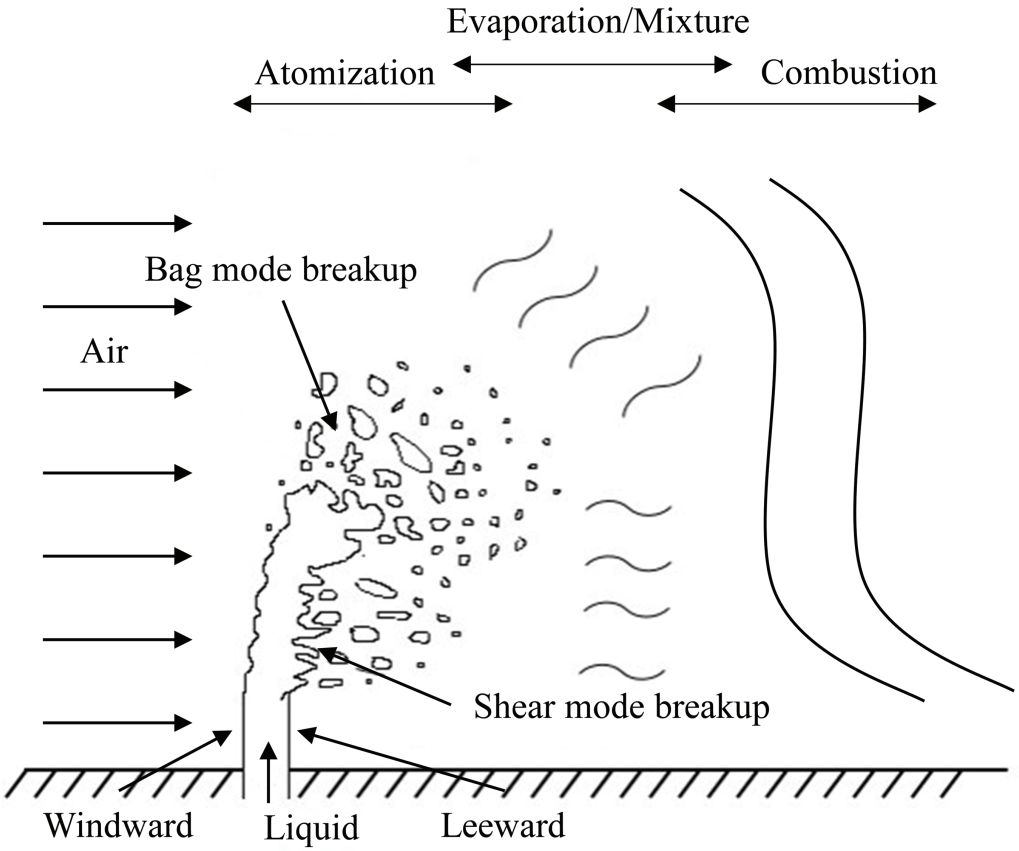

Figure 2.3: Schematic of spray combustion in a crossflow.

Generally, the primary breakup process in crossflow is thought to be of two different types, namely bag breakup and shear breakup. The bag breakup is the atomization behavior when the liquid jet collapses into relatively large droplets at the jet tip part

because of the enhanced surface waves generated on the windward. The waves are transported to the liquid jet tip with enhanced wavelength and then pitch-off to produce bag-like blobs, finally generate many smaller droplets. On the other hand, the shear breakup results from the shear force around the liquid jet, where many liquid threads are formed and droplets are generated at the end of threads. Wu et al. [5] and Sallam et al. [6] have stated that such primary breakup behavior is characterized by the aerodynamic Weber number, We, and the liquid Ohnesorge number, Oh, defined as follows.

$$We = \frac{\rho_g u_g^2 D_{inj}}{\sigma}, \tag{2.44}$$

$$Oh = \frac{\mu_l}{\sqrt{\rho_l D_{inj} \sigma}}. \tag{2.45}$$

When the liquid Ohnesorge number is small ($Oh < 0.3$), i.e., the liquid viscosity effect is negligibly small compared to the surface tension effect, the primary breakup behavior is only dominated by the aerodynamic Weber number and thus divided into four different mode regimes, namely, column mode regime ($We < 4$), bag mode regime ($4 \leqslant We < 30$), multimode regime ($30 \leqslant We < 110$), and shear mode regime ($We > 110$), respectively [6]. For the column mode regime, the deformation and breakup of the liquid jet are caused only by the reduced gas pressure alongside the liquid jet while air flow passes it. On the other hand, the bag and shear breakups are dominant for the bag and shear mode regimes, respectively, and both breakups coexist for the multimode regime. In this chapter, the atomization-evaporation process is investigated under different aerodynamic Weber number conditions for different primary breakup mode regimes.

2.3.2 Computational domains and conditions

As mentioned in Section 2.2.2, a cold state simulation is firstly performed to select a better liquid jet inlet velocity profile without considering the evaporation of droplets. A hot state simulation is then conducted by employing a non-equilibrium Langmuir-Knudsen evaporation model to investigate the atomization-evaporation process in crossflows with the better liquid jet inlet velocity profile. The performed cases are listed in Table 2.1 and Fig. 2.4 shows three computational domains set for these computations, consider-

ing the liquid jet height, computational cost, as well as accuracy. The comparison of the cases 1 and 2 is conducted to verify the effects of liquid jet inlet velocity profile on the liquid jet trajectory and atomization behavior, since some researchers have reported that the liquid jet trajectory is greatly influenced by the liquid jet velocity profile in the fuel nozzle [10–12, 47]. The comparison of the cases 3-5 is done to discuss the atomization-evaporation process.

Table 2.1: Computational cases performed for crossflow atomization.

Case	We	Domain	Purpose
1. Uniform velocity	70.7	a	Figure out a better liquid jet inlet velocity profile
2. Parabolic velocity	70.7	a	
3. Bag mode regime	10.0	b	Simulate the atomization-evaporation process
4. Multimode regime	46.0	c	
5. Shear mode regime	200.0	c	

All three computational domains are set to be an open space within a boundary at the bottom, where the fuel nozzle with a diameter of 0.1 mm is mounted. The boundary wall with a height of 0.15 mm is established for the liquid jet velocity development in the nozzle. The simulations are performed on the uniform staggered Cartesian grid with a uniform mesh size of $\Delta x = \Delta y = \Delta z = 5$ µm.

To investigate the influence of different liquid jet inlet velocity distributions, two different flow types, uniform and parabolic, as shown in Fig. 2.5, are set to be at the same average velocity, 12.4 m/s, and liquid Reynolds number, 366, which denotes laminar flows. The velocity profiles for cases 1 and 2 are given as follows.

$$u_{l,inj} = 12.4, \tag{2.46}$$

$$u_{l,inj} = 2 \times 12.4 \times (1 - \frac{r^2}{(D_{inj}/2)^2}). \tag{2.47}$$

For cases 1 and 2, the computational domain consists of $200 \times 200 \times 120$ grid points (a total of 4.8 million grid points) in the x, y, and z directions. Thus, the physical size

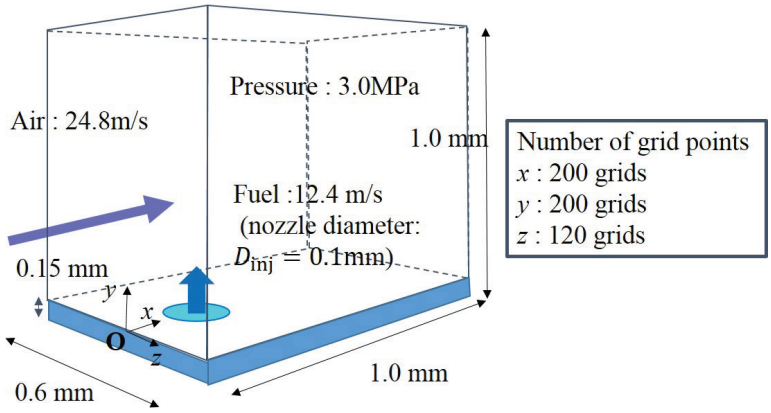

(a)

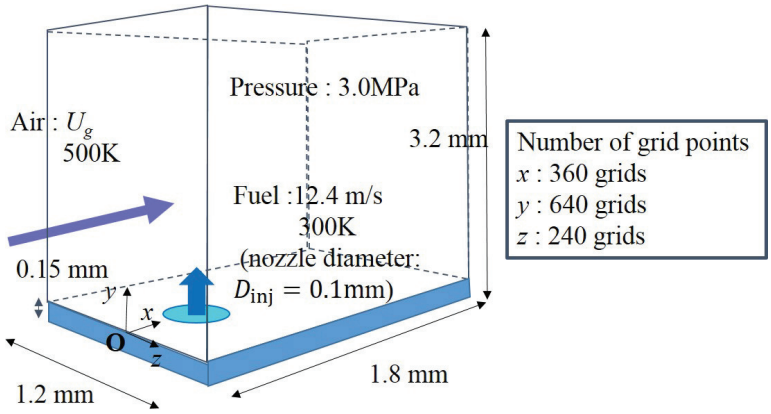

(b)

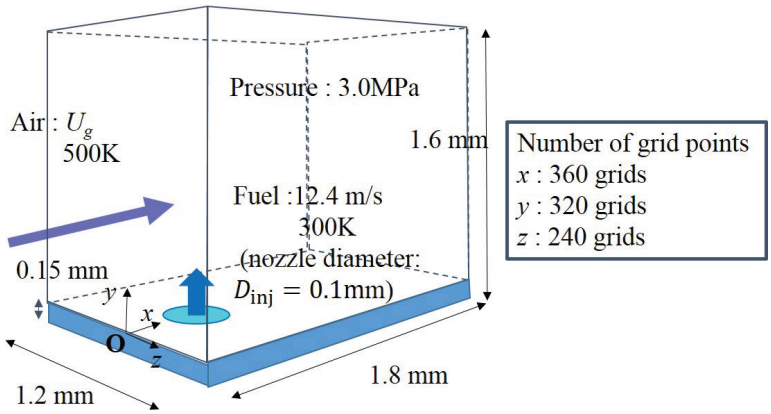

(c)

Figure 2.4: Schematics of computational domains and conditions: (a) non-evaporation computational domain for cases 1 and 2, (b) evaporation computational domain for case 3, (c) evaporation computational domain for cases 4 and 5.

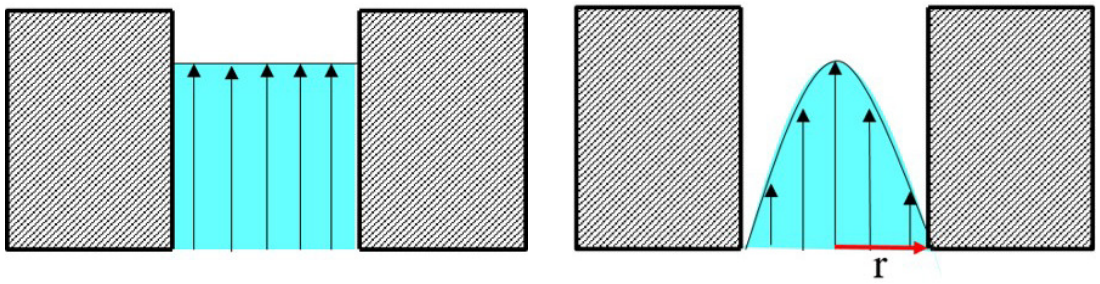

(a) (b)

Figure 2.5: Liquid jet inlet velocity distributions for case 1: (a) uniform distribution, and for case 2: (b) parabolic distribution.

of the computational domain is $10D_{inj} \times 10D_{inj} \times 6D_{inj}$ (1.0 mm × 1.0 mm × 0.6 mm), which is a small length scale where the effect of gravity is thought to be neglected.

To investigate the atomization-evaporation process in different primary breakup mode regimes, crossflow velocity with high temperature, 500 K, and parabolic liquid jet inlet velocity profile is adjusted and the aerodynamic Weber number is varied as 10, 46, and 200 (cases 3, 4, and 5), respectively, which are classified into the bag mode regime, multimode regime, and shear mode regime, respectively [6]. The computational domains for the atomization-evaporation simulation are also extended due to the elevated temperature as shown in Figs. 2.4(b) and 2.4(c) consisting of $360 \times 640 \times 240$ grid points (a total of 55.3 million grid points) for case 3 and $360 \times 320 \times 240$ grid points (a total of 27.6 million grid points) for cases 4 and 5 in the x, y, and z directions. The computational domains are $18D_{inj} \times 32D_{inj} \times 12D_{inj}$ (1.8 mm × 3.2 mm × 1.2 mm) and $18D_{inj} \times 16D_{inj} \times 12D_{inj}$ (1.8 mm × 1.6 mm × 1.2 mm) where the effect of gravity could also be neglected. The length in the y direction for case 3 is two times of the other two cases because the lower crossflow velocity of case 3 could lead the liquid jet to reach a higher height than the others. Overall, the scale in x direction is decided by the breakup behavior, the scale in y direction is decided by the predicted penetration, and the scale in z direction is decided by the bifurcation jets which will be explained later. Furthermore, the liquid jet with cold temperature, 300 K, is injected from the bottom boundary. The boundary conditions are set as non-slip for the bottom wall, slip for the

spanwise direction and free for the other directions. The mirror reflection model is used for the Lagrangian droplet wall collision.

Tables 2.2 and 2.3 are the detailed computational conditions and physical properties of liquid fuel and gas for cases 1-2 and cases 3-5, respectively. The gas phase density in Table 2.3 is calculated by the state equation of ideal gas for each step considering the local temperature change due to the evaporation effect. M is the momentum flux ratio of liquid to gas given as

$$M = \frac{\rho_l u_l^2}{\rho_g u_g^2}. \tag{2.48}$$

The estimate of the Hinze scales, η_H, given by $\eta_H = \sigma/(\rho_g U_g^2)$, are estimated to be 10 µm, 2.35 µm, and 0.51 µm for the bag mode regime, multimode regime, and shear mode regime, respectively. The Kolmogorov scales, η_K, calculated by $\eta_K = (\nu^3/\epsilon)^{1/4}$, where ϵ denotes the average rate of dissipation of turbulent kinetic energy per unit mass, are estimated to be 0.96 µm, 1.37 µm, and 3.62 µm for the bag mode regime, multimode regime, and shear mode regime, respectively. Compared to the mesh resolutions of Li et al. [48] and Prakash et al. [47], which are $130\eta_H$ and $23\eta_H$, respectively, and considering the employed uniform meth size $\Delta x = 5$ µm, which are 0.5-9.8 η_H and 1.3-5.2 η_K, respectively, the simulations are good enough to capture the liquid jet breakup behaviors. In Appendix A, the comparison of liquid jet trajectory for different mesh resolutions is presented where the results again demonstrate the adequate of present mesh to resolve the liquid jet penetration as well as breakup behaviors.

The computational cost of each case performed at the K-Computer (Fujitsu SPARC64TM VIIIfx processor, 300 cores) is 184k hours (real time 80 h) for case 3 and 92k hours (real time 80 h) for each case of 4 and 5.

Table 2.2: Parameters of detailed numerical simulation for effect of different liquid jet inlet velocity distributions.

Physical properties	
Liquid fuel	Kerosene
Crossflow gas	Air
Liquid nozzle diameter, D_{inj} (mm)	0.1
Liquid jet velocity, u_l (m/s)	12.4
Liquid jet viscosity, μ_l (Pa·s)	2.87×10^{-3}
Liquid jet density, ρ_l (kg/m^3)	848
Liquid jet temperature, T_l (K)	300
Crossflow velocity, u_g (m/s)	24.8
Crossflow viscosity, μ_g (Pa·s)	1.97×10^{-5}
Crossflow density, ρ_g (kg/m^3)	34.5
Crossflow temperature, T_g (K)	300
Liquid-gas surface tension, σ (N/m)	0.03
Ambient pressure, P (MPa)	3.0
Aerodynamic Weber number, We (-)	70.8
Jet Ohnesorge number, Oh (-)	0.06
Liquid-gas momentum flux ratio, M (-)	6.14

Table 2.3: Parameters of detailed numerical simulation for atomization-evaporation process.

Physical properties	
Liquid fuel	Kerosene
Crossflow gas	Air
Liquid nozzle diameter, D_{inj} (mm)	0.1
Liquid jet velocity, u_l (m/s)	12.4
Liquid jet viscosity, μ_l (Pa·s)	2.87×10^{-3}
Liquid jet density, ρ_l (kg/m^3)	848
Liquid jet temperature, T_l (K)	300
Crossflow velocity, u_g (m/s)	12.0 ,24.8, 53.7
Crossflow viscosity, μ_g (Pa·s)	2.72×10^{-5}
Crossflow temperature, T_g (K)	500
Liquid-gas surface tension, σ (N/m)	0.03
Ambient pressure, P (MPa)	3.0
Aerodynamic Weber number, We (-)	10, 46, 200
Jet Ohnesorge number, Oh (-)	0.06
Liquid-gas momentum flux ratio, M (-)	43, 10, 2.2

2.4 Results and discussion

2.4.1 Effects of liquid jet inlet velocity distributions on liquid jet penetration

Fig. 2.6 shows the comparison of the front view of instantaneous iso-surface of levelset function of $\varphi = 0$, which is regarded as the liquid-gas interface, between cases 1 and 2 with the uniform and parabolic distribution velocities, respectively (see also Fig. 2.5). For both cases, the bag breakup indicated by blue circles and shear breakup indicated by red circles are observed, which suggests that the primary breakup in this condition proceeds under the multimode regime. It is also evident that the liquid jet inlet velocity profile in the nozzle strongly affects the liquid jet behavior, and the penetration of case 2 is larger and then the inclination is weaker than those of case 1. The reason why the penetration of case 2 is larger than that of case 1 is considered to be due to the fact that the central velocity of the liquid jet, in other words, the local liquid-gas momentum flux ratio in the central region for case 2, is much larger than that for case 1 due to the presence of velocity profile.

Fig. 2.7 also shows the comparison of the time-averaged liquid jet trajectories on the central $x-y$ plane ($z = 0$ mm) with the jet trajectories calculated by using two existing prediction formulas developed by Wu et al. [5] and Song et al. [16]. Here, Wu et al. [5] derived an analytical solution of jet trajectory at the room temperature and atmospheric pressure given as

$$y' = 1.37\sqrt{MD_{inj}x'}. \tag{2.49}$$

and this correlation was experimentally verified by Sallam et al. [6]. On the other hand, Song et al. [16] provided an empirical correlation at elevated pressure up to 10 bar, which is still low compared to the present study. However, Song's later experiment works from the view point of combustion instability fit our interests of combining combustion with atomization, hence his work is considered meaningful for the present study.

$$\frac{y'}{D_{inj}} = 1.163(\frac{x'}{D_{inj}})^{0.463} M^{0.557} We^{0.111} (\frac{\rho_l}{\rho_g})^{-0.052} (\frac{\mu_l}{\mu_g})^{-0.086}. \tag{2.50}$$

It is observed that the jet trajectory of case 2 is in better agreement with two predictions using Eqs. 2.49 and 2.50, than that of case 1, which supports the importance of the reproduction of velocity distribution in the nozzle. Therefore, the parabolic velocity distribution in the nozzle is take into account for all the cases discussed later, i.e., cases 3-5.

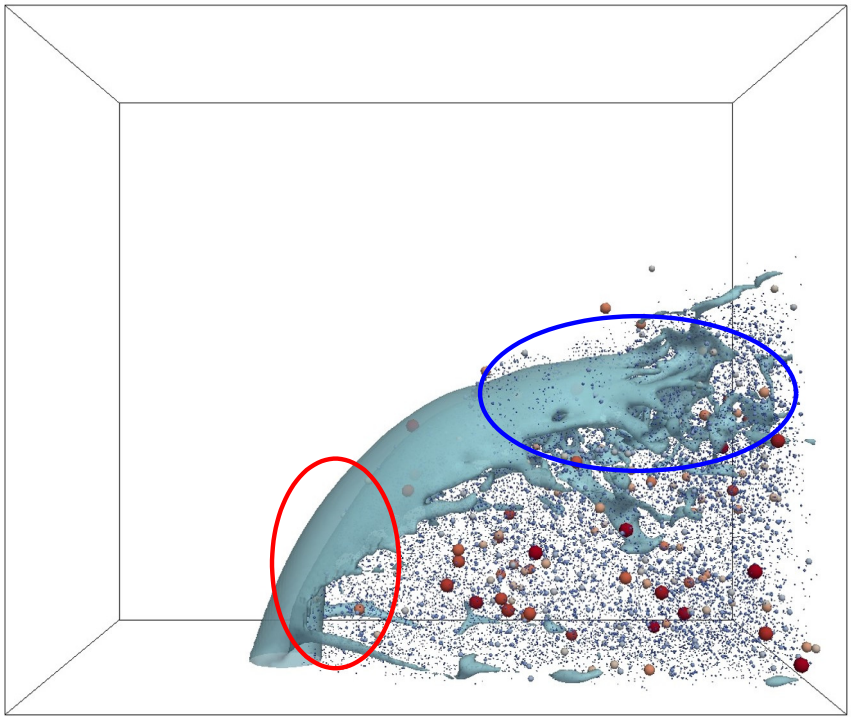

(a)

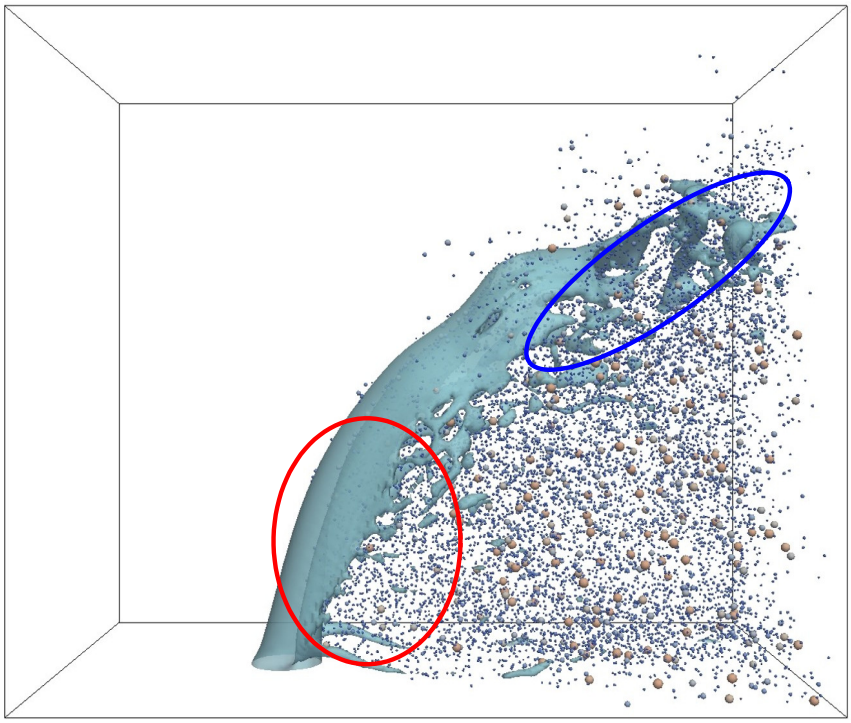

(b)

Figure 2.6: Front view snapshots of instantaneous iso-surface of levelset function of $\varphi = 0$: (a) case 1, (b) case 2.

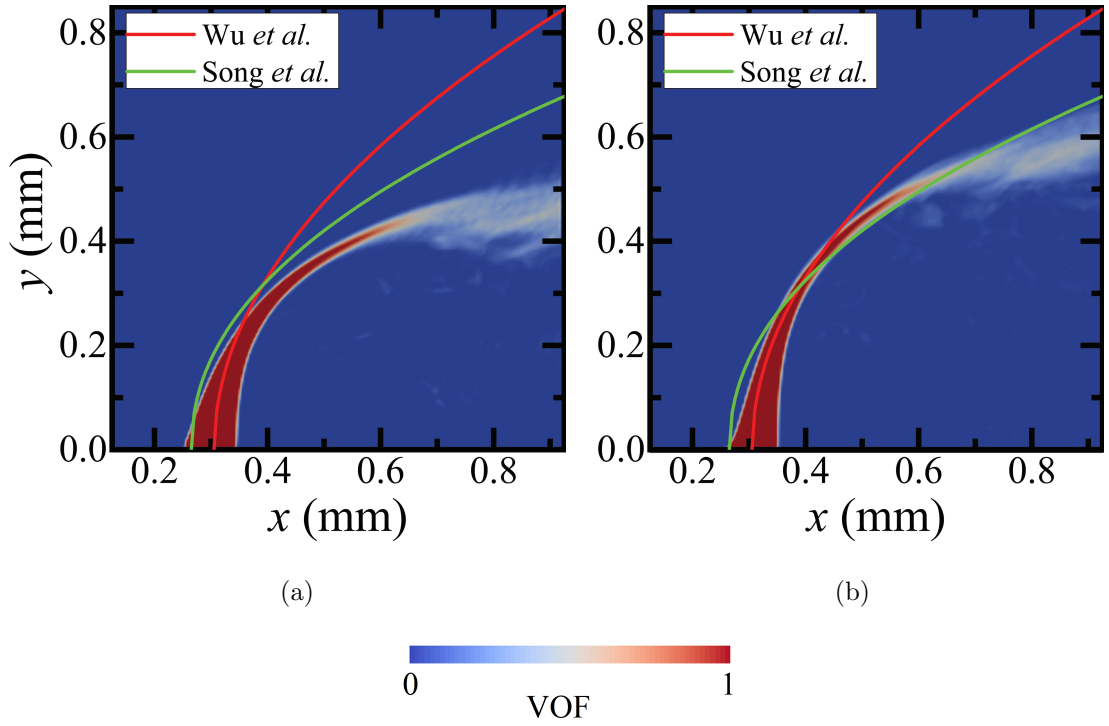

Figure 2.7: Time-averaged liquid jet trajectories on the central $x-y$ plane ($z = 0$ mm): (a) case 1, (b) case 2.

2.4.2 Atomization behavior

Figs. 2.8 - 2.10 show the comparisons of the front, side, and top views of instantaneous iso-surface of levelset function of $\varphi = 0$, respectively, which is regarded as the liquid-gas interface, among cases 3-5 with different aerodynamic Weber numbers. It is found that the atomization behavior tends to change depending on the aerodynamic Weber number. As the aerodynamic Weber number increases, the inclination of the liquid jet becomes evident due to the decreasing liquid-gas momentum flux ratio, M, and the dominant breakup feature shifts from the bag breakup, generating relatively large droplets around the liquid jet tip, to the shear breakup, generating many small droplets around the liquid jet surface with threads, from which it can be said that cases 3-5 are classified into the

bag mode regime, multimode regime, and shear mode regime, respectively. However, for the bag mode regime of case 3, it is observed that there appear two big threads, i.e., bifurcations, from the liquid jet surface, as indicated by red circles, and relatively large droplets are generated from them. This distinct phenomenon, as a result of the Rayleigh-Talor instability formed on the windward surface of the column, has also been reported by Sedarsky et al. [49]. However, they could not clarify the generation mechanism, but suggested that it is caused by the vorticities behind the liquid jet and not associated with the shear breakup. This will be discussed in more detail in the next section.

Fig. 2.11 shows the comparison of the time-averaged liquid jet trajectories on the central $x - y$ plane ($z = 0$ mm) with the jet trajectories calculated by the analytical solution of Eq. 2.49 and the empirical correlation of Eq. 2.50. The liquid jet trajectories are found to agree with those predicted by Eqs. 2.49 and 2.50. Based on these results, it can be said that the present simulation reproduces the atomization behavior with appropriate accuracy.

Fig. 2.12 shows the comparison of the time-averaged probability density function (PDF) of droplet size in the downstream region of 1.5 mm $\leqslant x \leqslant$ 1.8mm among cases 3-5. It is found that the smaller the droplet size is, the larger the PDF is for the all three cases, and that the trend becomes evident as the aerodynamic Weber number increases. As a result, the Sauter mean diameter (SMD) decreases with increasing the aerodynamic Weber number. This is due to the fact that the number of the small droplets generated from the threads on the liquid jet, that is the shear breakup, increases with increasing the aerodynamic Weber number. However, the difference in the SMD between the bag mode regime of case 3 and shear mode regime of case 5 is small (less than 10%), though the behaviors are quite different from each other (see Figs. 2.8 - 2.10). As the Weber number increased, more dispersed Eulerian phase without enough sphericity such as threads are generated. Therefore, much more smaller Eulerian phase would be easily torn apart and transformed into smaller Lagrangian droplets, thus, increasing the ratio of smaller droplets which would not decrease the counted SMD obviously because it is mainly determined by the larger droplets generated by the bag breakup.

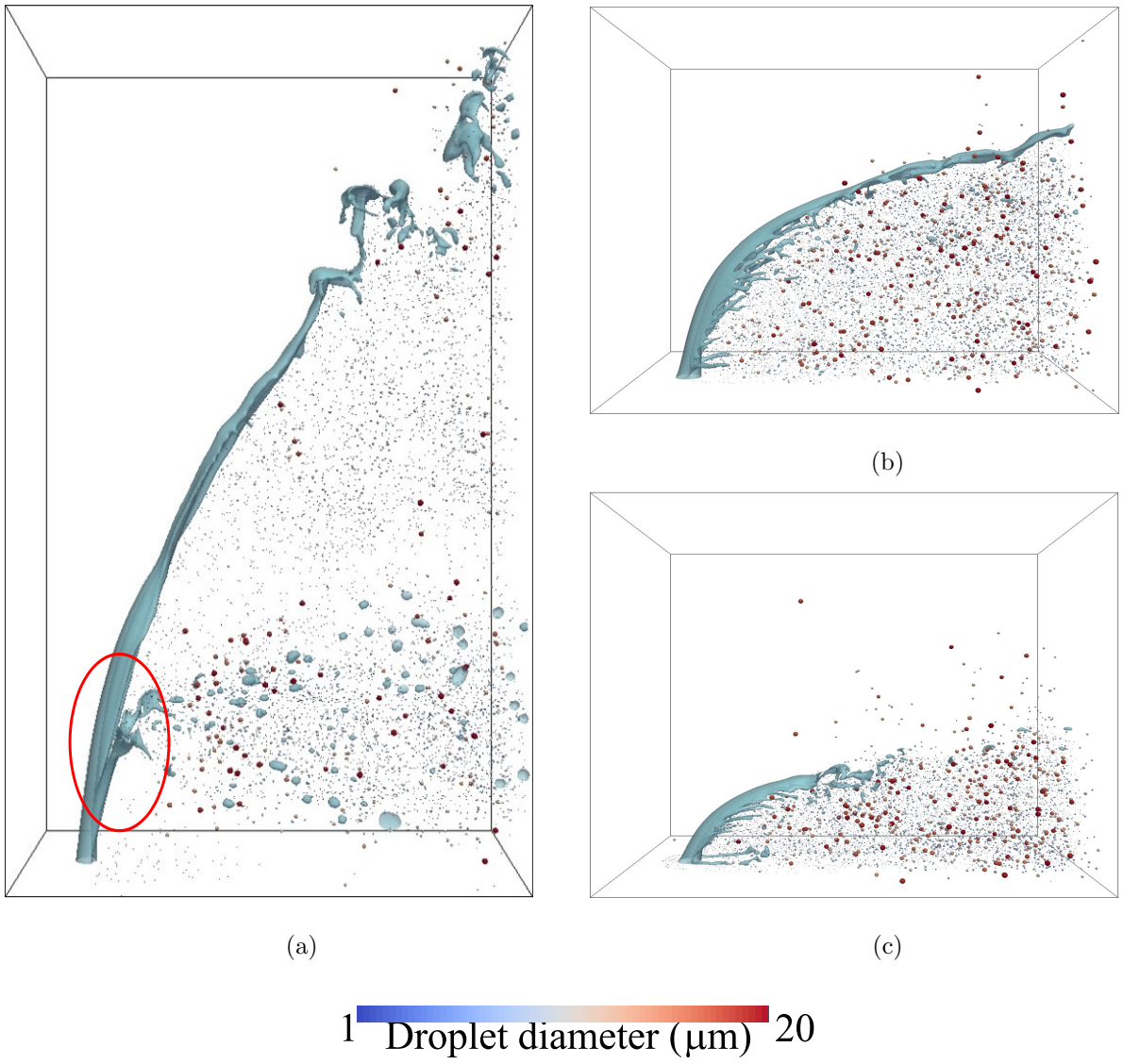

Figure 2.8: Front view snapshots of instantaneous iso-surface of levelset function of $\varphi = 0$: (a) case 3, (b) case 4, (c) case 5. Particle color indicates droplet diameter.

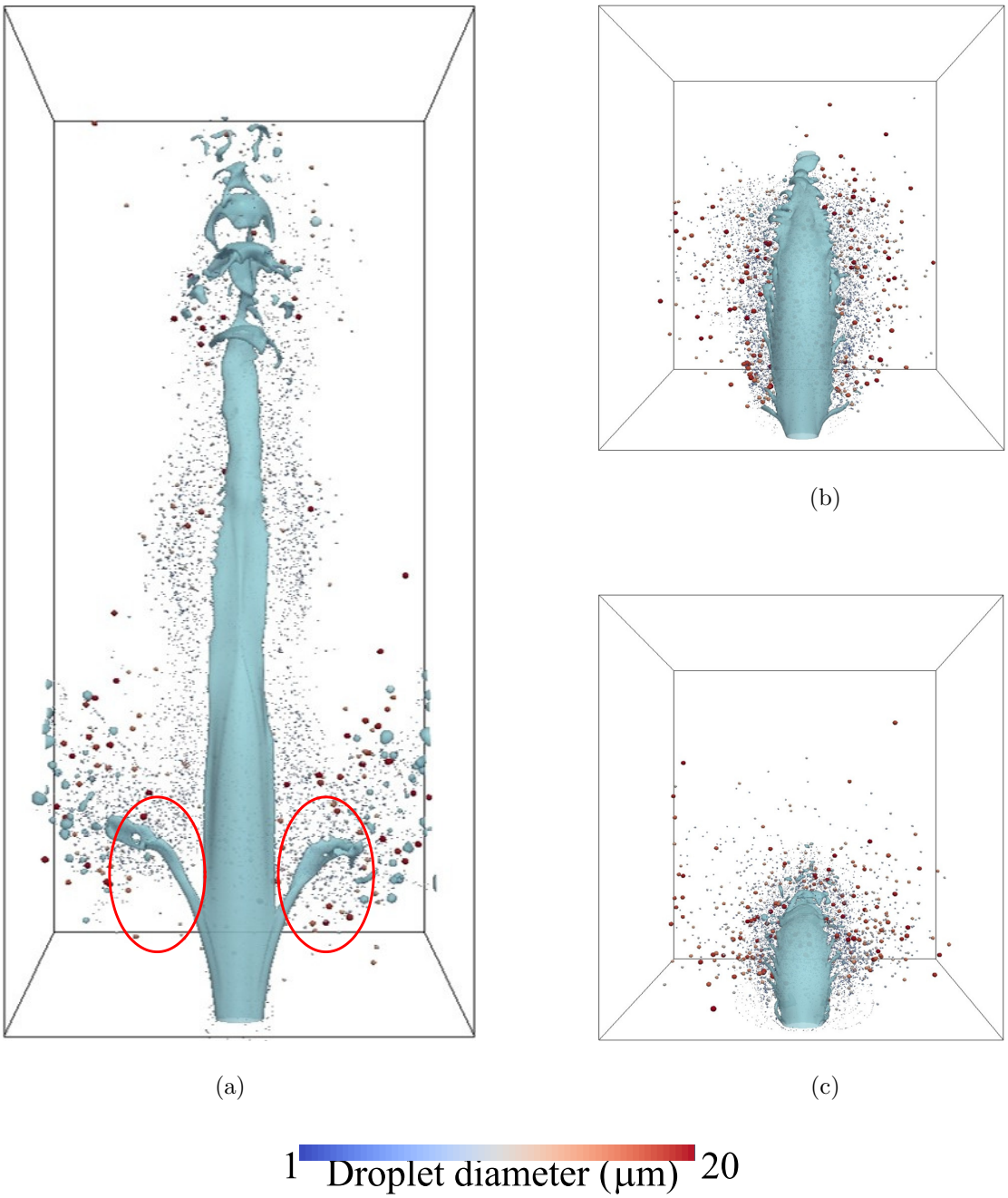

Figure 2.9: Side view snapshots of instantaneous iso-surface of levelset function of $\varphi = 0$: (a) case 3, (b) case 4, (c) case 5. Particle color indicates droplet diameter.

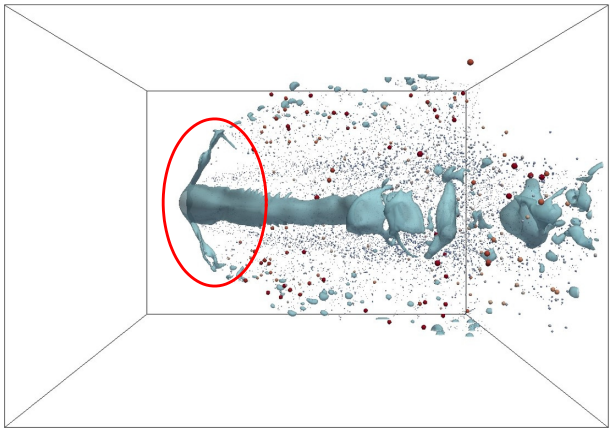

(a)

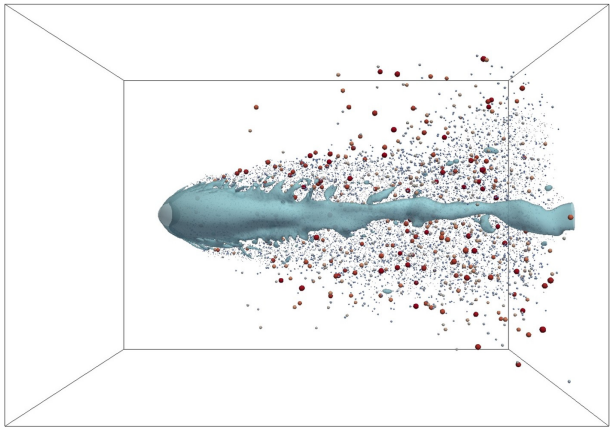

(b)

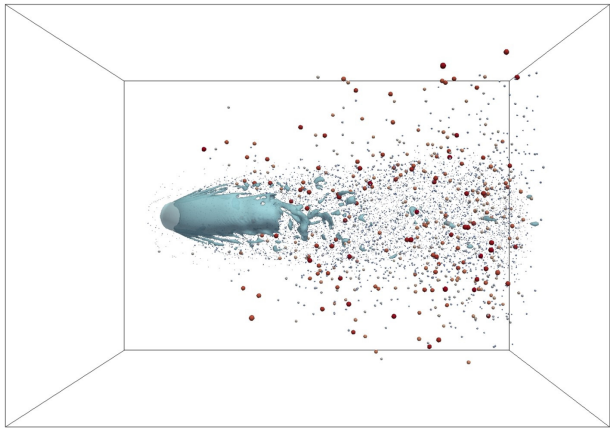

(c)

Figure 2.10: Top view snapshots of instantaneous iso-surface of levelset function of $\varphi = 0$: (a) case 3, (b) case 4, (c) case 5. Particle color indicates droplet diameter.

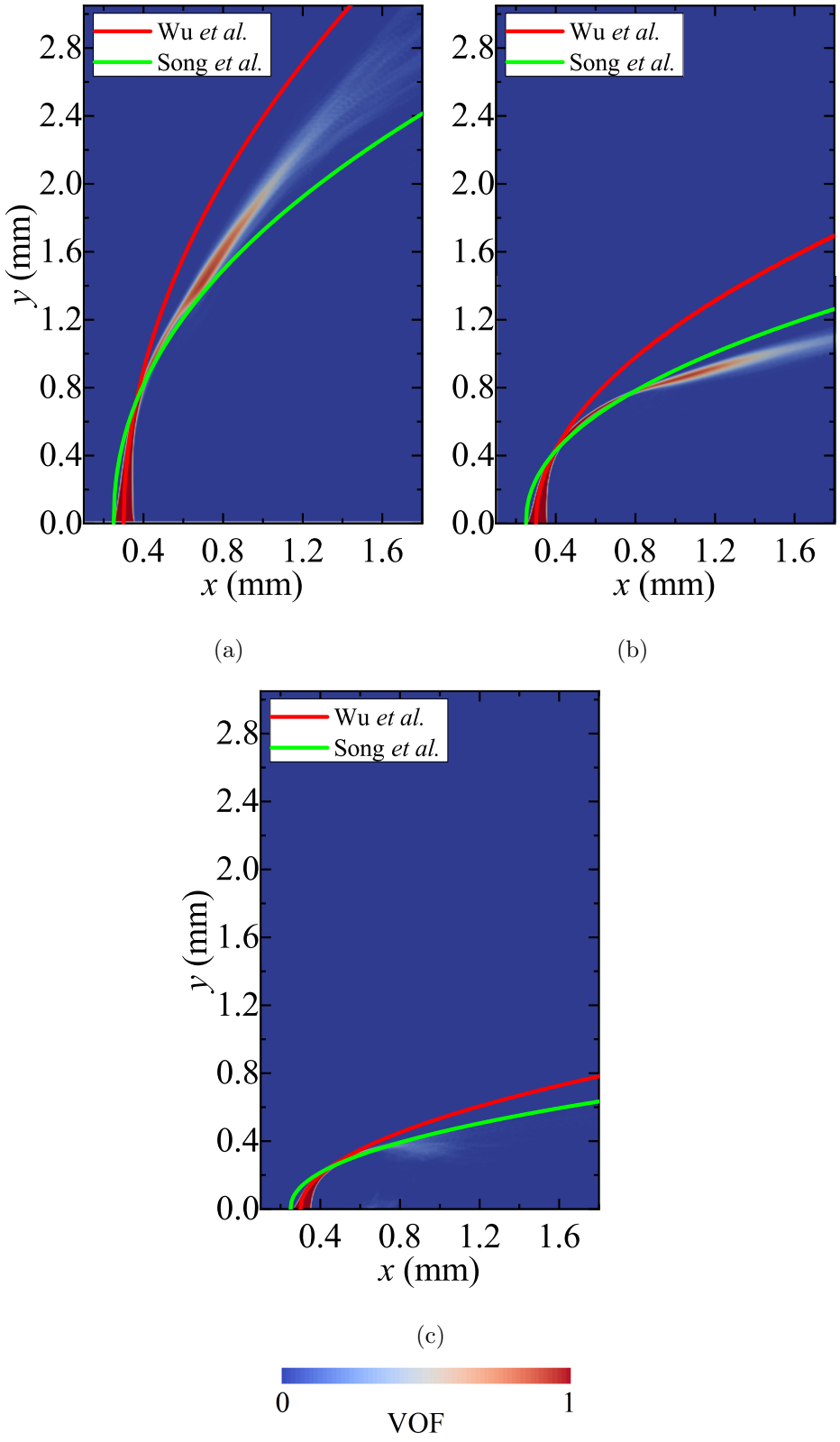

Figure 2.11: Time-averaged liquid jet trajectories on the central $x-y$ plane ($z = 0$ mm): (a) case 3, (b) case 4, (c) case 5.

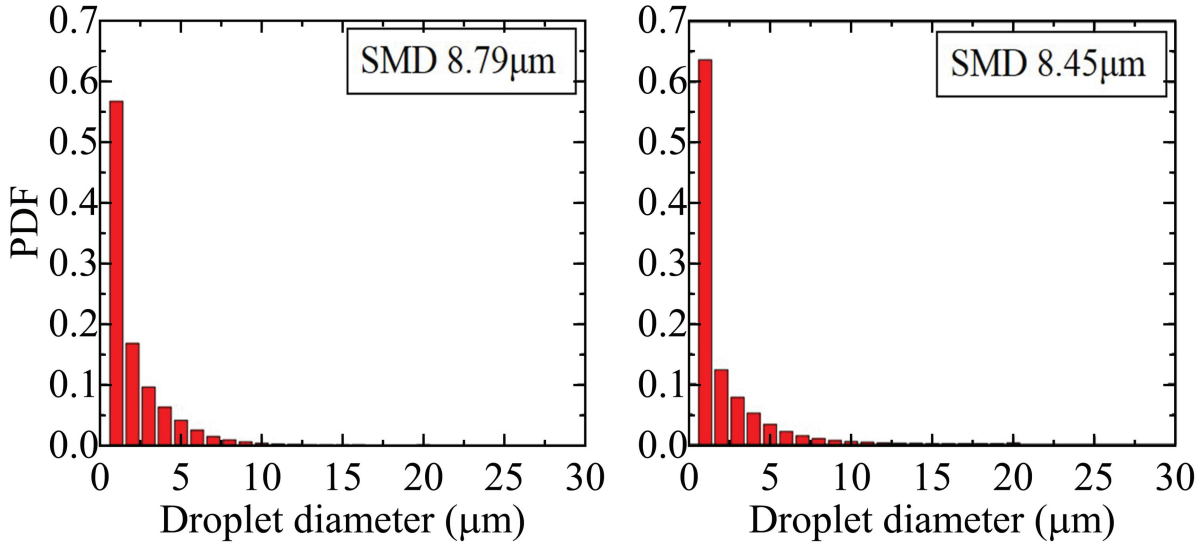

(a)

(b)

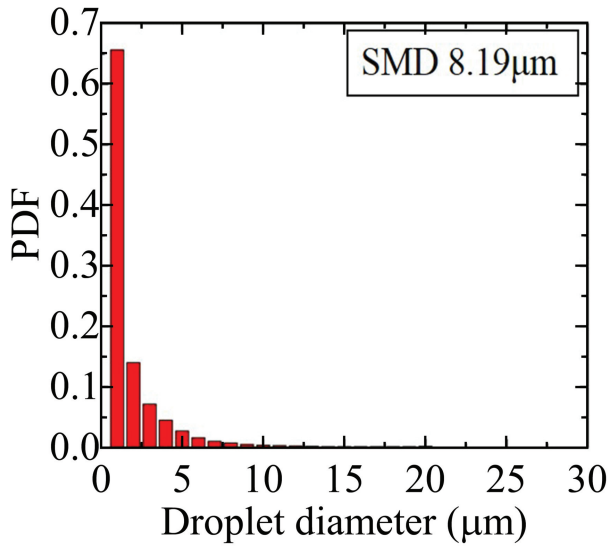

(c)

Figure 2.12: Time-averaged probability density function (PDF) and Sauter mean diameter (SMD) of droplet size in downstream region (1.5 mm $\leqslant x \leqslant$ 1.8 mm): (a) case 3, (b) case 4, (c) case 5.

2.4.3 Flow field behind liquid jet

Fig. 2.13 shows the comparisons of the time-averaged distributions of stream line and vorticity z component ($\omega_z = \partial v/\partial x - \partial u/\partial y$) on the central $x-y$ plane ($z = 0$ mm) among cases 3-5, where green area indicates liquid jet. There are transition points, where the local velocity vectors are perpendicular to the downward liquid-gas interface, for the all three cases as indicated by white circles. Especially for the multimode regime of case 4, the transition point of which definitely divides the flow field behind the liquid jet into two different parts. A counter-clockwise circulation flow is formed in the lower region of the liquid jet as pointed by the red circle, and the blue circle denotes a region where the flow just moves forward downstream directly. It is also found that as the inclination becomes strong with decreasing the liquid-gas momentum flux ratio, M, from the bag mode regime to the shear mode regime, the both flows are enhanced by the increased air flow velocity, and subsequently the transition point shifts to the end part of the liquid jet. This causes the counter-clockwise circulation flow taking the dominant position for the breakup behavior. Another interesting phenomenon should be noted that a clockwise circulation flow beyond the transition point is depicted by the vorticity distribution. It suggests that the liquid jet is gradually torn apart by the enhanced clockwise circulation flow such that the transition point in the shear mode regime of case 5 is far away from the main liquid jet, where the liquid jet has already been broken (see Fig. 2.8(c)).

Fig. 2.14 shows the comparison of the time-averaged distributions of vorticity y component ($\omega_y = \partial u/\partial z - \partial w/\partial x$) on the $x-z$ plane at different heights of $y = 0, 0.3$, and 0.6 mm for case 4, where green area indicates liquid jet. Here, the plane of $y = 0$ is defined as the plane one grid above the wall. Behind the liquid jet, a counter-rotating vortex pair (CVP) is observed. Accordingly, from this CVP and the circulation flows detected in Fig. 2.13, a three-dimensional flow pattern behind the liquid jet is presumed as depicted in Fig. 2.15. Above the transition point, the clockwise circulation flow towards downstream with the CVP, which is referred to as bag breakup vortex (BBV), transports the surface wave downstream leading to bag breakup at the end. Below the transition point, on the other hand, the counter-clockwise circulation flow with the CVP.

which is referred to as shear breakup vortex (SBV), is considered to deflect the vertical velocity of the leeward (see Fig. 2.3) of the liquid jet in the spanwise direction, broaden the liquid jet and enhance the generation of threads for shear breakup.

As mentioned earlier in the previous section, in the bag mode regime of case 3, there appear two big threads, i.e., bifurcations, from the liquid jet surface, which do not seem to associate with the shear breakup, as shown in Figs. 2.8 - 2.10. The similar phenomenon is also observed in the mesh convergence validation with refined uniform mesh size of 2.5 µm which confirms that the bifurcating jets are physical results. It is found that a thin membrane (see. Fig 2.9(a)) is stripped off the liquid jet and eventually forms some larger Eulerian droplets. However, in this condition, the aerodynamic Weber number is so small that the shear force cannot be the main reason to form these distinct bifurcations. Therefore, it is considered that the SBV causes the formation of the bifurcations, that is, the SBV rips a membrane from the liquid jet surface and this membrane develops to the bifurcations by the air flow. As also mentioned above, the SBV deflects the vertical velocity of liquid jet at the leeward into the spanwise direction, which rips a membrane from the liquid jet surface. Subsequently, the air flow presses the generated membrane downstream from the windward (see Fig. 2.8) of the liquid jet. Furthermore, while the air flow passes through the liquid jet, the air pressure alongside the liquid jet is reduced such that the generated membrane is further pressed in the spanwise direction. As a result, the bifurcations are developed just below the transition point. This means that this distinct phenomenon should not be classified as the shear breakup even the behavior looks like it.

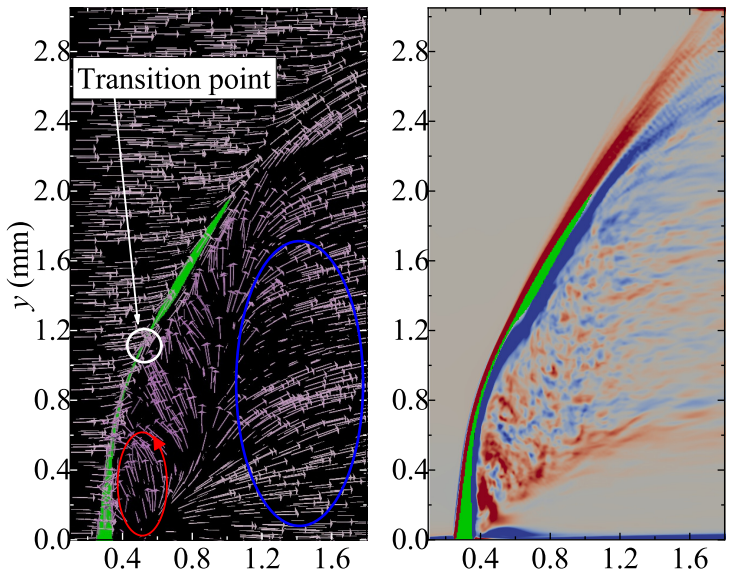

(a)

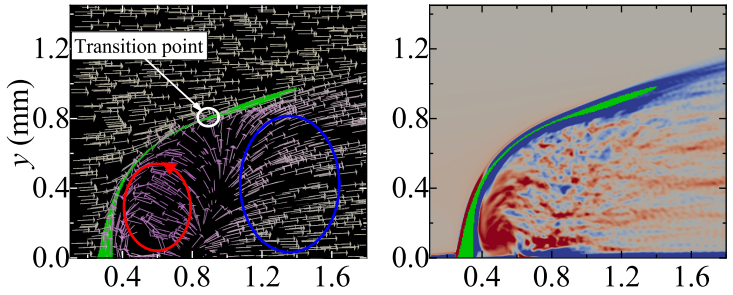

(b)

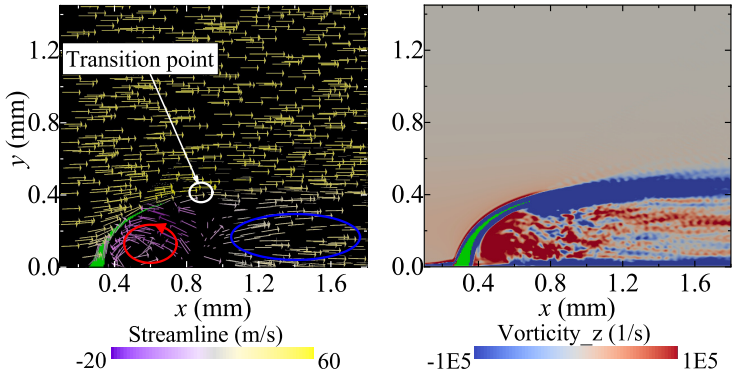

(c)

Figure 2.13: Time-averaged distributions of stream line and z component of vorticity on the central $x-y$ plane ($z = 0$ mm): (a) case 3, (b) case 4, (c) case 5. Green area indicates liquid jet.

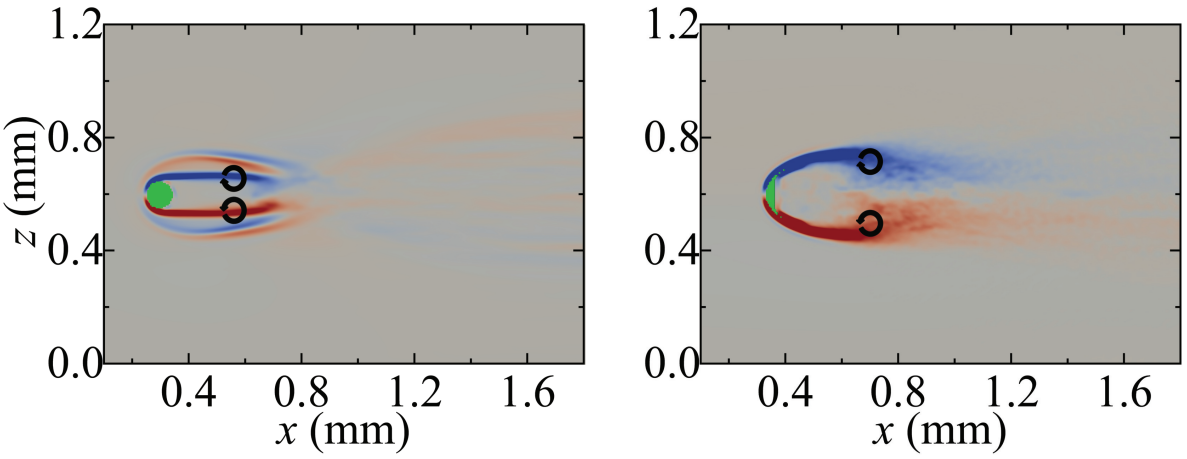

(a)

(b)

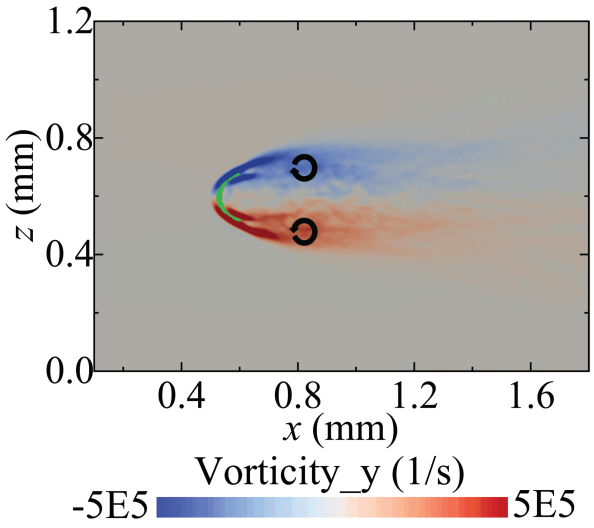

(c)

Figure 2.14: Time-averaged distributions of y component of vorticity on the $x-z$ plane at different heights for case 4: (a) $y = 0$ mm, (b) $y = 0.3$ mm, (c) $y = 0.6$ mm. Green area indicates liquid jet.

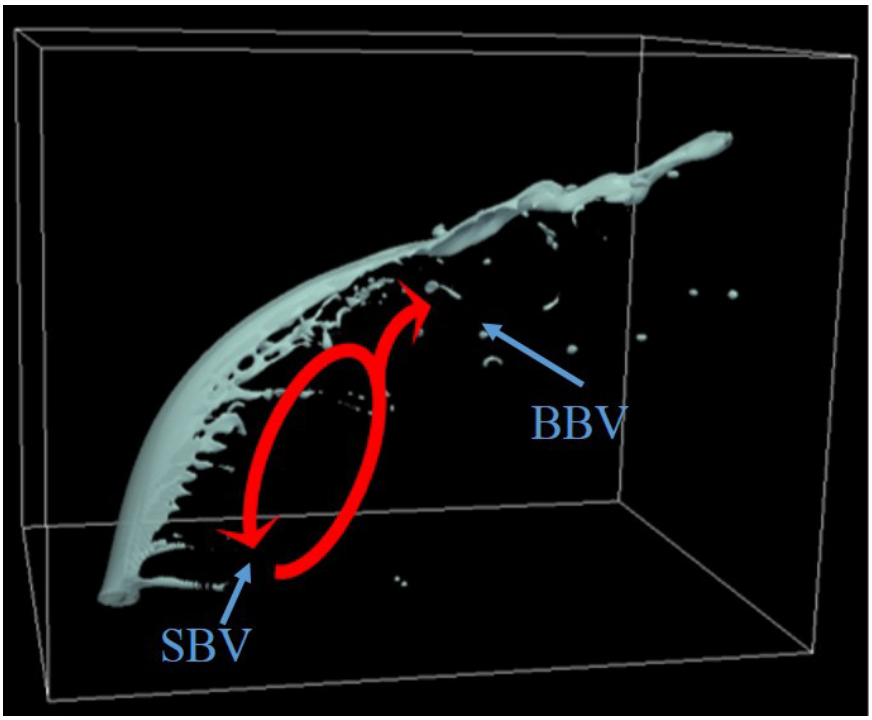

(a)

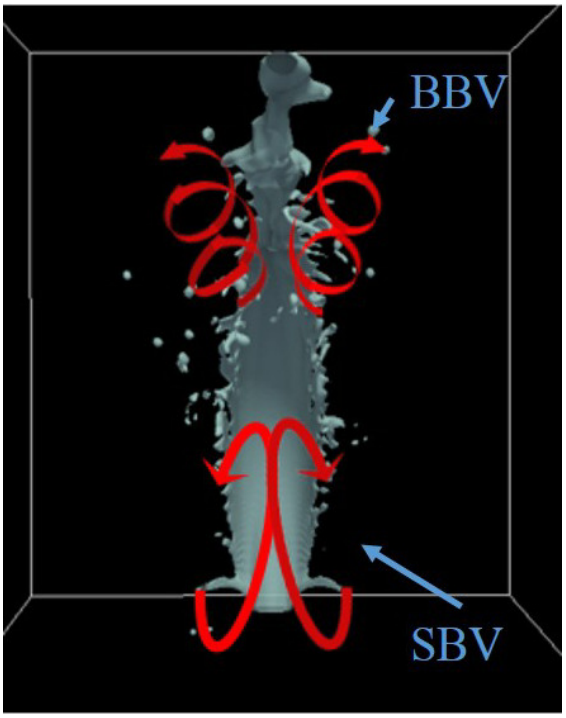

(b)

Figure 2.15: Vortex morphologies of SBV and BBV for case 4: (a) front view, (b) side view.

2.4.4 Evaporation process

Fig. 2.16 shows the comparisons of the time-averaged distributions of droplet number density and evaporation rate on the central $x-y$ plane ($z = 0$ mm) among cases 3-5, where green area indicates liquid jet. Here, because the bifurcations are stretched in the span wise direction (see Fig. 2.10(a)), the generated droplets are not depicted on the central $x-y$ plane. Regarding the droplet number density, the highest number density region in the bag mode regime of case 3 is located in the downstream region of the liquid jet tip, where the bag breakup occurs (see Fig. 2.8(a)). Since these droplets are mainly generated by the BBV, as explained in the previous section, they are simply transported downstream and out of the computational domain. In the multimode regime of case 4, the highest droplet number density region is located just behind the liquid jet around the transition point between the BBV and SBV. These droplets are ones generated both by the bag and shear breakups and transported here by the BBV and SBV. In the shear mode regime of case 5, the high droplet number density regions tend to be located behind the liquid jet, whose trend is similar to that in the multimode regime of case 4, but the highest region is observed in the vicinity of the wall, as indicated by a red circle. This is considered to be the fact that the shear breakup takes the dominant position, in which the crossflow shear force is extremely enhanced and much more threads are created from the liquid jet, such that a large number of droplets exist in this region. Regarding the evaporation rate, the high evaporation rate regions for the bag and shear modes of cases 3 and 5 roughly correspond to the high droplet number density regions and their downstream regions, respectively, which seems reasonable. However, in the multimode regime of case 4, the highest evaporation rate region does not correspond to the highest droplet number density region, that is, it is located not just behind the liquid jet around the transition point but in the vicinity of the wall.

In order to investigate the droplets behaviors and extremely high evaporation rate in the vicinity of the wall for cases 4 and 5 in more detail, Fig. 2.17 shows the time-averaged distributions of droplet number density and evaporation rate on the $x-z$ plane in the vicinity of the wall ($y = 0$ mm) for these two cases. Regarding the droplet

number density, the higher droplet number density regions in the multimode regime of case 4 is located nearby the liquid jet as indicated by the red circle (A), and droplets are transported to the downstream region indicated by the blue circle (B). Here, it is observed that the region B locally displays higher values than that around it. This is considered that the SBV transports the droplets generated in the upper region (see Fig. 2.16(b)) down to these regions. However, in the shear mode regime of case 5, the regions holding higher droplet number density values are places in some different regions. The region A is located further downstream compared to that of case 4, and it seems that the droplets are simply transported downstream from the region A to region B. In addition, two other regions appear as indicated by the yellow circle (C) and purple circle (D), respectively. The region C appearing at the windward of the liquid jet is considered as a result of the enhanced CVP. That is, the CVP in the vicinity of the wall expands from the windward of liquid jet, as shown in Fig. 2.14(a), and this CVP becomes strong and tends to strip a large number of droplets off the windward of the liquid jet as the air flow velocity increases. The region D indicating higher value is obviously caused by the SBV, which transports the upper droplets down to this region. Regarding the evaporation rate, the high evaporation rate regions roughly correspond to the high droplet number density regions and their downstream regions, despite the region D, whose trend is also described earlier in Fig. 2.16(b).

The discrepancy in the location indicating the high value between the droplet number density and evaporation rate can be explained in terms of the temperature and fuel vapor mass fractions as follows. Fig. 2.18 and 2.19 show the comparisons of the time-averaged distributions of fuel vapor mass fraction and temperature on the central $x-y$ plane (z = 0 mm) and in the vicinity of the wall (y = 0 mm), respectively, for cases 4 and 5, where green area indicates liquid jet. It is found that the fuel vapor mass fraction and temperature in the highest droplet number density regions for cases 4 and 5 are high and low, respectively. This suggests that the accommodated fuel vapor with low temperature is trapped by the SBV and acts to suppress the droplet evaporation. Towards the downstream, however, the fuel vapor mass fraction and temperature for

each case gradually decreases and increases, respectively, and the temperature tendency is slightly apparent in the vicinity of the wall, which enhances the evaporation and makes the evaporation rate increase in this region.

Therefore, the evaporation process is strongly dependent on the vortex morphology just behind the liquid jet, i.e., SBV, such that the regions holding higher evaporation rate value change from the upper part in the bag mode regime of case 3 to the vicinity of the wall in the shear mode regime of case 5 as the aerodynamic Weber number increases.

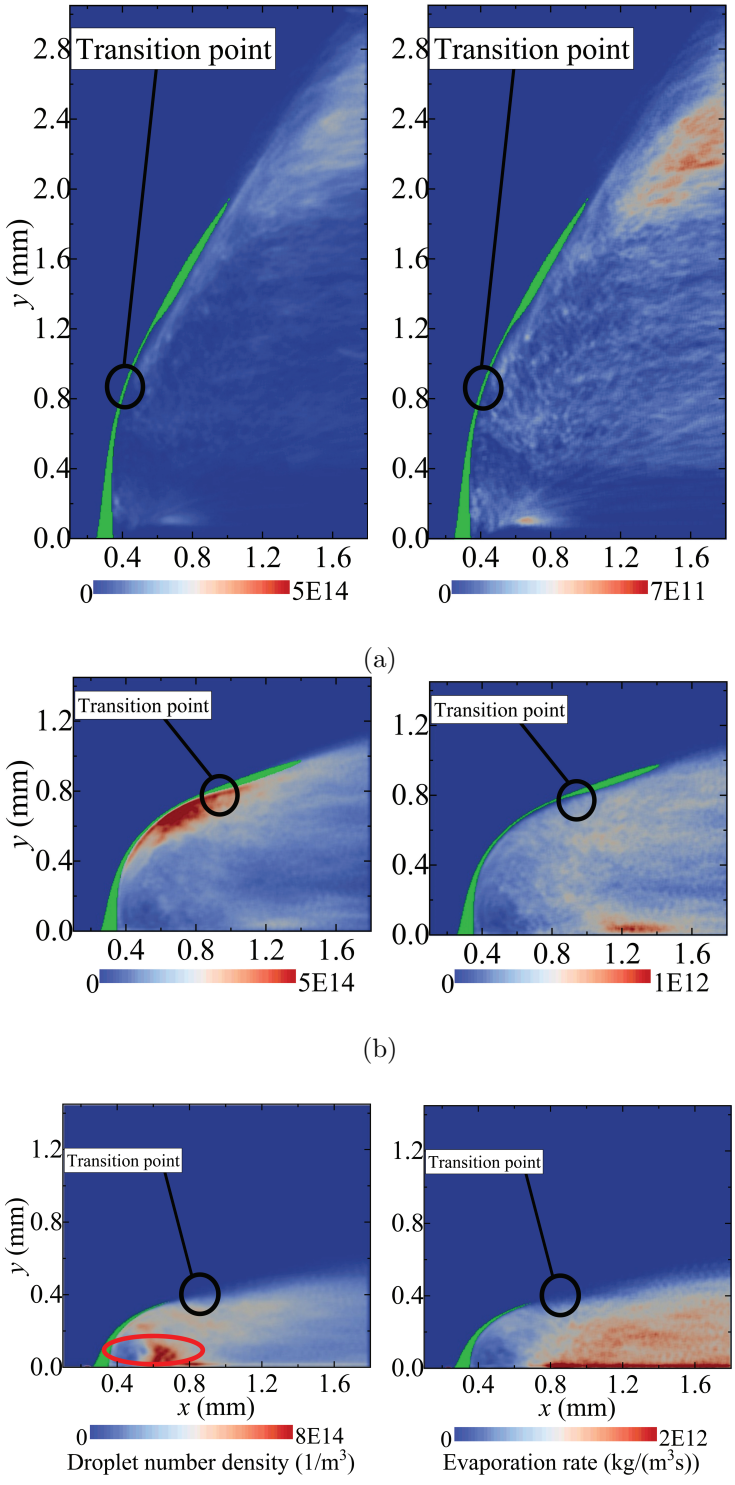

Figure 2.16: Time-averaged distributions of droplet number density n and evaporation rate $\dot{m}$ on the central $x-y$ plane ($z = 0$ mm): (a) case 3, (b) case 4, (c) case 5. Green area indicates liquid jet.

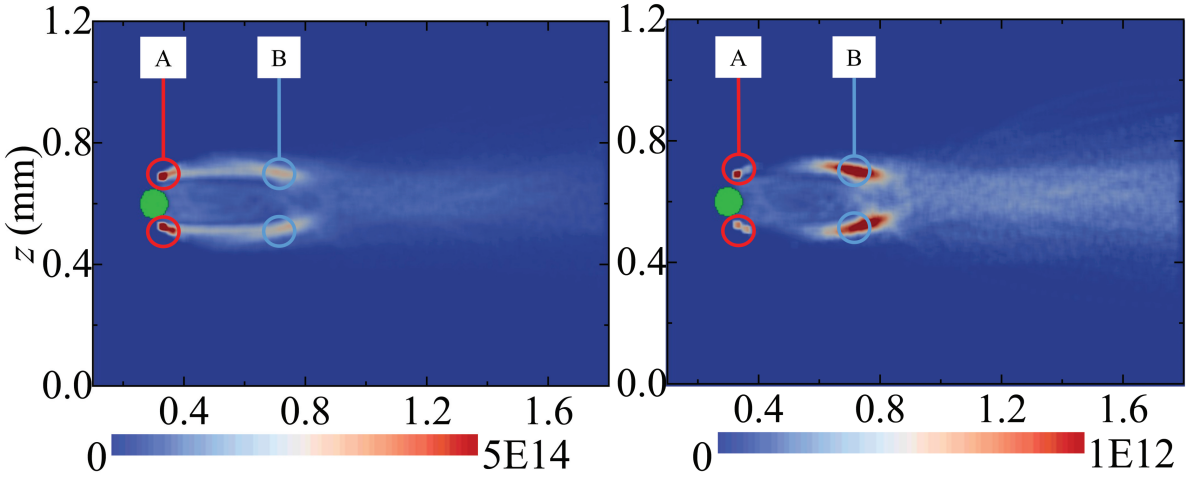

(a)

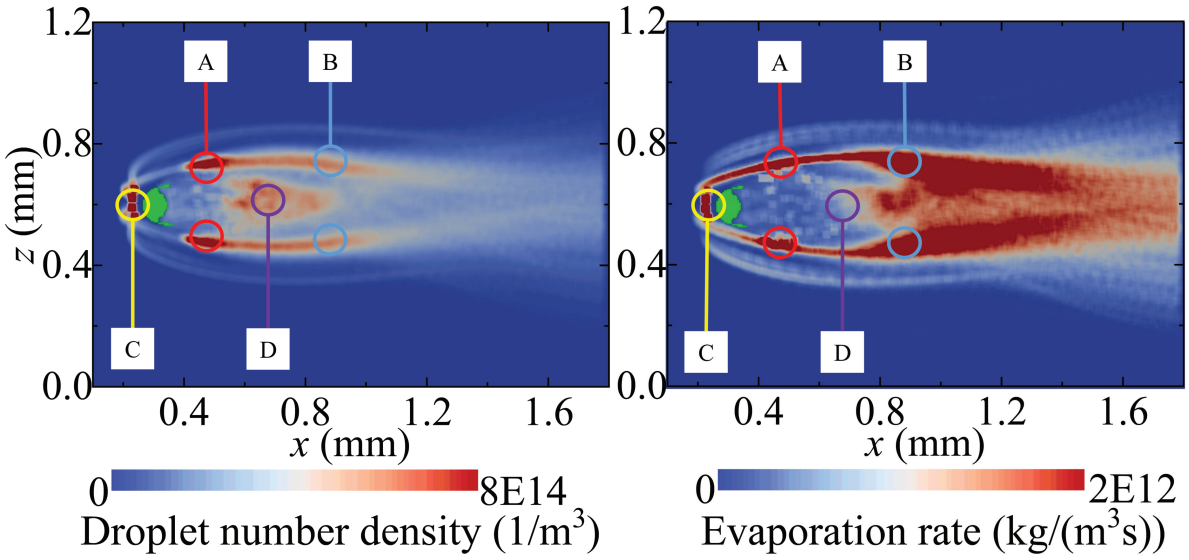

(b)

Figure 2.17: Time-averaged distributions of droplet number density n and evaporation rate $\dot{m}$ on the $x-z$ plane in the vicinity of the wall ($y = 0$ mm): (a) case 4, (b) case 5. Green area indicates liquid jet.

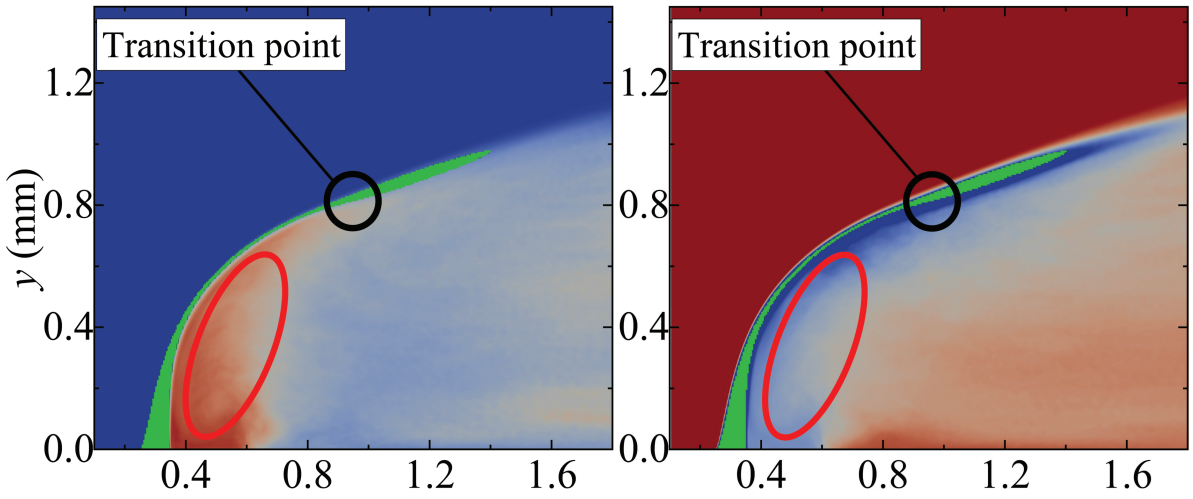

(a)

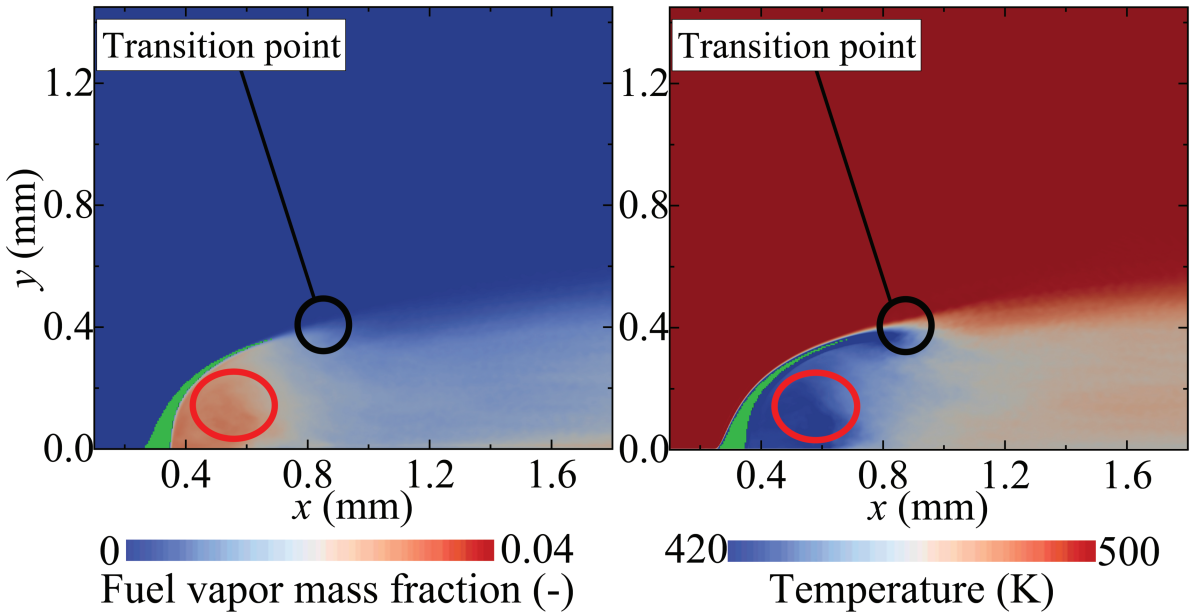

(b)

Figure 2.18: Time-averaged distributions of fuel vapor mass fraction and gas temperature T on the central $x-y$ plane ($z = 0$ mm): (a) case 4, (b) case 5. Green area indicates liquid jet.

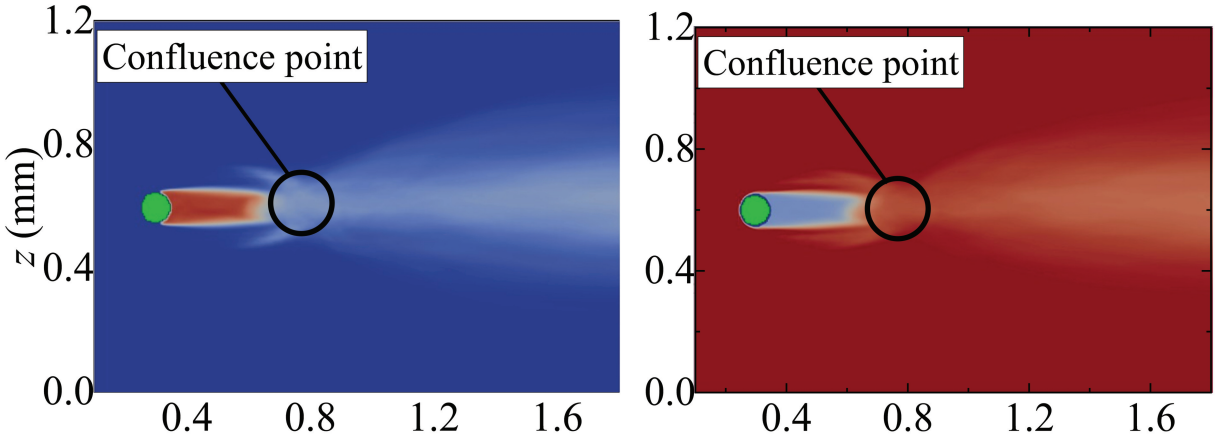

(a)

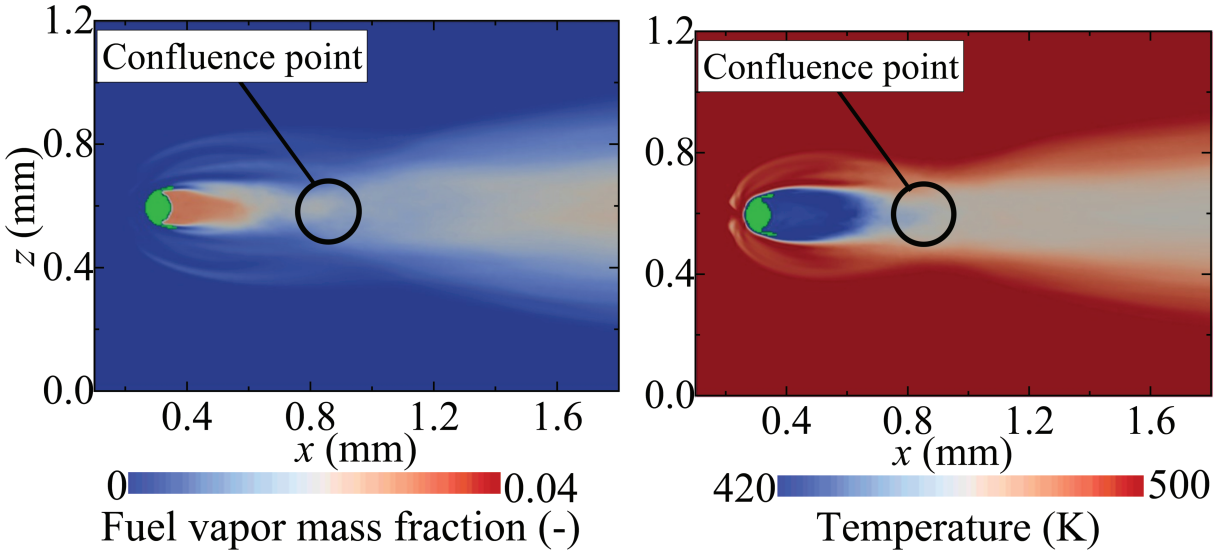

(b)

Figure 2.19: Time-averaged distributions of fuel vapor mass fraction and gas temperature T on the $x-z$ plane in the vicinity of the wall ($y = 0$ mm): (a) case 4, (b) case 5. Green area indicates liquid jet.

2.5 Conclusions

In this chapter, the atomization-evaporation process of a liquid fuel jet in the vicinity of a fuel nozzle in several different steady crossflows under the elevated ambient pressure was investigated by a detailed numerical simulation using an Eulerian-Lagrangian framework under different aerodynamic Weber number conditions. The main results are summarized as follows.

1. The parabolic velocity distribution of the liquid jet in the nozzle has much more penetration force compared to the uniform one because the local liquid-gas momentum flux ratio in the central region of the parabolic case is much larger than that of uniform case and shows the similar liquid jet trajectory to the analytical solution and empirical correlation. This supports the importance of the reproduction of velocity distribution in the nozzle for the precise prediction of the atomization-evaporation process of the liquid jet in crossflows.

2. The present detailed numerical simulation reproduces the primary atomization characteristics of the liquid jet in steady crossflows under different breakup mode regimes, namely bag mode regime, multimode regime, and shear mode regime, respectively, which are consistent with those results in the previous experimental studies. With increasing the aerodynamic Weber number, the shear breakup tends to take the dominant position compared to the bag breakup, leading to smaller Sauter mean diameter (SMD) in the downstream region.

3. The droplets behavior is strongly affected by the circulation flows generated behind the liquid jet, namely, bag breakup vortex (BBV) and shear breakup vortex (SBV). For the case of the bag mode regime, the droplets mainly generated by bag breakup are directly transported downstream by the BBV, and the distinct bifurcations are proved to be the result of the weak SBV deflecting the liquid jet. For the cases of the multimode regime and shear mode regime, on the other hand, the SBV is enhanced, which acts to transport the droplets generated in upper regions to the regions in the vicinity of the wall.

4. The droplet evaporation rate is greatly influenced by the behavior in 3. For the case of bag mode regime, the liquid jet tip downstream holds higher evaporation rate. However, for the cases of multimode regime and shear mode regime, the droplet number density near the wall increases and the evaporation rate there also holds a high value due to the temperature distributions. Furthermore, the SBV traps a large amount of fuel vapor just behind the liquid jet, suppressing the evaporation effect there.

Appendix A. Comparison of liquid jet breakup behavior for different mesh resolutions

The computation with a refined uniform mesh size of 2.5 µm with $400 \times 400 \times 240$ grid points is performed to ensure the atomization behavior, i.e., liquid jet trajectory and droplet size distribution, is properly resolved, which is presented in Fig. 2.20 in comparison to case 2. Here, the case 2 is called 'coarse' with 20 grids per injector diameter and the refined case for the validation is labelled as 'fine' with 40 grids per injector diameter. The jet penetration does not show obvious difference between these two sets of mesh resolution. Furthermore, the comparison of droplet size distributions obtained from the fine and coarse cases are shown in Fig. 2.21. The E-E framework is applied for the fine case, in which the dispersed Eulerian droplets less than one mesh size are eliminated. It can be seen that the computed droplet size distributions are almost similar, which indicates that the Lagrangian droplets with diameter larger than 2.5 µm in the case with coarse mesh is well resolved. Therefore, based on the discussions above, the mesh independence of the present study using the coarse mesh is confirmed.

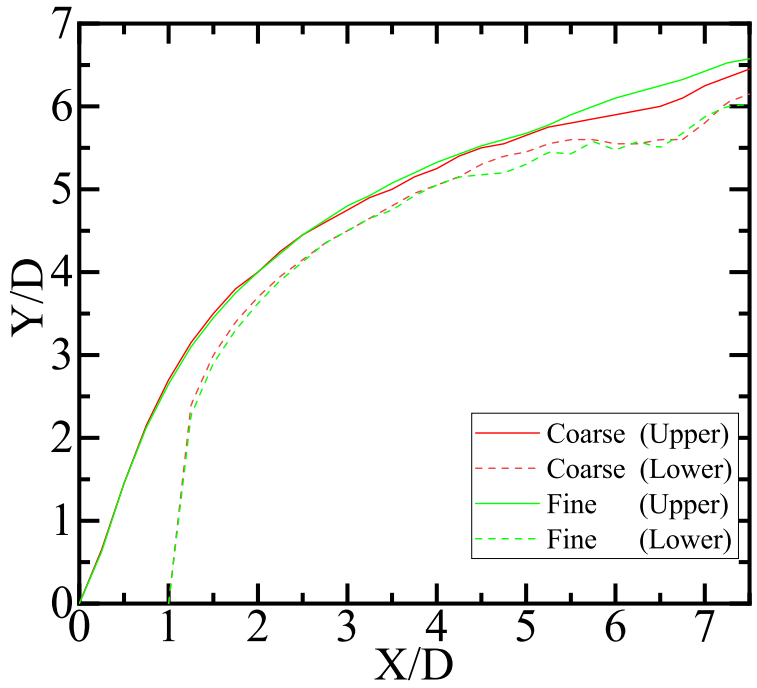

Figure 2.20: Liquid jet trajectories in different mesh size resolutions; green: fine, red: coarse.

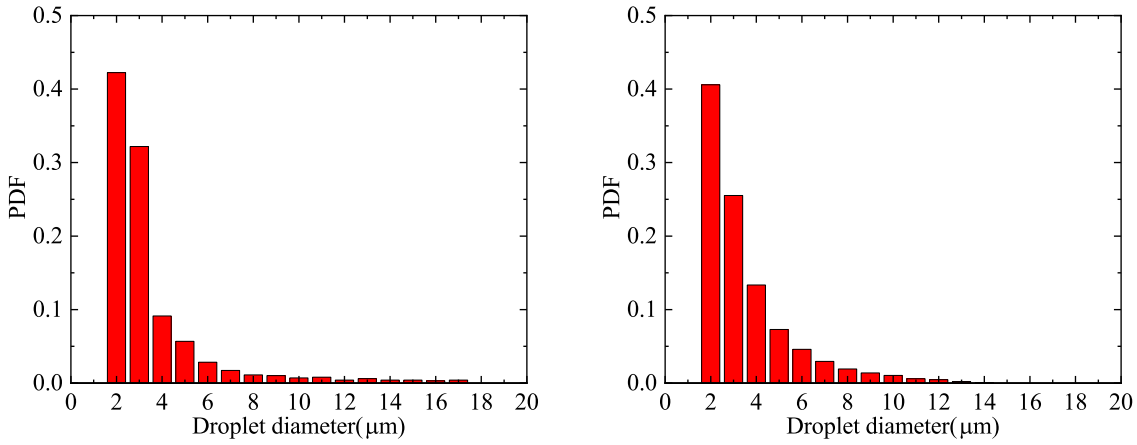

(a) (b)

Figure 2.21: Comparison of PDF of droplet size in different mesh size resolutions: (a) fine, (b) coarse.

Appendix B. Eulerian-Lagrangian droplets transformation

In this work, the E-L coupling method to reduce the computational cost is employed. Within this method, the effectiveness of the tagging method is important and is detailed here. The droplet size distribution at the instance of Eulerian droplets transformed to Lagrangian droplets is presented, and the mass conservation of this method is checked in this section. Firstly, the non-evaporation case under the E-L framework is computed till the 10,000th step with eliminating the dispersed Eulerian droplets less than one mesh size. Then, the computation for the 10,001st step is carried out by using both the E-E framework and the E-L framework, respectively, to validate the tagging method by comparing the droplet diameter distributions in the whole domain, which are shown in Fig. 2.22. A good agreement between two calculations is observed, which confirms that the tagging method utilized could properly transform the Eulerian droplets into Lagrangian droplets, and most of the small droplets could thus be considered as mesh independent. Note that the droplets with diameter larger than 20 μm are still considered as the Eulerian droplets in both cases. By this tagging method, the liquid phase mass conservation is also checked as shown in Fig. 2.23, averaging the time period from the 10000th step to 15000th step. The liquid phase mass loss of E-L framework is 0.00737% which shows superior compared to that of the E-E framework of 9.77%.

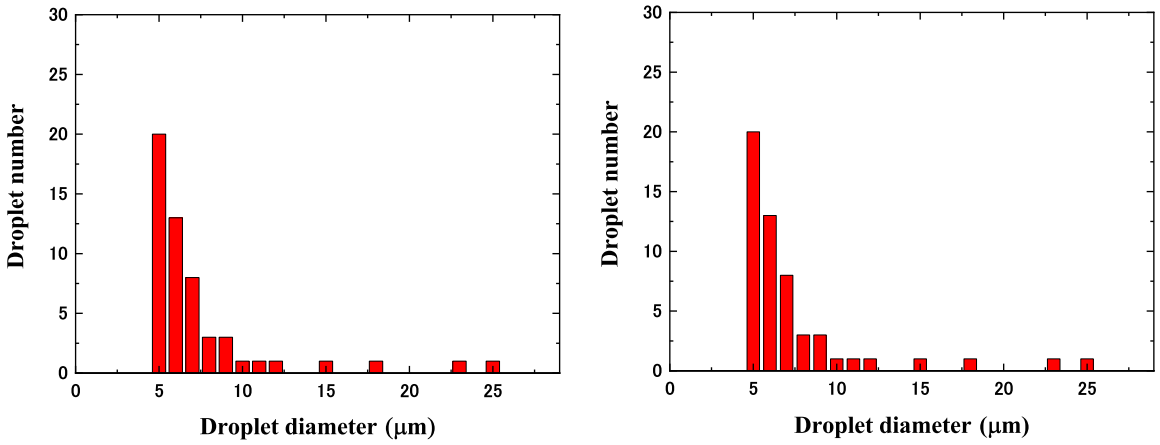

(a) (b)

Figure 2.22: Validation for E-L tagging method by comparing droplet diameter distribution in the whole domain: (a) E-E, (b) E-L.

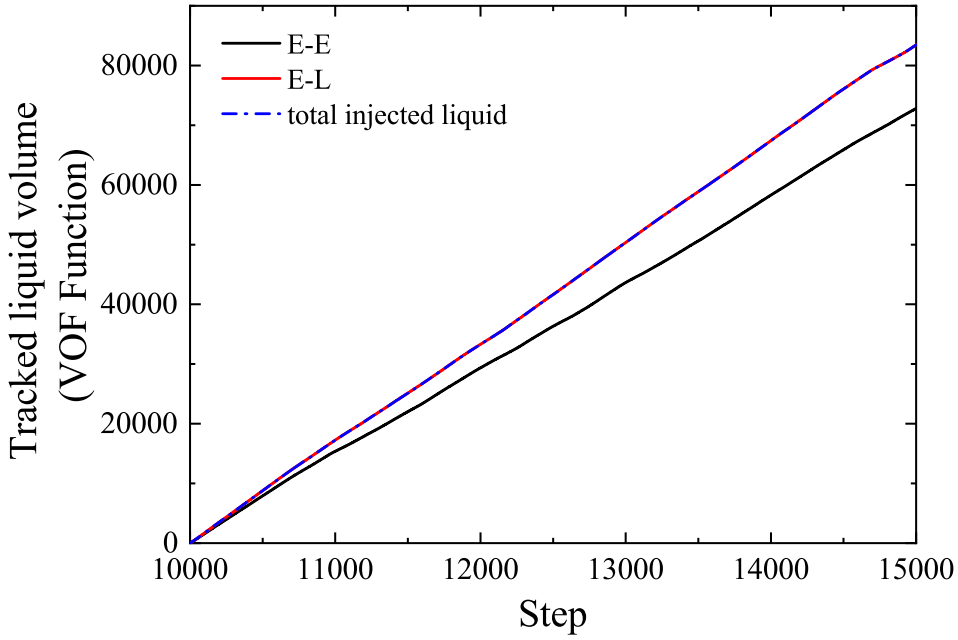

Figure 2.23: Injected liquid jet mass conservation validation for E-E and E-L frameworks.

References

[1] H. Watanabe, R. Kurose, S. Komori, and H. Pitsch. Effects of radiation on spray flame characteristics and soot formation. *Combust. Flame*, 152:2–13, 2008.

[2] S. Tachibana, K. Saito, T. Yamamoto, M. Makida, T. Kitano, and R. Kurose. Experimental and numerical investigation of thermos-acoustic instability in a liquid-fuel aero-engine combustor at elevated pressure: validity of large-eddy simulation of spray combustion. *Combust. Flame*, 162:2621–2637, 2015.

[3] T. Kitano, T. Tsuji, R. Kurose, and S. Komori. Effect of pressure oscillations on flashback characteristics in a turbulent channel flow. *Energy. Fuel*, 29:6815–6822, 2015.

[4] A. Pillai and R. Kurose. Combustion noise analysis of a turbulent spray flame using a hybrid dns/ape-rf approach. *Combust. Flame*, 200:168–191, 2019.

[5] P. Wu, K. Kirkendall, R. Fuller, and A. Nejad. Breakup processes of liquid jets in subsonic crossflows. *J. Propuls. Power*, 13:64–73, 1997.

[6] K. Sallam, C. Aalburg, and G. Faeth. Breakup of round nonturbulent liquid jets in gaseous crossflow. *AIAA J.*, 42:2529–2540, 2004.

[7] S. Tambe, S. Jeng, H. Mongia, and G. Hsiao. Liquid jets in subsonic crossflow. *43rd AIAA ASME*, AIAA2005–731, 2005.

[8] P. Eriksson, R. Orbay, and J. Klingmann. Experimental investigations of a low weber liquid spray in air cross flow. *ICLASS2006*, ICLASS06–277, 2006.

[9] J. Stenzler, J. Lee, D. Santavicca, and W. Lee. Penetration of liquid jets in a cross-flow. *Atomiz. Sprays*, 16:887–906, 2006.

[10] M. Herrmann. Detailed numerical simulations of the primary atomization of a turbulent liquid jet in crossflow. *J. Eng. Gas Turbines Power*, 132:061506, 2010.

[11] M. Herrmann. The influence of density ratio on the primary atomization of a turbulent liquid jet in crossflow. *P. Combust. Inst.*, 33:2079–2088, 2011.

[12] S. Ghods. *Detailed numerical simulation of liquid jet in crossflow atomization with high density ratios*. PhD thesis, Arizona State University, Tempe, USA, 2013.

[13] X. Li and M. Soteriou. High fidelity simulation and analysis of liquid jet atomization in a gaseous crossflow at intermediate weber numbers. *Phys. Fluids*, 28:082101, 2016.

[14] X. Li, H. Gao, and M. Soteriou. Investigation of the impact of high liquid viscosity on jet atomization in crossflow via high-fidelity simulations. *Phys. Fluids*, 29:082103, 2017.

[15] X. Li and M. Soteriou. Detailed numerical simulation of liquid jet atomization in crossflow of increasing density. *Int. J. Multiphas. Flow*, 104:214–232, 2018.

[16] J. Song, C. Cain, and J. Lee. Liquid jets in subsonic air crossflow at elevated pressure. *J. Eng. Gas Turb. Power Trans Asme*, 041502, 2015.

[17] R. Ragucci, A. Bellofiore, and A. Cavaliere. Breakup and breakdown of bent kerosene jets in gas turbine conditions. *Proc. Combust. Inst.*, 31:2231–2338, 2007.

[18] S. Freitag and C. Hassa. Spray characteristics of a kerosene jet in cross flow of air at elevated pressure. *ILASS2008*, ILASS08–12–1, 2008.

[19] A. Amighi, M. Eslamian, and N. Ashgriz. Trajectory of a liquid jet in high pressure and high temperature subsonic air crossflow. *ICLASS*, 2009.

[20] M. Owkes and O. Desjardins. A computational framework for conservative, three-dimensional, unsplit, geometric transport with application to the volume-of-fluid (vof) method. *J. Comput. Phys.*, 270:587–612, 2014.

[21] D. Fuster, T. Arrufat, M. Esposito, Y. Ling, L. Malan, S. Pal, R. Scardovelli, G. Tryggvason, and S. Zaleski. A momentum-conserving, consistent, volume-

of-fluid method for incompressible flow on staggered grids. *arXiv:1811.12327 [Physics.comp-ph]*, 2020.

[22] D. Zuzio, A. Orazzo, J. Estivalèzes, and I. Lagrange. A new efficient momentum preserving level-set/vof method for high density and momentum ratio incompressible two-phase flows. *J. Comput. Phys.*, 410:109342, 2020.

[23] S. Matsushita and T. Aoki. A weakly compressible scheme with a diffuse-interface method for low mach number two-phase flows. *J. Copmut. Phys.*, 376:838–862, 2019.

[24] R. Miller, K. Harstad, and J. Bellan. Evaluation of equilibrium and non-equilibrium evaporation models for many-droplet gas-liquid flow simulations. *Int. J. Multiphas. Flow*, 24:1025–1055, 1998.

[25] R. Miller and J. Bellan. Direct numerical simulation of a confined three-dimensional gas mixing layer with one evaporating hydrocarbon-droplet-laden stream. *J. Fluid Mech.*, 384:293–339, 1999.

[26] T. Kitano, J. Nishio, R. Kurose, and S. Komori. Evaporation and combustion of multicomponent fuel droplets. *Fuel*, 136:219–225, 2014.

[27] T. Kitano, J. Nishio, R. Kurose, and S. Komori. Effects of ambient pressure, gas temperature and combustion reaction on droplet evaporation. *Combust. Flame*, 161:551–564, 2014.

[28] N. Takagaki, R. Kurose, Y. Baba, Y. Nakajima, and S. Komori. Relationship between momentum of an impinging drop and intensities of vortex rings generated below free surface. *Int. J. Multiphas. Flow*, 65:1–10, 2014.

[29] T. Kitano, K. Kaneko, R. Kurose, and S. Komori. Large-eddy simulations of gas- and liquid-fueled combustion instabilities in back-step flows. *Combust. Flame*, 170:63–78, 2016.

[30] U. Ahmed, A. Pillai, N. Chakraborty, and R. Kurose. Statistical behavior of turbulent kinetic energy transport in boundary layer flashback of hydrogen-rich premixed combustion. *Phys. Rev. F.*, 4:103201, 2019.

[31] C. Crowe, M. Sharma, and D. Stock. The particle-source-in cell (psi-cell) model for gas-droplet flows. *J. Fluid Eng. Trans. Asme*, 99:325–332, 1977.

[32] R. Kurose, R. Misumi, and S. Komori. Drag and lift forces acting on a bubble in a linear shear flow. *Int. J. Multiphas. Flow*, 27:1247–1258, 2001.

[33] R. Kurose, H. Makino, S. Komori, M. Nakamura, F. Akamatsu, and M. Katsuki. Effects of outflow from the surface of a sphere on drag, shear lift, and scalar diffusion. *Phys. Fluids*, 15:2338–2351, 2003.

[34] H. Watanabe, R. Kurose, S. Huang, and F. Akamatsu. Characteristics of flamelets in spray flames formed in a laminar counterflow. *Combust. Flame*, 148:234–248, 2007.

[35] K. Watson. Thermodynamics of the liquid state. *Indust. Eng. Chem.*, 35:398–406, 1943.

[36] S. Mirjalili, S. Jain, and M. Dodd. Interface-capturing method for two-phase flow: An overview and recent developments. *CTR Ann. Res. Briefs*, 117–135, 2017.

[37] K. Yokoi. Efficient implementation of thinc scheme: a simple and practical smoothed vof algorithm. *J. Comput. Phys.*, 226:1985–2002, 2007.

[38] K. Yokoi. A numerical method for free-surface flows and its application to droplet impact on a thin liquid layer. *J. Sci. Comput.*, 35:372–396, 2008.

[39] K. Yokoi. A practical numerical framework for free surface flows based on clsvof method, multi-moment methods and density-scaled csf model: numerical simulations of droplet splashing. *J. Comput. Phys.*, 232:252–271, 2013.

[40] A. Albadawi, D. Donoghue, A. Robinson, D. Murray, and Y. Delauré. Influence of surface tension implementation in volume of fluid and coupled volume of fluid with level set methods for bubble growth and detachment. *Int. J. Multiphas. Flow*, 53:11–28, 2013.

[41] M. Sussman, P. Smereka, and S. Osher. A level set approach for computing solutions to incompressible two-phase flow. *J. Comput. Phys.*, 114:146–159, 1994.

[42] J. Brackbill, D. Kothe, and C. Zemach. A continuum method for modeling surface tension. *J. Comput. Phys.*, 100:335–354, 1992.

[43] M. Herrmann. A balanced force refined level set grid method for two-phase flows on unstructured flow solver grids. *J. Comput. Phys.*, 227:2674–2706, 2008.

[44] M. Herrmann. A parallel eulerian interface tracking/lagrangian point particle multiscale coupling procedure. *J. Comput. Phys.*, 229:745–759, 2010.

[45] D. Zuzio, J. Estivalèzes, and B. DiPierro. An improved multiscale eulerian-lagrangian method for simulation of atomization process. *Comput. Fluids*, 176:285–301, 2018.

[46] X. Li, M. Soteriou, M. Arienti, and M. Sussman. High-fidelity simulation of atomization and evaporation in a liquid jet in cross-flow. *49th AIAA Aerospace Sciences Meeting including the New Horizons Forum and Aerospace Exposition*, AIAA2011–99, 2011.

[47] R. Prakash, S. Jain, J. Lovett, B. Raghunandan, R. Ravikrishna, and G. Tomar. Detailed numerical simulation of atomization of a liquid jet in a swirling gas crossflow. *Atomiz. Sprays*, 2019.

[48] X. Li, M. Soteriou, W. Kim, and J. Cohen. High fidelity simulation of the spray generated by a realistic swirling flow injector. *J. Eng. Gas Turb. Power*, 136:071503, 2014.

[49] D. Sedarsky, M. Paciaroni, E. Berrocal, P. Petterson, J. Zelina, J. Gord, and M. Linne. Model validation image data for breakup of a liquid jet in crossflow: part i. *Exp. Fluids*, 49:391–408, 2010.

Nomenclature

B_M	: Mass transfer number [-]	α	: Droplet sphericity [-]
c_p	: Specific heat capacity [J/(K·kg)]	β	: Evaporation parameter [-]
d	: Diameter [m]	Γ	: Interface thickness [m]
D	: Diffusion coefficient [m^2/s]	ϵ	: TKE dissipation rate [m^2/s^3]
D_{inj}	: Nozzle injector diameter [m]	η_H	: Hinze scale [m]
f_1	: Correction of Stokes drag [-]	η_K	: Kolmogorov scale [m]
f_2	: Correction of heat transfer [-]	κ	: Local curvature of interface [1/m]
$F_{\boldsymbol{\sigma}}$	: Body force of surface tension [N]	λ	: Thermal conductivity [W/(m·K)]
h	: Enthalpy [J/kg]	μ	: Viscosity [Pa·s]
H	: Heaviside function [-]	ρ	: Density [kg/m^3]
L_K	: Knudsen layer thickness [m]	σ	: Surface tension [N/m]
L_V	: Latent heat [J/kg]	τ	: Response time [s]
m	: Mass [kg]	$\boldsymbol{\tau}$	: Stress tensor [N/m^2]
M	: Liquid-gas momentum flux ratio [-]	φ	: Levelset function [-]
n	: Droplet number density [-]	ψ	: VOF function [-]
$\boldsymbol{n}_\varphi$	: local normal vector of interface [-]	ω	: Vorticity [1/s]
N	: Number of droplets in a grid [-]	**Subscripts**	
Nu	: Nusselt number [-]	0	: Initial value
Oh	: Ohnesorge number [-]	atm	: Atmospheric value
P	: Pressure [Pa]	b	: Blowing value
Pr	: Prandtl number [-]	B	: Boiling point
r	: Radius [m]	c	: Critical point
R	: Gas constant [J/(K·mol)]	d	: Droplet's value
Re	: Reynolds number [-]	eff	: Effective value
S	: Source term	F	: Fuel

Sc	: Schmidt number [-]	g	: Gas phase value
Sh	: Sherwood number [-]	ii	: grid number of droplet
t	: Time [s]	k	: Chemical species k
T	: Temperature [K]	l	: Liquid phase value
$\boldsymbol{u}$	: Velocity [m/s]	max	: Maximum value
V	: Volume [m^3]	s	: Droplet surface
W	: Mole weight [kg/mol]	sat	: Saturated value
We	: Aerodynamic Weber number [-]	sl	: Slip value
X	: Mole fraction [-]	Γ	: Interface value
$\boldsymbol{x}$	: Position [m]	**Superscripts**	
Y	: Mass fraction [-]	n	: step number

Chapter 3

VOF simulation of atomization and evaporation of liquid fuel jets in crossflows: Effect of oscillating airflow

3.1 Introduction

In this chapter, the atomization-evaporation process of a liquid fuel jet in the oscillating crossflow under the elevated ambient pressure is investigated in comparison to that in a steady crossflow by using a detailed numerical simulation. For the detailed numerical simulation of spray atomization, the E-L framework proposed in the previous chapter is employed.

Combustion instability poses the primary technical challenge for engine design because of its capacity causing catastrophic damage to the combustor. Combustion instability either in gas combustion or spray combustion has been studied experimentally [1–3] and numerically [4–6], which confirms that the phase difference between the oscillations of pressure and heat release rate has significant influence on combustion characteristics. Tachibana et al. [4] performed a LES of combustion instability in spray combustion and

found that the thermo-acoustics induced by the unstable combustion could affect the fuel atomization process, providing positive or negative feedback to damp or amplify the combustion instability. Kitano et al. [5] and Pillai et al [6] also investigated the combustion instability in spray combustion under various combustion conditions by numerical approaches and found that a comprehensive understanding of the spray atomization and combustion could suggest an effective method to control the combustion instability.

However, these numerical simulations are conducted on the assumption of dilute spray flames without considering the detailed atomization process in the dense spray region. As mentioned in the previous chapter, the limitation of optical diagnostics in the dense spray region makes it difficult to investigate the primary breakup of the atomization process. Therefore, the experimental researches on the spray atomization in oscillating crossflows are very limited. Bunce et al. [7] and Song et al. [8, 9] conducted several experiments to investigate the atomization behaviors of liquid jets in crossflows, but they obtained totally different conclusions on the relationship of phase difference and frequency dependence. In addition, the size distributions of droplets generated in the spray atomization in the different oscillating flow frequencies show different results in Song's work [8, 9], for which the reason is not elaborated yet. Moreover, the detailed mechanism of such complex interaction between atomization and crossflow oscillation in the spray dense region, has not been understood due to the complexity of its flow field and the limitation of experimental measurement. Regarding the numerical simulation, the accurate prediction of such complicated atomization pattern is still a challenge for the current computation models. Therefore, there are no numerical simulations investigating the influence of the oscillating air flow conditions on the atomization-evaporation process of liquid jets in crossflows.

The purpose of this chapter is, therefore, to investigate the atomization-evaporation process of a liquid fuel jet in the oscillating crossflow under the elevated ambient pressure in comparison to that in a steady crossflow to figure out how the crossflow oscillation affects the liquid breakup, droplet transportation and evaporation. The E-L framework, proposed in the previous chapter, is employed to capture the atomization behavior and

droplet evaporation by using the CLSVOF method and the non-equilibrium Langmuir-Knudsen evaporation model, respectively.

3.2 Numerical simulation methods

3.2.1 Governing equations for Eulerian framework

In present detailed numerical simulation, both liquid and gas phases are solved in the Eulerian framework and are treated as incompressible fluids. The governing equations used in the present calculation are the conservation equations of mass, momentum, energy, and mass fraction of chemical species applied to the study by using in-house code, FK^3 [5, 6, 10–12].

$$\rho \nabla \cdot \boldsymbol{u} = S_\rho, \tag{3.1}$$

$$\rho(\frac{\partial \boldsymbol{u}}{\partial t} + \boldsymbol{u} \cdot \nabla \boldsymbol{u}) = -\nabla P + \nabla \cdot \boldsymbol{\tau} + \boldsymbol{F}_\sigma + S_\rho, \tag{3.2}$$

$$\rho[\frac{\partial h}{\partial t} + \nabla \cdot (\boldsymbol{u}h)] = \nabla \cdot (\frac{\lambda}{c_p} \nabla h) + S_{\rho h}, \tag{3.3}$$

$$\rho[\frac{\partial Y_k}{\partial t} + \nabla \cdot (\boldsymbol{u}Y_k)] = \nabla \cdot (D_k \nabla Y_k) + S_{\rho Y_k}. \tag{3.4}$$

Here, ρ is the density, $\boldsymbol{u}$ the velocity, P the pressure, μ the viscosity, $\boldsymbol{\tau}$ the viscous stress tensor, $\boldsymbol{F}_\sigma$ the source term of surface tension, h the enthalpy, λ and c_p are the thermal conductivity and specific heat capacity at constant pressure, respectively. Y_k and D_k are the mass fraction and mass diffusion coefficient of chemical species k, respectively. Eqs. 3.1 and 3.2 are employed for both gas and liquid phases, while Eqs. 3.3 and 3.4 are only employed for the gas phase. S_ρ, $S_{\rho u}$, $S_{\rho h}$, and $S_{\rho Y_k}$ are the source terms of mass, momentum, energy, and chemical species, respectively, which could be found in the FK^3 works as well as in Chapter 2.

An E-L tagging method [13] is utilized to transform the Eulerian droplet into a Lagrangian droplet to couple the Eulerian solution with the Lagrangian droplet tracking, and the threshold of droplet diameter of the E-L transformation from Eulerian droplets to Lagrangian droplets are set to be 4 grids length. The two-way coupling is retained for interphase interactions, and a CLSVOF method [14, 15] is adopted to accurately capture the liquid-gas interface. The body force at the liquid-gas interface due to surface tension is accounted for by the CSF model [16]. The droplet-interface collision as well as the

momentum conservation for the transformed Lagrangian droplets are also considered by referring to the work [17].

3.2.2 Governing equations for Lagrangian framework

The dispersed droplets generated by the Eulerian framework are transformed into Lagrangian droplets by the E-L coupling, and then tracked in the Lagrangian framework. For the droplet evaporation, a non-equilibrium Langmuir-Knudsen evaporation model is used. Therefore, the governing equations for tracking the profiles of droplets such as the position, velocity, temperature, and mass of each droplet are given as follows [18–21].

$$\frac{d\boldsymbol{x}_d}{dt} = \boldsymbol{u}_d, \tag{3.5}$$

$$\frac{d\boldsymbol{u}_d}{dt} = \frac{f_1}{\tau_d}(\boldsymbol{u} - \boldsymbol{u}_d), \tag{3.6}$$

$$\frac{dT_d}{dt} = \frac{Nu}{3Pr}\frac{c_p}{c_{p,d}}\frac{f_2}{\tau_d}(T - T_d) + \frac{1}{m_d}\frac{dm_d}{dt}\frac{L_V}{c_{p,d}}, \tag{3.7}$$

$$\frac{dm_d}{dt} = \dot{m}_d. \tag{3.8}$$

Here, $\boldsymbol{x}_d$, $\boldsymbol{u}_d$, T_d, and m_d are the position, velocity, temperature, and mass of the Lagrangian droplet, respectively. T is the gas temperature, $c_{p,d}$ the specific heat capacity of the droplet at constant pressure, L_V the latent heat of evaporation at T_d, $\dot{m}_d$ the evaporation rate f_1, f_2, and τ_d are the correction coefficients of Stokes drag, heat transfer, [22, 23] and response time for the droplet, respectively. Pr the Prandtl number, Nu the Nusselt number.

The gas phase has been proved to be a direct numerical simulation work and the generated droplets are considered to be mesh independent as explained in the previous chapter. The evaporation model for dispersed droplets applied in present work has been validated in our previous works [20, 21].

3.3 Computational setup

3.3.1 Computational domains

Figure 3.1(a) shows the computational domain for the crossflow atomization simulations, considering the liquid jet injected vertically interfered by the transverse oscillating air flow. The computational domain is set to be an open space with a non-slip boundary wall at the bottom, the height of which is 0.15 mm for the liquid jet velocity development in the nozzle. A jet nozzle with diameter $D_{inj} = 0.1$ mm is mounted. A total number of 27.6 million grid points and 360 × 320 × 240 grids in three directions x−, $y-$, and $z-$, respectively, of a Cartesian coordinate are employed for the discretization of a computational domain. The uniform mesh size of 5 µm is utilized, thus leading a physical domain of 1.8 mm × 1.6 mm × 1.2 mm. The mesh independence of the present computation by adopting a refined mesh of 400 × 400 × 240 grids with uniform mesh size of 2.5 µm is presented in the previous chapter such that the computed liquid jet trajectory and droplet size distribution are both found to be well resolved.

3.3.2 Computational conditions

To investigate the influence of the oscillating air flow on fuel jet atomization and droplets evaporation process, the multimode is selected as an object because it holds the two different breakup behaviors, i.e., bag breakup and shear breakup, which makes it possible to judge the response to the oscillating condition. Both breakup modes are the results of wave disturbance development due to the aerodynamic force. For a lower aerodynamic Weber number, surface waves generated at the windward of the liquid jet grow into larger waves where nodes could be observed. Due to the higher pressure of stagnating gas flow on the upstream side of the liquid jet, the connecting liquid jet between these nodes would form a baglike structure and finally breakup into relatively large droplets. Whereas, for a higher aerodynamic Weber number, the ligaments would be generated along the periphery of the liquid jet due to the shear stress and droplets are finally generated at the end of ligaments. The former one is called bag breakup and the latter

one is shear breakup. In addition, the liquid-gas momentum flux ratio should not be small, otherwise the difference of the liquid jet trajectory resulted from the oscillating velocity of the inflow air could hardly be observed. Therefore, two scenarios under the steady and oscillating air velocity, respectively, are simulated, considering the same averaged velocity of 24.8 m/s for air inflow. Kerosene is widely used in aircraft engines and is used in this work as the liquid fuel. The liquid jet velocity is prescribed by a parabolic profile with mean value of 12.4 m/s. The oscillation frequency is set to be 500 Hz which is decided by the combustion instability observed in the aircraft engines at the elevated pressure [4]. The amplitude of fluctuating crossflow velocity is 20% of the average velocity according to the experimental indication [9], and the oscillating velocity profile is made to fit with a sine curve. Since the aerodynamic Weber number is proportional to the square of air velocity and determines the trajectory of the liquid jet, the higher the fluctuation amplitude is, the longer the liquid jet penetrates in the space which would lead to an enlarged computational domain. Meanwhile, regarding the purpose of this chapter, the atomization process should be kept existing in the multimode breakup regime during the whole calculation so that the bag breakup, shear breakup and the transition of which could all be observed. Therefore, the aerodynamic Weber number of multimode regime needs to be within the range from 30 to 110 by referring to the Sallam's work [24]. Thus, the amplitude of 20% is determined in this study which would give a minimum value of 29.44 to keep the aerodynamic Weber number always approximately larger than 30. The hot air and cold liquid jet with the temperature of 500 K and 300 K, respectively, are employed for the study of the evaporation process. The pressure is set to be 3.0 MPa for the real engine situation and gas flow is considered as ideal gas. For the present condition, the air viscosity is 2.72×10^{-5} Pa·s, liquid viscosity is 2.87×10^{-3} Pa·s, and liquid-gas surface tension is 0.03 N/m. Thus, the aerodynamic Weber number, $We = \rho_g u_g D_{inj}/\sigma$, in this configuration is evaluated as 46, and liquid-gas momentum flux ratio, M, is 10 for the steady crossflow condition, which is classified to be in the multimode breakup regime. The parameters for the oscillating crossflow are shown in Table 1. Fig. 3.1(b) illustrates the profiles of air velocity from

the left boundary for the steady and oscillating inflow conditions.

A secondary breakup model known as Taylor analogy breakup (TAB) model was once applied in the present study, however very little secondary breakup took place (less than 1%) in the computational domain. For the steady crossflow condition, generally the aerodynamic Weber number of the atomized droplets is rarely larger than 9.2. However, the TAB model requires the aerodynamic Weber number of a single droplet larger than 12 for enough time.

The computational cost of the steady case, performed at the K-Computer (Fujitsu SPARC64TM VIIIfx processor, 300cores), is 184 k hours (real time 80h), and the corresponding time for the oscillating case, simulated at the Kyoto University Supercomputer (Cray XC40, 1200 cores), is 1.4 million hours (real time 1170h).

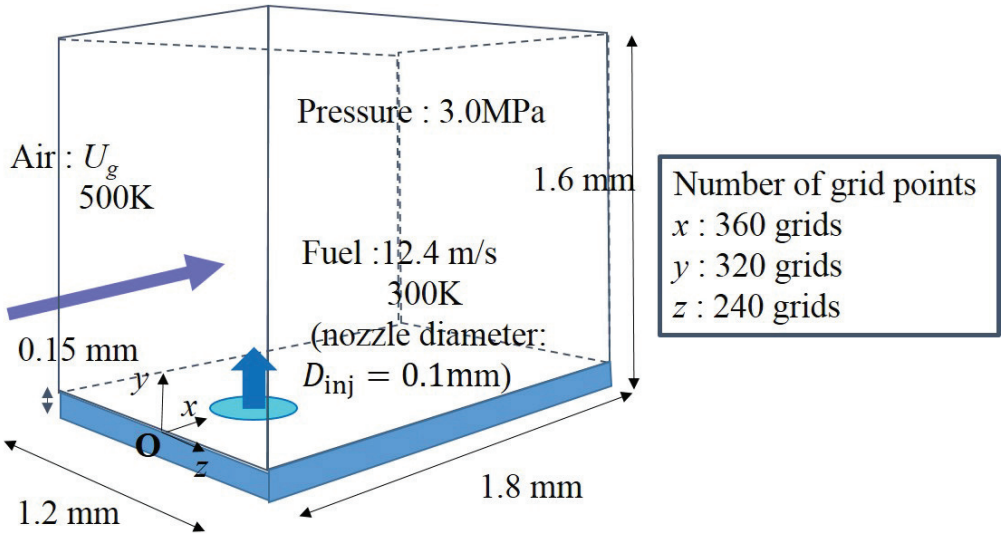

(a)

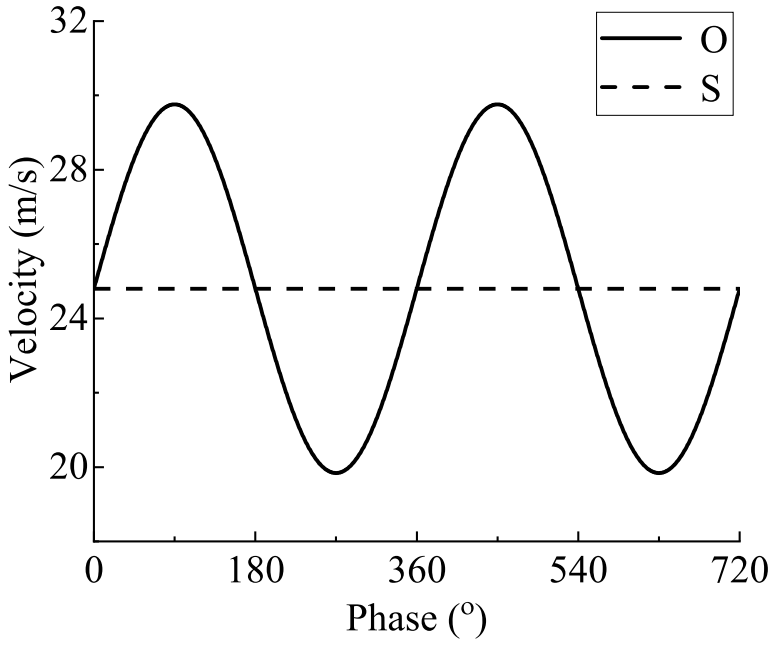

(b)

Figure 3.1: Computational setups: (a) schematics of computational domain and conditions, (b) crossflow velocity profile from left boundary (O: oscillating crossflow and S: steady crossflow).

Table 3.1: Parameters for detailed numerical simulation in oscillating crossflow.

Physical properties	
Liquid fuel	Kerosene
Crossflow gas	Air
Liquid nozzle diameter, D_{inj} (mm)	0.1
Liquid jet velocity, u_l (m/s)	12.4
Liquid jet viscosity, μ_l (Pa·s)	2.87×10^{-3}
Liquid jet density, ρ_l (kg/m^3)	848
Liquid jet temperature, T_l (K)	300
Crossflow velocity, u_g (m/s)	19.84-29.76
Crossflow viscosity, μ_g (Pa·s)	2.72×10^{-5}
Crossflow temperature, T_g (K)	500
Liquid-gas surface tension, σ (N/m)	0.03
Ambient pressure, P (MPa)	3.0
Aerodynamic Weber number, We (-)	29.44-66.24
Jet Ohnesorge number, Oh (-)	0.06
Liquid-gas momentum flux ratio, M (-)	7.42-15.93

3.4 Results and discussion

3.4.1 Breakup behavior and liquid jet trajectory

Figure 3.2 shows the front views of instantaneous iso-surface of the levelset function of φ=0, which is regarded as the liquid-gas interface. The comparison is given for the steady case and different phases of 90°, 180°, 270° of the oscillating case. Four black circles in the figure denote the positions of mode transition which are called as transition points in this study. Shear breakup occurs at the upstream of the transition point as indicated by the red circle in the steady case, and the bag breakup occurs at the downstream of the transition point as suggested by the blue circle in the steady case. The steady case reproduces the breakup behavior in the multimode regime where the transition from bag mode regime to shear mode regime occurs [24]. Thus, this regime usually contains two breakup behaviors of bag breakup and shear breakup. The bag breakup occurs when the liquid jet reaches the downstream domain, and the surface wave is enhanced by both Rayleigh-Taylor instability and Kelvin-Helmholtz instability. Once the surface wave is too large to be self-sustained, the jet would breakup into child droplets. Conversely, the shear breakup exists near the nozzle exit, where the shear force strips off threads from the liquid jet, and the threads would further breakup into smaller droplets. For the oscillating case, the liquid jet penetration varies at different phases, and it is weakened at the phase of higher crossflow velocity, i.e., 90°. This result agrees well with the trajectory property that is positively correlated to the liquid-gas momentum flux ratio. In addition, the breakup behavior also shows a similar trend as the aerodynamic Weber number changes, i.e., the larger the aerodynamic Weber number is, the closer it approaches a shear mode regime for the fact that more threads tend to be stripped off from the liquid jet. As the crossflow velocity decreases from phase 90° to 270°, the aerodynamic Weber number becomes smaller which would weaken the shear breakup and enhance the bag breakup. Therefore, the transition point would be transited to upstream region to indicate less proportion of shear breakup in the whole atomization process.

Figure 3.3 shows the comparison of the time-averaged liquid jet trajectories on the central $x-y$ plane ($z = 0.0$ mm), and it includes: (a) steady case in comparison with the jet trajectories calculated by the analytical solution [25] and empirical correlation [26], (b) the comparison of steady case and oscillating case at different phases, colored regions represent liquid jets with VOF function of, $\psi \geqslant 0.5$. Especially, the time-averaged value in the oscillating condition is for a short period (0.04 ms) which corresponds to the cycle of 7.2°. In Wu's work [25], the liquid jet trajectory was analyzed without considering the mass and momentum loss during the atomization process such that the computed jet trajectory in this work is lower than Wu's solution. In Song's work [26], the experiment was conducted at the elevated pressure of 9.65 bar, which is still lower than the present work of 30 bar and pressure is also found as another factor to affect the jet trajectory. Therefore, due to the difference of pressure and density ratio, the discrepancy between the steady crossflow case and previous works is observed especially at the downstream position, although a well match is obtained near the nozzle exit. Shown in Fig. 3.3(b), the liquid jet trajectory presents a quick response to the change of crossflow velocity, and in general, the jet penetration decreases with the increase of crossflow velocity. This can be attributed to the monotonic increment of the penetration force displayed from phase 90° to 270°. It is consistent with the monotonic decline of crossflow velocity shown in Fig. 3.1(b). It is also worth noticing that the phase 180° (green color) displays a similar liquid trajectory with steady case (red color), which suggests that there is little time delay between the inflow velocity change and the jet response. The distinctive liquid jet trajectories, breakup behaviors, as well as frequency dependence shown in Fig. 3.3 were also observed in Sharma's experiments in the multimode breakup regime [27]. Figure 3.3(b) also shows that the averaged jet area at phases with higher air velocity (such as 90°) is smaller and shorter than that of lower velocity phases, for example 270°, indicating an increased mass loss within larger aerodynamic Weber number.

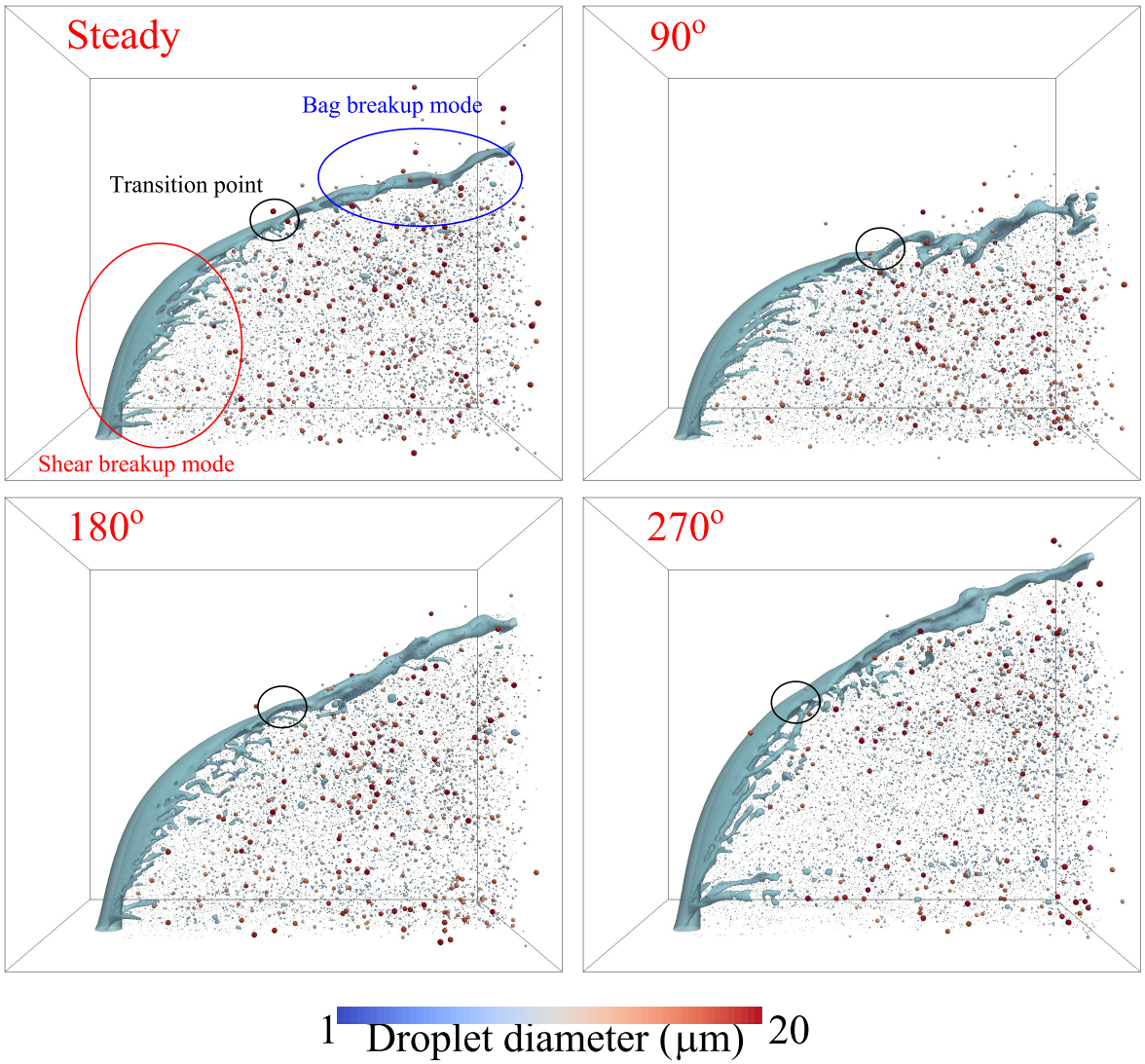

Figure 3.2: Front view snapshots of instantaneous iso-surface of levelset function of $\varphi = 0$ of steady case and different phases of 90°, 180°, 270° of oscillating case. Particle color indicates droplet diameter; black, red, and blue circles indicate transition points, shear breakup, and bag breakup, respectively.

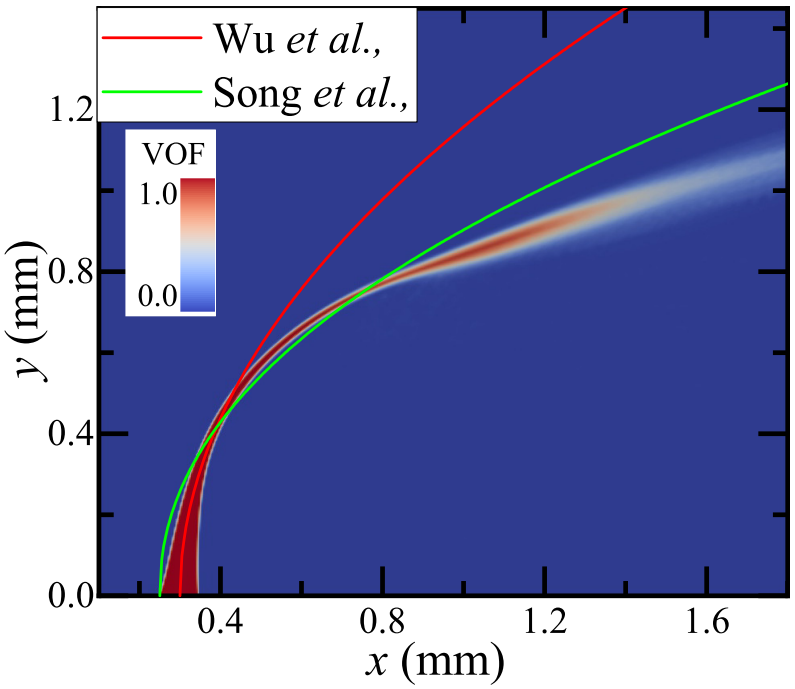

(a)

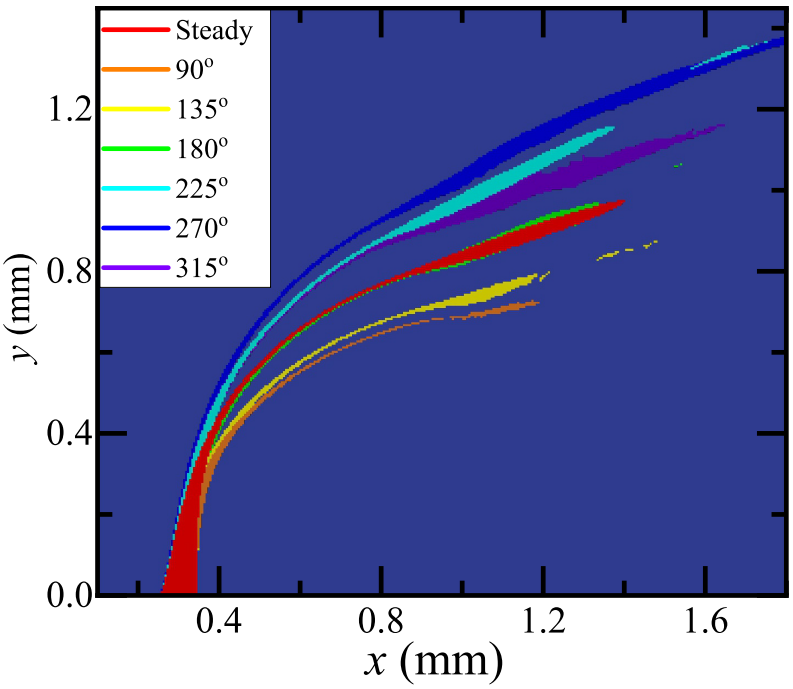

(b)

Figure 3.3: Time-averaged liquid jet trajectories on the central $x-y$ plane ($z = 0.0$ mm): (a) steady case, (b) the comparison of steady case and oscillating case with different phases, colored regions represent liquid jets with VOF function of, $\psi \geqslant 0.5$.

3.4.2 Flow field behind the jet

Figure 3.4 shows the comparisons of the time-averaged distributions of the vorticity z component ($\omega_z = \partial v/\partial x - \partial u/\partial y$) and streamline on the central $x-y$ plane ($z = 0.0$ mm) for the steady and different phases in 90°, 180°, 270° of the oscillating case. A transition point is defined by the velocity field below the liquid jet where the local velocity vector is directing perpendicularly to the liquid-gas interface. This transition point separates the flow field behind the liquid jet into two different parts. The left-side circle indicates a counter clockwise circulation flow that locates just after the liquid jet, and the right-side circle points out the region where flow moves to the downstream directly. In addition, for the oscillating case, the transition point tends to be transmitted to the upstream of the jet as air inflow velocity decreasing from 90° to 270°. Therefore, the left-side circle which represents the domain of shear breakup would become less significant when the aerodynamic Weber number is weakened during the phase change from 90° to 270°. And the shape of this region would change from a fat circle to a slim oval shape beneath the liquid jet. Furthermore, due to the oscillating crossflow velocity, the vorticity ω_z shows higher value and more turbulent changes in different phases than those of the steady case, which suggests the existence of more complex and stronger vortex behind the liquid jet for the oscillating case.

Figure 3.5 gives the time-averaged distribution of vorticity y component ($\omega_y = \partial u/\partial z - \partial w/\partial x$) on the $x - z$ plane at different heights of $y = 0.0$, 0.3, and 0.6 mm for the steady case in a three-dimensional view. A counter-rotating vortex pair (CVP) is observed at all three $x - z$ planes as indicated by the red and blue circle pair. Therefore, combining the CVP and the circulation flow denoted by the colored streamline, a three-dimensional vortex morphology is depicted by the green arrows. The transition point, where the vortex impact on the liquid jet perpendicularly, separates the flow field into two parts. The horizontally rotating CVP together with vertically rotating counter-clockwise flow comprise a unique three-dimensional vortex, which is referred to as shear breakup vortex (SBV) in this chapter. The SBV was found to enhance the threads generation clearly when the aerodynamic Weber number increases obviously (46-200)

in the previous chapter from bag mode regime to shear mode regime. Still, even the change of aerodynamic Weber number in this study (29.44-66.24) is not that obvious, the influence of which could be observed. The SBV behind the liquid jet deflects the jet momentum to the spanwise direction and enhances the threads generation in relation to the shear breakup. As a result, the threads in the multimode regime are observed to be mainly generated below the transition points (see Figs. 3.2 and 3.4). The SBV in the oscillating case is presumed to be determined by the crossflow velocity since its vertically rotating component is decided by the velocity as indicated by the red circles area in Fig. 3.4.

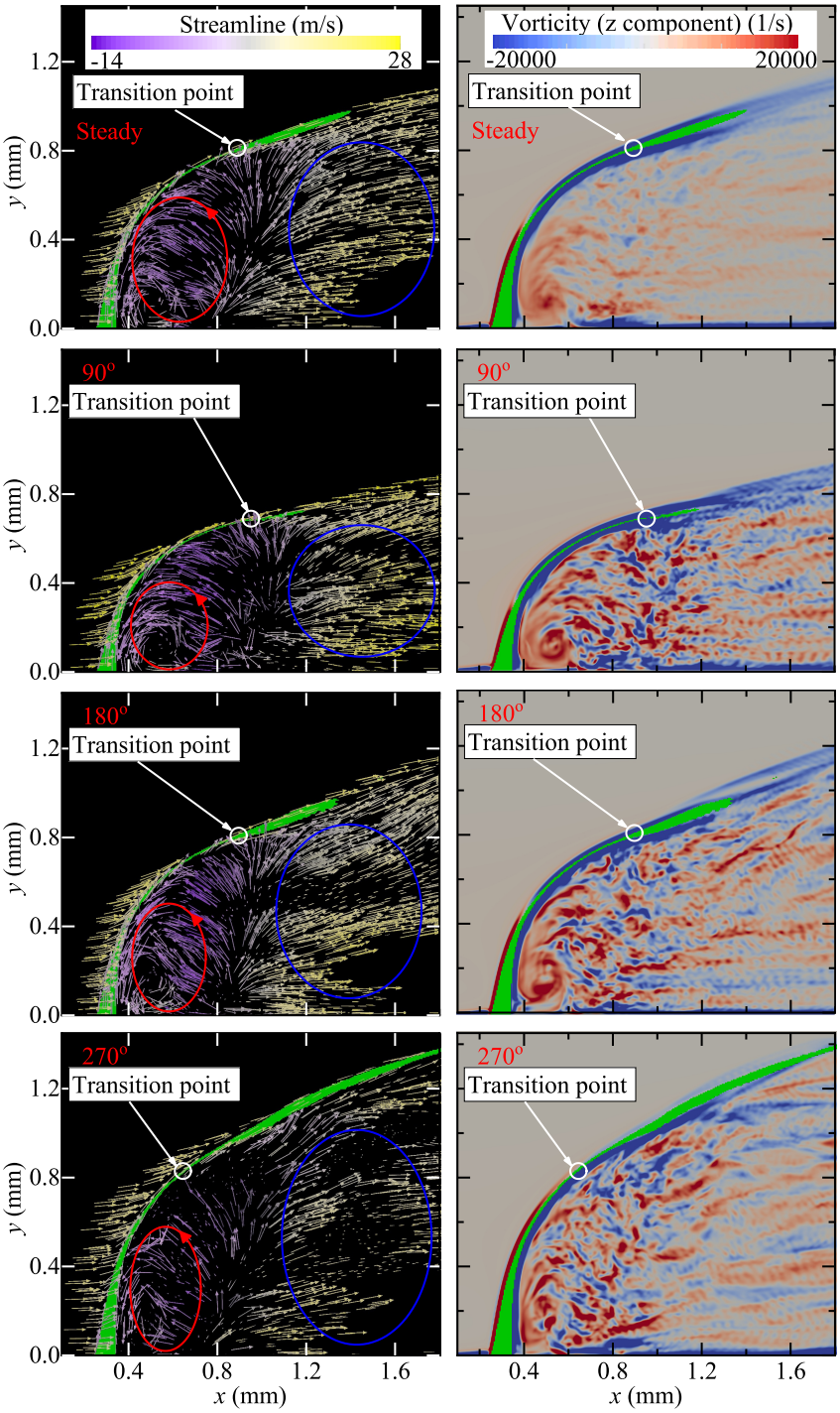

Figure 3.4: Time-averaged distributions of streamline and vorticity z component on the central $x-y$ plane ($z = 0.0$ mm) of steady case and different phases of 90°, 180°, 270° of oscillating case. Green area indicates liquid jet.

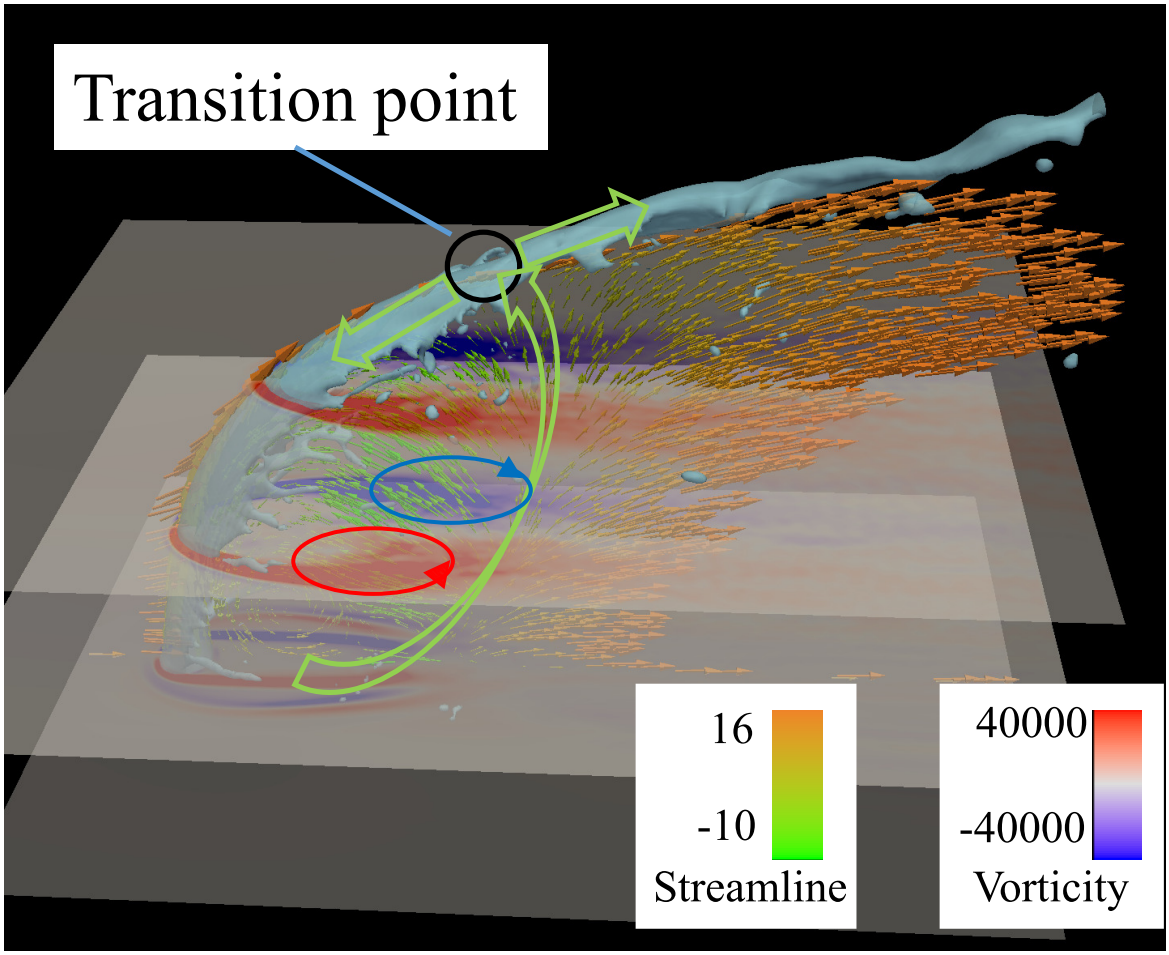

Figure 3.5: Time-averaged distribution of vorticity y component on the $x-z$ plane at different heights of $y = 0.0$, 0.3, 0.6 mm of steady case.

3.4.3 Spray evaporation

Figure 3.6 depicts the contour plots of the time averaged droplet number density, evaporation rate and fuel vapor mass fraction on the central $x-y$ plane ($z = 0.0$ mm) of different phases in 90°, 180°, 270° of the oscillating case, where green area indicates liquid jet. The regions where more droplets are accumulated show constant changes, that is, two parts, one near the bottom wall, another beneath the liquid jet around the transition point, are observed under the higher We condition; and these two parts become one beneath the liquid jet under the lower We condition. These characteristics under higher and lower We conditions fit the results in shear mode regime and bag mode regime which are investigated in the previous chapter The evaporation rate in all phases shows relatively lower values in the SBV region even though it accumulates more droplets. This discrepancy could be explained by referring to the plots of fuel vapor; the vaporized fuel tends to be trapped by the SBV which shows similar shape of the SBV, resulting in a low temperature domain. Since the droplet evaporation rate is dominated by the local temperature and mass transfer number, it implies that the SBV could play an important role in suppressing the evaporation process. As to the region out of the boundary of SBV, especially in the area near the wall, the temperature slightly increases and droplets accumulate as a result of the transport effect of SBV by its counter-clockwise movement. Thus, the evaporation near the wall displays a higher value than the other regions in all phases.

Figure 3.7 shows the fluctuation of generated droplets SMD (D_{32}), arithmetic diameter (D_{10}), and their ratio in the downstream region (1.5 mm $\leqslant x \leqslant$ 1.8 mm) for different phases in the whole two cycles of the oscillating case as well as the ones of the steady case. In Song's experimental work, D_{32}/D_{10} was used as an index to show the shape of droplet size PDF distribution. For example, for a given D_{10}, a large value of D_{32}/D_{10} means that droplet size distribution skews more towards relatively larger droplets range. Therefore, this index is used for comparison. All the three variables show periodic changes with the same frequency as crossflow velocity (see Fig. 3.1(b)). Specially, D_{32} and D_{32}/D_{10} show similar sine curves as the crossflow velocity, in contrast

to which, the D_{10} profile shows a cosine curve. Generally, the D_{32} is largely affected by the aerodynamic Weber number (We); it grows with increasing the We because the shear breakup is enlarged and the droplet size distribution obtained at the further downstream shifts to the smaller size region [26]. However, this is not the case in present study, focusing on the spray dense region near the nozzle exit, and the D_{32} appears to be larger at high velocity phase 90°. This can be related to the intense SBV with larger extended area along the axial direction (x) at 90°, leading to the enhanced recirculation of discrete droplets and therefore their evaporation. In this situation, the small droplets are easily consumed before moving downstream and large D_{32} is then found out of this SBV region (see blue circle in Fig. 3.4). Hence, by referring to the slim SBV region in phase 270° (see Fig. 3.4), D_{32} become smaller for phase 270° since more small droplets survives at the region far from the fuel nozzle. It is also interesting to note that, due to the violent vorticity change in the oscillating case compared to the steady flow, the mean value of D_{32} appears to be smaller than the steady case. The same trend is found for D_{10} as well, indicating an improved liquid atomization by the oscillating crossflow. In addition, the mean value of D_{32}/D_{10} in oscillating flow has almost the same value as the one of steady case, which implies that little difference on droplet size PDF is observed for different cases.

The influence of SBV structure on liquid evaporation can further be outlined by the plots of fuel vapor distribution evaluated in the same downstream region (1.5 mm $\leqslant x \leqslant$ 1.8 mm) shown in Fig. 3.8. The value of the steady case is set to be unit for normalization. The fuel vapor value in the oscillating case shows a periodic cosine-like curve. A small value of fuel vapor is found at phase 90° compared to the peak value at phase 270°. Although phase 90° commits to a higher evaporation rate as discussed above, the intense SBV area in 90° traps the vaporized fuel beneath the liquid jet and thus, a few of them are found at downstream domain. Based on the present results, the atomization process under the influence of the fluctuating carrier air velocity tends to generate more small droplets which is shown in Figure 3.7 with larger D_{32} in the fluctuating case compared to the steady case. If the combustion is involved at the

downstream locations, this increased D_{32} would enhance the evaporation and fuel-air mixing, therefore the subsequent combustion and heat release rate, because of which the combustion instability under the constant temperature would be amplified.

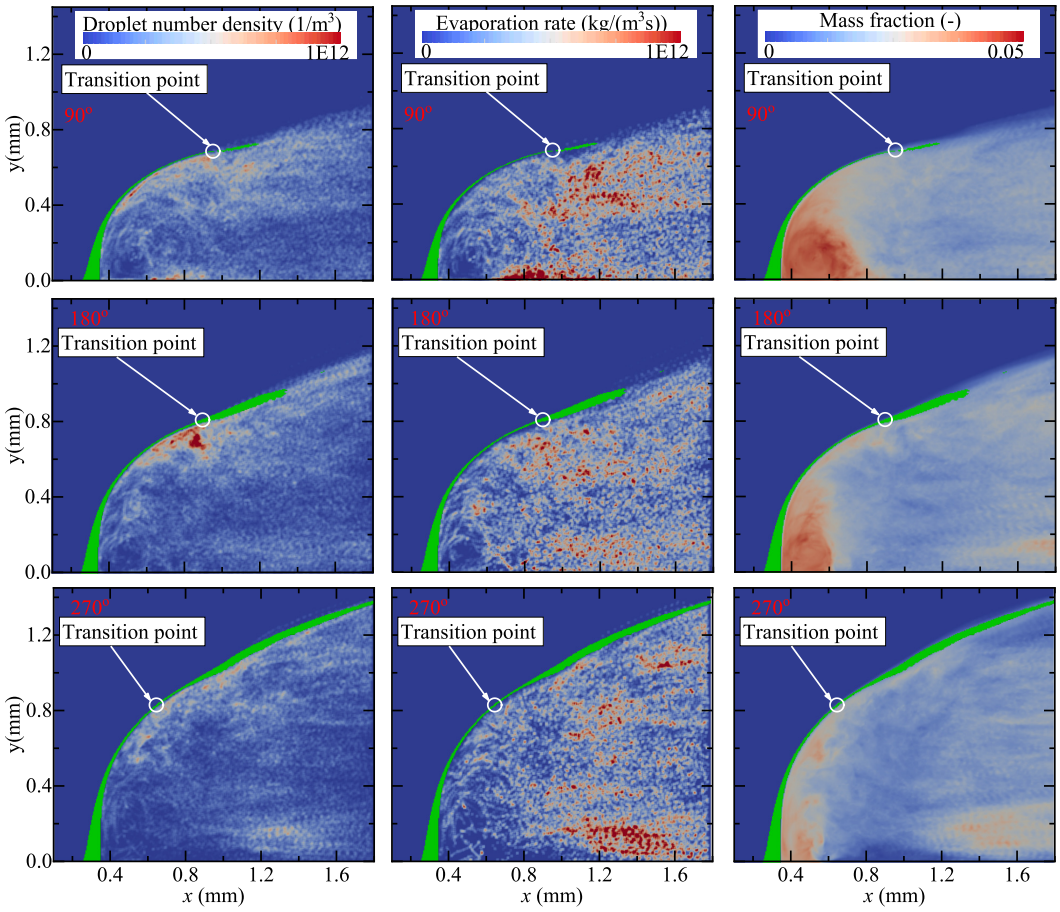

Figure 3.6: Various evaporation properties: droplet number density, evaporation rate, fuel vapor mass fraction, of different phases of 90°, 180°, 270° of oscillating case on the central $x - y$ plane ($z = 0.0$ mm). Green area indicates liquid jet.

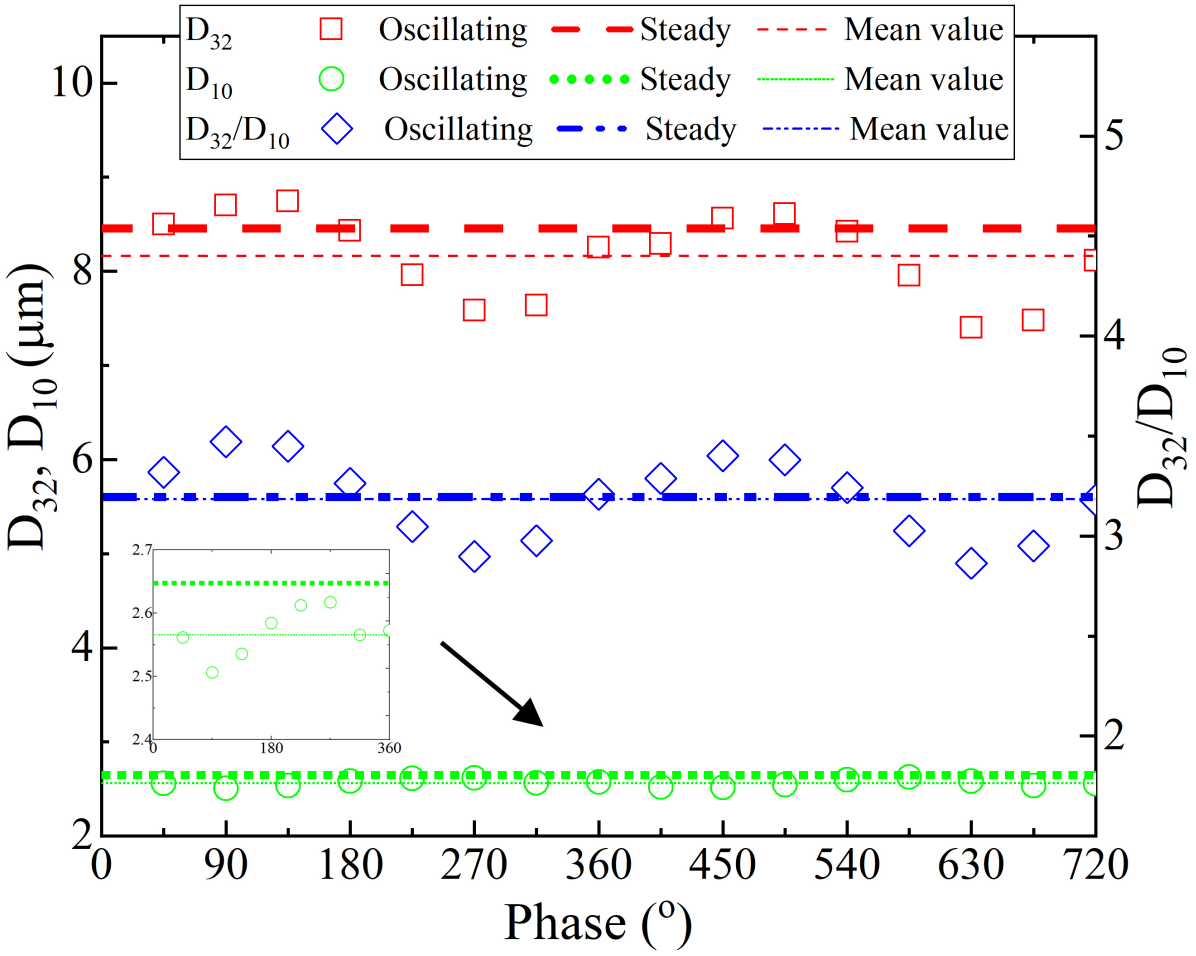

Figure 3.7: Fluctuation of droplet sizes (D_{32} and D_{10}) and their ratio (D_{32}/D_{10}) in the downstream region (1.5 mm $\leqslant x \leqslant$ 1.8 mm) of steady and oscillating cases.

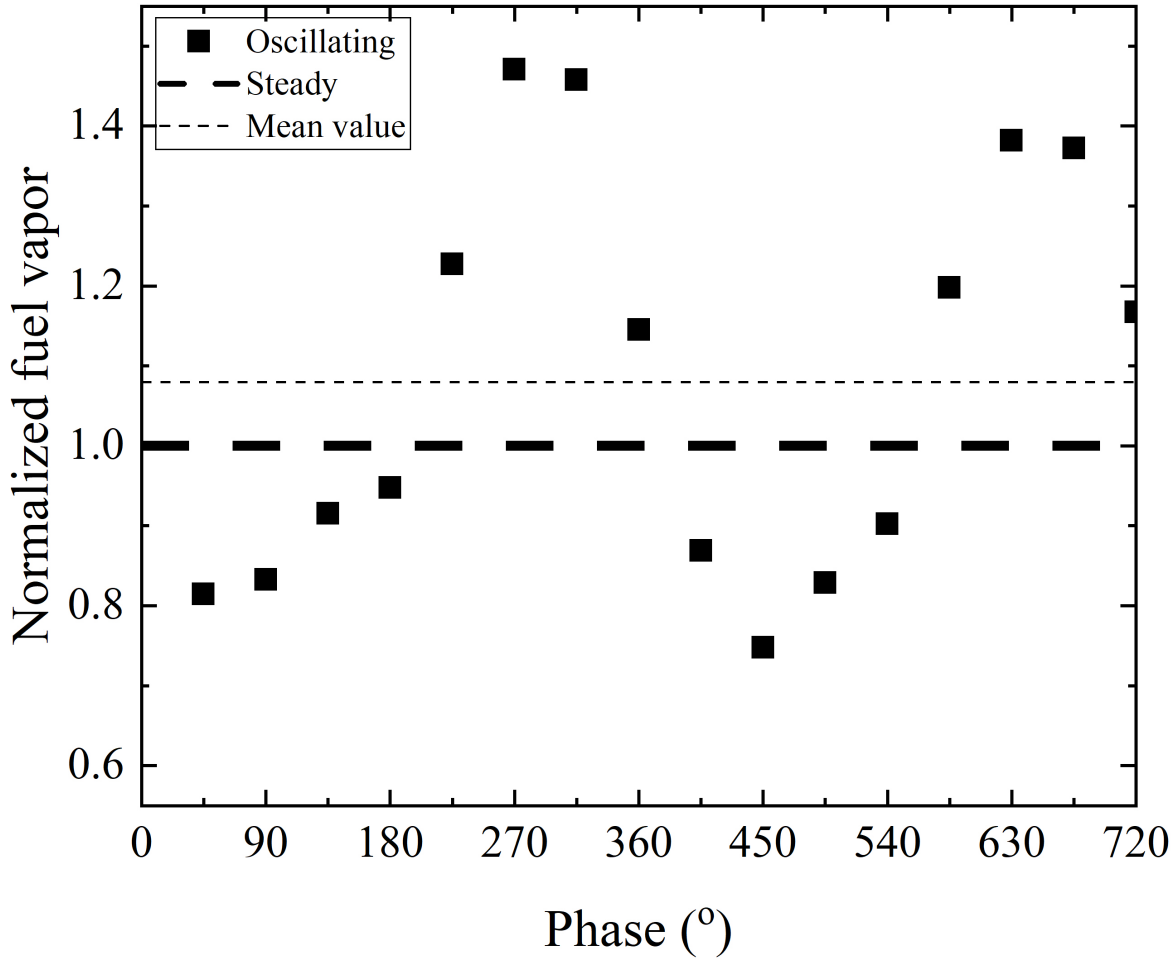

Figure 3.8: Fluctuation of normalized fuel vapor in the downstream region (1.5 mm $\leqslant x \leqslant$ 1.8 mm) of steady and oscillating cases.

3.5 Conclusions

In this chapter, the atomization-evaporation process of a liquid fuel jet in the oscillating crossflow under the elevated ambient pressure was investigated in comparison to that in a steady crossflow by using a detailed numerical simulation with the E-L framework, in which the CLSVOF method and the non-equilibrium Langmuir-Knudsen evaporation model are employed to capture the atomization behavior and droplet evaporation characteristics, respectively. The main results are summarized as follows.

1. The breakup behavior, liquid jet trajectory, droplet size and fuel vapor distributions in the downstream region are observed to hold the same frequency as the oscillating crossflow velocity. The former three properties also respond to the velocity rapidly, in contrast to which, the fuel vapor distribution tends to have a half period time delay. The fast response of the breakup behavior and liquid jet trajectory are in good agreement with the experimental results in multimode regime [27].

2. The droplet size distributions, D_{32} and D_{10}, shows converse changes, which are presumed to be caused by the shear breakup vortex (SBV) behind the liquid jet. The SBV is enhanced at the higher velocity phase of 90°, thus holding more droplets circulating there and resulting in higher evaporation rate. Therefore, the small droplets are consumed in advance leading to larger D_{32} and smaller D_{10} in the downstream region.

3. Fuel vapor in the downstream region is observed to have a half period time delay to the oscillating crossflow velocity since the weakened SBV at the lower velocity phase could sent more fuel vapor, which is trapped by the enhanced SBV at the higher velocity phase, out of the domain. The smaller mean value of D_{32} and D_{10} as well as the larger mean value of fuel vapor in the downstream region in the oscillating crossflow compared to those in the steady crossflow suggest a better atomization-evaporation property for the more violent turbulence vorticity change in the SBV region.

Therefore, the investigation of this chapter may help to improve the understanding of the physical mechanism how combustion instability in combustors influences the combustion properties such as combustion efficiency and ignition. However, for the future investigation, consideration of combustion reaction, which may drastically change the temperature field and then combustion instability behavior, is essential.

References

[1] R. Balachandran, B. Ayoola, C. Kaminski, A. Dowling, and E. Mastorakos. Experimental investigation of the nonlinear response of turbulent premixed flames to imposed inlet velocity oscillations. *Combust. Flame*, 143:37–55, 2005.

[2] H. Altay, R. Speth, D. Hudgins, and A. Ghoniem. Flame-vortex interaction driven combustion dynamics in a backward-facing step combustor. *Combust. Flame*, 156:1111–1125, 2009.

[3] S.Hong, S. Shanbhogue, R. Speth, and A. Ghoniem. On the phase between pressure and heat release fluctuations for propane/hydrogen flames and its role in mode transitions. *Combust. Flame*, 160:2827–2842, 2013.

[4] S. Tachibana, K. Saito, T. Yamamoto, M. Makida, T. Kitano, and R. Kurose. Experimental and numerical investigation of thermos-acoustic instability in a liquid-fuel aero-engine combustor at elevated pressure: validity of large-eddy simulation of spray combustion. *Combust. Flame*, 162:2621–2637, 2015.

[5] T. Kitano, K. Kaneko, R. Kurose, and S. Komori. Large-eddy simulations of gas- and liquid-fueled combustion instabilities in back-step flows. *Combust. Flame*, 170:63–78, 2016.

[6] A. Pillai, J. Nagao, R. Awane, and R. Kurose. Influences of liquid fuel atomization and flow rate fluctuations on spray combustion instabilities in a backward-facing step combustor. *Combust. Flame*, 220:337–356, 2020.

[7] K. Bunce, J. Lee, and D. Santavicca. Characterization of liquid jets-in-crossflow under high temperature, high velocity non-oscillating and oscillating flow conditions. *44th AIAA ASME*, AIAA2006–1225, 2006.

[8] J. Song, C. Ramasubramanian, and J. Lee. Response of liquid jet to modulated crossflow. *Atomiz. Sprays*, 24:129–154, 2014.

[9] J. Song and J. Lee. Characterization of spray formed by liquid jet injected into oscillating air crossflow. *Proc. ASME Turb. Expo. 2015*, GT 2015–43726, 2015.

[10] Y. Hu and R. Kurose. Nonpremixed and premixed flamelets les of partially premixed spray flames using a two-phase transport equation of progress variable. *Combust. Flame*, 188:227–242, 2018.

[11] A. Pillai and R. Kurose. Combustion noise analysis of a turbulent spray flame using a hybrid dns/ape-rf approach. *Combust. Flame*, 200:168–191, 2019.

[12] J. Wen, Y. Hu, A. Nakanishi, and R. Kurose. Atomization and evaporation process of liquid fuel jets in crossflows: A numerical study using eulerian/lagrangian method. *Int. J. Multiphas. Flow*, 103331, 2020.

[13] M. Herrmann. A parallel eulerian interface tracking/lagrangian point particle multiscale coupling procedure. *J. Comput. Phys.*, 229:745–759, 2010.

[14] A. Albadawi, D. Donoghue, A. Robinson, D. Murray, and Y. Delauré. Influence of surface tension implementation in volume of fluid and coupled volume of fluid with level set methods for bubble growth and detachment. *Int. J. Multiphas. Flow*, 53:11–28, 2013.

[15] K. Yokoi. A practical numerical framework for free surface flows based on clsvof method, multi-moment methods and density-scaled csf model: numerical simulations of droplet splashing. *J. Comput. Phys.*, 232:252–271, 2013.

[16] J. Brackbill, D. Kothe, and C. Zemach. A continuum method for modeling surface tension. *J. Comput. Phys.*, 100:335–354, 1992.

[17] D. Zuzio, J. Estivalèzes, and B. DiPierro. An improved multiscale eulerian-lagrangian method for simulation of atomization process. *Comput. Fluids*, 176:285–301, 2018.

[18] R. Miller, K. Harstad, and J. Bellan. Evaluation of equilibrium and non-equilibrium evaporation models for many-droplet gas-liquid flow simulations. *Int. J. Multiphas. Flow*, 24:1025–1055, 1998.

[19] R. Miller and J. Bellan. Direct numerical simulation of a confined three-dimensional gas mixing layer with one evaporating hydrocarbon-droplet-laden stream. *J. Fluid Mech.*, 384:293–339, 1999.

[20] T. Kitano, J. Nishio, R. Kurose, and S. Komori. Evaporation and combustion of multicomponent fuel droplets. *Fuel*, 136:219–225, 2014.

[21] T. Kitano, J. Nishio, R. Kurose, and S. Komori. Effects of ambient pressure, gas temperature and combustion reaction on droplet evaporation. *Combust. Flame*, 161:551–564, 2014.

[22] R. Kurose, H. Makino, S. Komori, M. Nakamura, F. Akamatsu, and M. Katsuki. Effects of outflow from the surface of a sphere on drag, shear lift, and scalar diffusion. *Phys. Fluids*, 15:2338–2351, 2003.

[23] H. Watanabe, R. Kurose, S. Huang, and F. Akamatsu. Characteristics of flamelets in spray flames formed in a laminar counterflow. *Combust. Flame*, 148:234–248, 2007.

[24] K. Sallam, C. Aalburg, and G. Faeth. Breakup of round nonturbulent liquid jets in gaseous crossflow. *AIAA J.*, 42:2529–2540, 2004.

[25] P. Wu, K. Kirkendall, R. Fuller, and A. Nejad. Breakup processes of liquid jets in subsonic crossflows. *J. Propuls. Power*, 13:64–73, 1997.

[26] J. Song, C. Cain, and J. Lee. Liquid jets in subsonic air crossflow at elevated pressure. *J. Eng. Gas Turb. Power Trans Asme*, 041502, 2015.

[27] A. Sharma, J. Song, and J. Lee. Response of spray formed by liquid jet injected into oscillating air crossflow. *ILASS2015*, 2015.

Nomenclature

c_p	: Specific heat capacity [J/(K kg)]	λ	: Thermal conductivity [W/(m K)]
D	: Diffusion coefficient [m^2/s]	μ	: Viscosity [Pa s]
D_{inj}	: Nozzle injector diameter [m]	ρ	: Density [kg/m^3]
f_1	: Correction of Stokes drag [-]	σ	: Surface tension [N/m]
f_2	: Correction of heat transfer [-]	$\boldsymbol{\tau}$	: Stress tensor [N/m^2]
$F_{\boldsymbol{\sigma}}$	: Body force of surface tension [N]	φ	: Levelset function [-]
h	: Enthalpy [J/kg]	ψ	: VOF function [-]
L_V	: Latent heat [J/kg]	ω	: Vorticity [1/s]
m	: Mass [kg]	**Subscripts**	
M	: Liquid-gas momentum flux ratio [-]	d	: Droplet's value
n	: Droplet number density [-]	F	: Fuel
Nu	: Nusselt number [-]	g	: Gas phase value
Oh	: Ohnesorge number [-]	k	: Chemical species k
P	: Pressure [Pa]	l	: Liquid phase value
Pr	: Prandtl number [-]		
S	: Source term		
t	: Time [s]		
T	: Temperature [K]		
$\boldsymbol{u}$	: Velocity [m/s]		
We	: Aerodynamic Weber number [-]		
Y	: Mass fraction [-]		

Chapter 4

Large-eddy simulation (LES) of turbulent dense spray flame coupled with VOF simulation of liquid fuel atomization

4.1 Introduction

In the previous chapters, the spray atomization-evaporation process in spray combustion is investigated numerically in detail. The atomization behaviors of liquid jets in steady and oscillating crossflows are reproduced in comparison to the experimental studies. Within a comprehensive understanding of the approaches to reproduce the spray atomization, it makes it possible to couple the combustion process with the beforehand atomization process to investigate the spray combustion. In this chapter, a numerical framework to model dense spray flames is proposed by coupling the combustion process using a LES flamelet approach with the atomization process using a VOF method.

Various techniques and studies have been experimentally and numerically conducted to investigate the atomization and combustion processes in spray combustion in separated ways, which make it difficult to clarify the detailed mechanism of spray combus-

tion. Recently, Shinjo et al. [1] pointed out that the conventional researches in academic and industrial simulations, in which the spray properties for combustion simulations are given by some models instead of physical accuracy, should be shifted to an ideal situation, where the spray atomization is well resolved and hence considered in the combustion simulation since the enhanced computational ability in these years make it possible to consider this issue. Masri's group [2–4] has developed the Sydney Burner to provide various spray properties, ranging from dilute spray to dense spray, in which the atomization and combustion regions are physically well separated, ensuring an ideal situation to develop numerical approaches to investigate the dense spray flames with considering the detailed atomization mechanism.

The purpose of this chapter is, therefore, to propose a numerical framework to model the coupling of atomization and combustion of dense spray flames while maintaining reasonable computational cost. Results are compared with experimental data obtained from the Sydney needle burner [3, 4]. The concept is as follows. The liquid fuel atomization is solved by a detailed numerical simulation, in which both continuum gas and liquid phases are strictly solved in an Eulerian framework, and the Eulerian components of the liquid droplets are transformed into the Lagrangian droplets at a certain downstream cross-section, i.e., sampling cross-section, whose information is stored in database. Then, the combustion process is solved by a large eddy simulation (LES) with a flamelet model adopting the pre-stored database of Lagrangian droplets, namely, by a one-way coupling between a VOF simulation and a combustion simulation.

4.2 Numerical simulation methods

In this work, all computations are performed using an unstructured LES solver, i.e., the FrontFlow/Red extended by Kyoto University [5–7].

4.2.1 Governing equations for dense spray region

In the dense spray region where the atomization process occurs, liquid and gas continuum phases are treated as incompressible fluids and are both solved in an Eulerian framework. Their governing equations solved in this region include the conservation equations of mass and momentum as follows,

$$\rho \nabla \cdot \boldsymbol{u} = 0, \tag{4.1}$$

$$\rho(\frac{\partial \boldsymbol{u}}{\partial t} + \boldsymbol{u} \cdot \nabla \boldsymbol{u}) = -\nabla P + \nabla \cdot (2\mu \boldsymbol{S}) + \boldsymbol{F}_\sigma + \boldsymbol{g}, \tag{4.2}$$

Here, ρ is the local density, $\boldsymbol{u}$ the velocity vector, P the pressure, μ the viscosity, $\boldsymbol{g}$ the gravity, $\boldsymbol{S}$ the rate-of-strain tensor $S_{ij} \equiv (\partial_i u_j + \partial_j u_i)/2$, and $\boldsymbol{F}_\sigma$ is the source term of surface tension calculated by the continuum surface force (CSF) model [8].

The high-resolution interface capturing (HRIC) scheme [9] is implemented into the volume of fluid (VOF) method in order to capture the gas-liquid interface and the atomization process, where the VOF advection function takes the following form [10],

$$\frac{\partial \psi}{\partial t} + \boldsymbol{u} \cdot \nabla \psi + \boldsymbol{u}_m \cdot \nabla[\psi(1-\psi)] = 0, \tag{4.3}$$

where, ψ is the VOF value within each grid, and $\boldsymbol{u}_m = \boldsymbol{u}_l - \boldsymbol{u}_g$ is the compressive velocity. The subscripts l and g refer to liquid and gas phases, respectively. The compressive velocity is considered only for the gas-liquid interface in the normal direction to avoid a dispersion of the VOF value. This additional compressive term helps retain the mass conservation and convergence for the VOF advection. It also facilitates the simulation of a multiphase flow with a large liquid/gas density ratio. Because the present study is performed in cylindrical coordinates with unstructured grids, the HRIC scheme is implemented instead of the coupled level-set and VOF method, which avoids the unnecessary complexity induced by the use of the level-set method.

A tagging method [11, 12] is then utilized to transform the Eulerian liquid parts at a specific downstream cross-section into the Lagrangian spherical droplets with the droplet properties such as the position, size, and velocity, which are saved in a database (referred to as E-L tagging and E-L transformation, respectively, hereafter). Then, the stored Lagrangian droplets are utilized as the inlet boundary conditions for the combustion process.

4.2.2 Governing equations for dilute spray region

The combustion process occurring in the dilute spray region is modeled by a LES, utilizing the governing equations for the mass, momentum, and energy, and the detailed information can be found in studies [13–15]. To include the detailed chemical kinetics, a non-adiabatic version of flamelet/progress variable approach (NAPFV) [7, 16] is used for the modeling of the turbulence-chemistry interaction, which results in the solution of the following equations,

$$\frac{\partial \bar{\rho}}{\partial t} + \nabla \cdot (\bar{\rho}\tilde{\boldsymbol{u}}) = S_{\rho}, \tag{4.4}$$

$$\frac{\partial \bar{\rho}\tilde{\boldsymbol{u}}}{\partial t} + \nabla \cdot (\bar{\rho}\tilde{\boldsymbol{u}}\tilde{\boldsymbol{u}}) = -\nabla \bar{P} + \nabla \cdot (\bar{\boldsymbol{\tau}} + \bar{\boldsymbol{\tau}}_{sgs}) + S_{\rho \boldsymbol{u}}, \tag{4.5}$$

$$\frac{\partial \bar{\rho}\tilde{h}}{\partial t} + \nabla \cdot (\bar{\rho}\tilde{\boldsymbol{u}}\tilde{h}) = \nabla \cdot [\bar{\rho}(\widetilde{D_h}\nabla \tilde{h})] + \nabla q_h + Q_{rad} + S_{\rho h}, \tag{4.6}$$

$$\frac{\partial \bar{\rho}\tilde{Z}}{\partial t} + \nabla \cdot (\bar{\rho}\tilde{\boldsymbol{u}}\tilde{Z}) = \nabla \cdot [\bar{\rho}(\widetilde{D_Z}\nabla \tilde{Z})] + \nabla q_Z + S_{\rho Z}, \tag{4.7}$$

$$\frac{\partial \bar{\rho}\tilde{C}}{\partial t} + \nabla \cdot (\bar{\rho}\tilde{\boldsymbol{u}}\tilde{C}) = \nabla \cdot [\bar{\rho}(\widetilde{D_C}\nabla \tilde{C})] + \nabla q_C + \bar{\rho}\tilde{\dot{\omega}}_C, \tag{4.8}$$

where, the overbar, $-$, denotes the filtered mean value, and the tilde, $\sim$, denotes the Favre averaged value. $\tau_{sgs} = \bar{\rho}(\tilde{\boldsymbol{u}}\tilde{\boldsymbol{u}} - \widetilde{\boldsymbol{u}\boldsymbol{u}})$ is the subgrid term of the stress tensor, h the enthalpy, Z the mixture fraction. The mixture fraction is defined as the mass fraction of fuel stream, such that $Z = 1$ means a fuel stream and $Z = 0$ means an oxidizer stream. Following the work [7, 16], the progress variable C is defined as the summation of combustion products, i.e., $C = Y_{H_2O} + Y_{H_2} + Y_{CO_2} + Y_{CO}$. Y is the mass fraction of chemical species. D_h, D_Z, and D_C are diffusion coefficients of h, Z, and C, respectively. D_h is the gaseous thermal diffusivity given by $D_h = \lambda/(\rho c_p)$, D_Z and D_C are obtained

by assuming the unity Lewis number. λ is the heat conductivity, c_p is the specific heat capacity at constant pressure. q_h, q_Z, and q_C are the subgrid-scale (SGS) scalar fluxes, $q_\phi = \bar{\rho}(\widetilde{\boldsymbol{u}}\tilde{\phi} - \widetilde{\boldsymbol{u}\phi}), (\phi = h, Z, C)$. Q_{rad} is the radiation heat loss modeled by the weighted sum of gray gases (WSGG) model [17]. $\dot{\omega}_C$ is the source term of reaction progress variable. The eddy viscosity approximation is used to determine the $\boldsymbol{\tau}$ and q as follows,

$$\bar{\boldsymbol{\tau}}_{sgs} = \mu_t[(\nabla\tilde{\boldsymbol{u}}) + (\nabla\tilde{\boldsymbol{u}})^T)], \tag{4.9}$$

$$q_\phi = \bar{\rho}\alpha_t\nabla\tilde{\phi}, \tag{4.10}$$

where, μ_t and α_t denote the turbulent viscosity and eddy diffusivity, respectively, and are generally related in the formulation as $\alpha_t = \mu_t/(\bar{\rho}Sc)$ with a constant Schmidt number of $Sc = 0.4$ [18], where μ_t is determined by the dynamic Smagorinsky-Lilly model [19].

A non-adiabatic flamelet/progress variable approach (NAPFV), which can consider the effect of the heat loss caused by the latent heat of spray vaporization and radiation, is used. In order to generate the flamelet library, the following flamelet equations depending on the unity Lewis number assumption with heat loss are solved as follows,

$$\rho\frac{\partial Y_k}{\partial t} - \frac{\rho\chi}{2}\frac{\partial^2 Y_k}{\partial Z^2} - \dot{\omega}_k = 0, \tag{4.11}$$

$$\rho\frac{\partial T}{\partial t} - \frac{\rho\chi}{2}(\frac{\partial^2 T}{\partial Z^2} + \frac{1}{c_p}\frac{\partial c_p\partial T}{\partial Z\partial Z}) + \sum_k \frac{\rho\chi}{2}(\frac{\partial Y_k}{\partial Z} + \frac{Y_k}{W}\frac{\partial W}{\partial Z})(1 - \frac{c_{p,k}}{c_p})\frac{\partial T}{\partial Z}$$
$$+\frac{1}{c_p}\sum_k h_k\dot{\omega}_k + q'_{loss} = 0, \tag{4.12}$$

$$q'_{loss} = -\frac{\alpha}{c_p}\sum_k h_k\dot{\omega}_k, \tag{4.13}$$

where, the subscript k denotes the chemical species, χ is the scalar dissipation rate, $\dot{\omega}_k$ the reaction rate of species k, T the temperature, W the mean molecular weight of mixture, $c_{p,k}$ the specific heat capacity of species k at constant pressure, q'_{loss} the heat loss, α the heat loss rate parameter which can be varied from 0 to 1. Then a four dimensional flamelet library is obtained as,

$$\tilde{\varphi} = \tilde{\varphi}(\tilde{Z}, \widetilde{Z''^2}, \tilde{C}, \widetilde{\Delta h}), \tag{4.14}$$

where, Z''^2 is the variance of mixture fraction, Δh is the enthalpy defect due to heat loss, φ is the flame properties such as temperature, species mass fraction, and reaction

rate. Here, the adiabatic enthalpy h_a is calculated by Eq. 4.14 by assuming $\Delta h = 0$, i.e., $h_a = \tilde{h}(\tilde{Z}, \widetilde{Z''^2}, \tilde{C}, \widetilde{\Delta h} = 0)$, and thus the enthalpy defect Δh can be calculated by $\Delta h = h_a - h$, where h is determined with Eq. 4.6.

The influence of the evaporating droplets on the carrier gas flow is considered using the Particle-Source-In Cell (PSI-Cell) method [20]. S_ρ, $S_{\rho \boldsymbol{u}}$, $S_{\rho h}$, and $S_{\rho Z}$, which are the source terms for the mass, momentum, enthalpy, and mixture fraction originating from the dispersed droplets, respectively, are given as follows,

$$S_\rho = -\frac{1}{\Delta V}\sum_N \frac{dm_d}{dt}, \tag{4.15}$$

$$S_{\rho \boldsymbol{u}} = -\frac{1}{\Delta V}\sum_N \frac{dm_d \boldsymbol{u_d}}{dt}, \tag{4.16}$$

$$S_{\rho h} = -\frac{1}{\Delta V}\sum_N \frac{dm_d h_d}{dt}, \tag{4.17}$$

$$S_{\rho Z} = -\frac{1}{\Delta V}\sum_N \frac{dm_d}{dt} \quad \text{for fuel}, \tag{4.18}$$

where, ΔV is the volume of the unit grid, N is the number of droplets in the grid, and m_d, $\boldsymbol{u}_d$, and h_d are the mass, velocity, and specific enthalpy of the droplet, respectively.

Considering the non-equilibrium Langmuir-Knudsen evaporation model [13, 21], the governing equations used to track the droplet profiles such as the position, $\boldsymbol{x}_d$, velocity, $\boldsymbol{u}_d$, temperature, T_d, and mass, m_d, are given,

$$\frac{d\boldsymbol{x}_d}{dt} = \boldsymbol{u}_d, \tag{4.19}$$

$$\frac{d\boldsymbol{u}_d}{dt} = \frac{f_1}{\tau_d}(\tilde{\boldsymbol{u}} - \boldsymbol{u}_d), \tag{4.20}$$

$$\frac{dT_d}{dt} = \frac{Nu}{3Pr}\left(\frac{\tilde{c}_p}{c_{p,d}}\right)\left(\frac{f_2}{\tau_d}\right)(\tilde{T} - T_d) + \frac{1}{m_d}\left(\frac{dm_d}{dt}\right)\frac{L_V}{c_{p,d}}, \tag{4.21}$$

$$\frac{dm_d}{dt} = -\frac{Sh}{3Sc}\frac{m_d}{\tau_d} ln(1 + B_M), \tag{4.22}$$

Here, f_1 and f_2 are the correction coefficients for the Stokes drag and heat transfer for the evaporating fuel droplet, τ_d is the particle response time [22, 23], T the gas temperature, L_V the latent heat of evaporation at T_d, c_p and $c_{p,d}$ the specific heat of gas and fuel droplet, the Nusselt number and Prandtl number $Nu = 2 + 0.522 Re_{sl}^{1/2} Pr^{1/3}$ and $Pr =$

$\mu c_p/\lambda$, the Sherwood number and Schmidt number $Sh = 2 + 0.552 Re_{sl}^{1/2} Sc^{1/3}$ and $Sc = \mu/(\rho D_k)$, the mass transfer number $B_M = (Y_{F,s} - Y_F)/(1 - Y_{F,s})$. The detailed information of the droplet evaporation model can be found in our previous studies [13, 24–26]. The employed secondary breakup model is the Taylor analogy breakup (TAB) model [27].

4.3 Computational setup

4.3.1 Computational domains

A numerical framework is proposed in the present study, where the spray atomization and the subsequent combustion are simulated using different methods following an assumption that these two sub-processes usually occur in separated domains. Therefore, two computational domains are adopted and are marked as atomization and combustion domains, respectively, as shown in Fig. 4.1. In Fig. 4.1(a), the part depicted by the black line is the Sydney Burner, which consists of two concentric tubes, 1 and 2, surrounded by a pilot tube, 3. The inner tube, 1, is the liquid fuel nozzle with an inner diameter of $D_l = 0.686$ mm and wall thickness of 0.381 mm, and the outer tube, 2, is the air stream nozzle for the liquid fuel atomization with an inner diameter of $D_g = 10$ mm and wall thickness of 0.5 mm. The pilot tube, 3, is used to supply the hot combustion products through an inner diameter of $D_p = 25$ mm and wall thickness of 0.2 mm. The concentric tubes are adjustable such that the distance from the liquid fuel nozzle to the pilot outlet is variable, enabling the Sydney Burner to supply a dense or dilute spray for the combustion. The distance is called the recess distance and is referred to as Lr in the present and related studies [2–4], ranging from 0 to 80 mm. The present study selected two different flame cases, N-AF8-25 and N-AF8-80 which hold different Lr values, $Lr =$ 25 and 80 mm, respectively.

However, for the atomization computation, the case of $Lr = 80$ mm requires a much higher computational cost than that of $Lr = 25$ mm. Therefore, only the N-AF8-25 case atomization process is calculated, which is depicted by the solid and dotted blue lines in Fig. 4.1(a), and is shown in Fig. 4.1(b) in detail. The atomization domain

consists of a region with a wall boundary having a length of 25 mm corresponding to the experimental recess distance and a free boundary of 25 mm. Two atomization-combustion coupling (ACC) planes are set in the atomization domain. These are utilized to transform the Eulerian components into the Lagrangian droplets and serve as the inlet boundary conditions for the combustion simulation. To investigate the influence of different ACC positions on the E-L transformation, one plane is set at 5 mm upstream of the pilot outlet (ACC1) and the other is 5 mm downstream of the pilot outlet (ACC2).

The combustion domain is depicted by the red line in Fig. 4.1(a), the details of which are presented in Fig. 4.1(c). The entire combustion domain holds a diameter of $D_c = 104$ mm. In the axial direction, the inlet boundary is placed at the ACC plane, whose distance to the pilot outlet is marked as L_1. Since the recess distance of N-AF8-25 and N-AF8-80 are adjusted to 25 and 80 mm to produce dense and dilute sprays, L_1 holds two values of 10 and 65 mm for N-AF8-25 and N-AF8-80, respectively, and the other parameters $L_2 = 1000$ mm, $L_3 = 75$ mm, and $L_4 = 135$ mm are kept the same in both cases.

The cylindrical coordinate system with the unstructured grids is utilized for both atomization and combustion simulations. The atomization computational domain has a total of 24.6 million grid points, with a non-uniform mesh size ranging from 8 to 100 µm in the radial direction, and a uniform mesh size of 100 µm in the axial direction. The combustion computational domain has a total of 18 million grid points, with an increasing mesh size of 0.13 to 3 mm in the radial direction, and a variable mesh size of 0.15 to 3.5 mm in the axial direction. In addition, the Hinze scale $\eta_H = \sigma/(\rho_g U_g^2)$ in the atomization computation is estimated to be 8.54 µm and the mesh size holds 1-10 η_H. As suggested in our Chapter 2 and regarding this simulation reaches to the experimental scale, it could be considered as a high-resolution VOF simulation.

4.3.2 Computational conditions

For the atomization computation, the temperature and pressure are set to room temperature and atmospheric pressure, and hence, both the liquid fuel and air have a tempera-

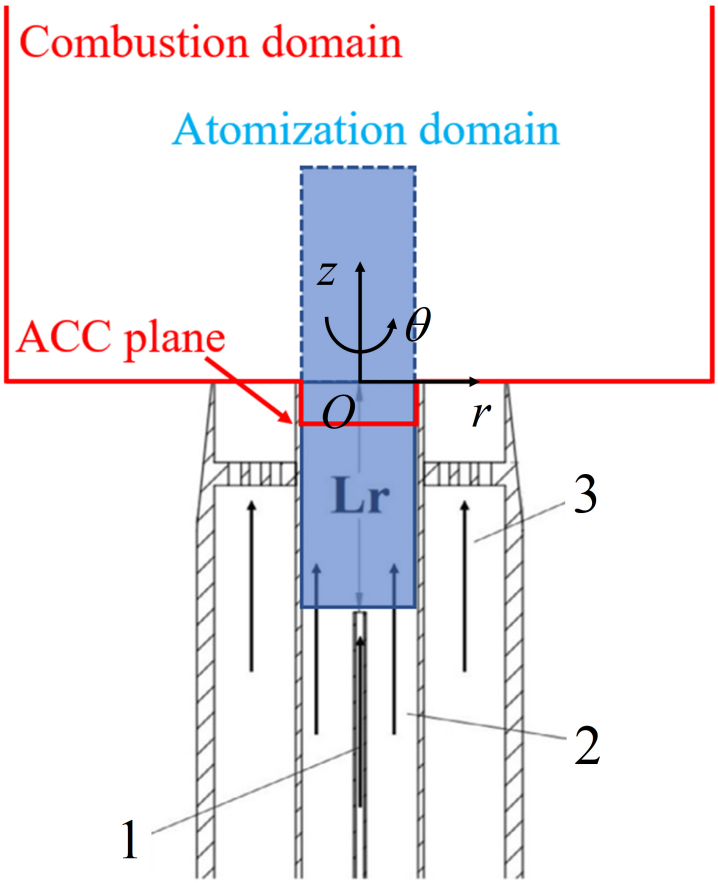

(a) Computational domains of atomization and combustion. 1, 2, and 3 refer to liquid fuel nozzle, air stream nozzle, and pilot tube, respectively and ACC refers to atomization-combustion coupling plane

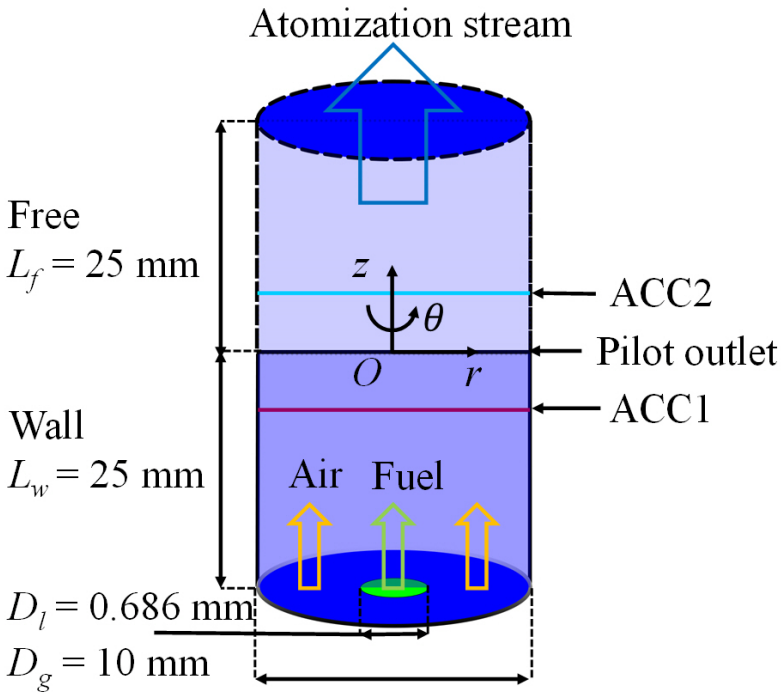

(b) Computational domain of atomization

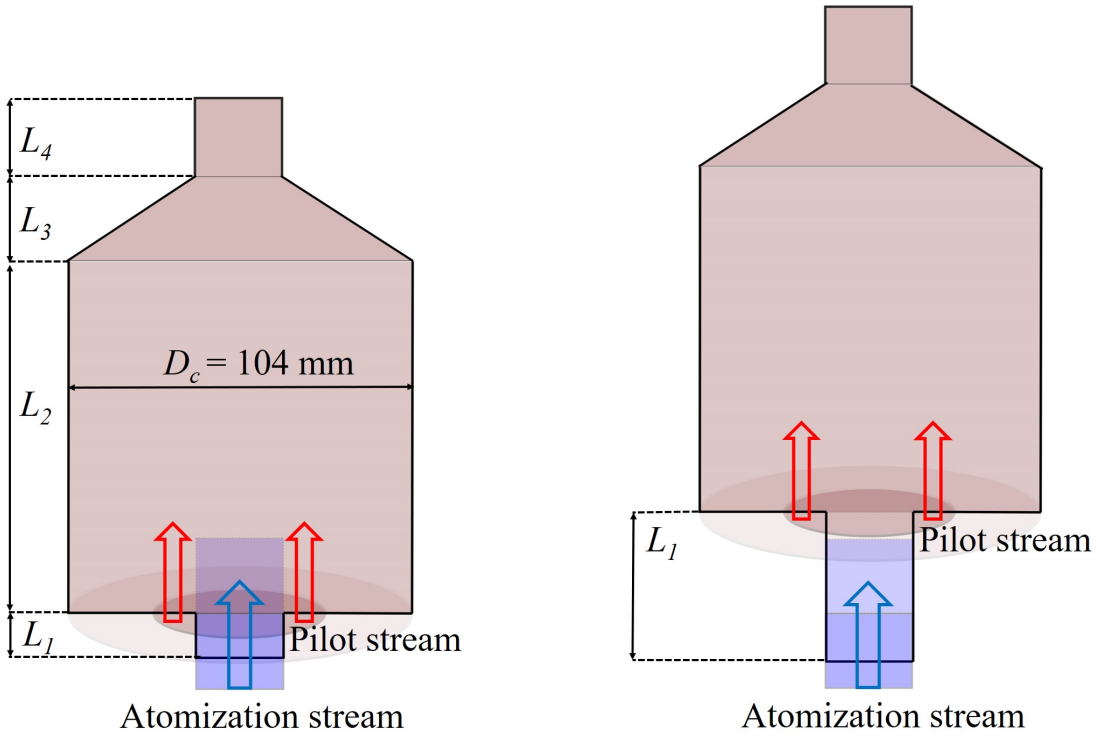

(c) Computational domains of combustion (left: N-AF8-25; right: N-AF8-80)

Figure 4.1: Schematics of computational domains.

ture of 300 K, which can be regarded as a cold state for only atomization, neglecting the evaporation effect. Therefore, the air viscosity, μ_g, is 1.81×10^{-5} Pa·s, and liquid viscosity, μ_l, is 3.33×10^{-4} Pa·s, the liquid-gas surface tension, σ, is 2.37×10^{-2} N/m. At the inlet, both the liquid and carrier gas velocities, u_l and u_g, are assigned as 2.57m/s and 48 m/s with a flat laminar velocity profile, respectively, according to the experiments [3, 4]. Thus, in both configurations, i.e., N-AF8-25 and N-AF8-80, the dimensionless parameters, including the aerodynamic Weber number, $We = \rho_g u_g^2 D_l/\sigma$, evaluated as 80, the liquid jet Reynolds number, $Re_l = 4161$, as well as the carrier gas Reynolds number, $Re_g = 31823$, are close to the experimental conditions, as shown in Thomas and Lowe's works [3, 4]. The parameters used in the atomization computation are shown in Table 1.

After the atomization computation, the droplets are transformed into the Lagrangian droplets, which are stored in a database for the following combustion computation. Droplets recorded at the ACC plane of the atomization domain are directly injected into

Table 4.1: Parameters for atomization simulation.

Physical properties	
Liquid fuel	Acetone
Gas	Air
Liquid nozzle diameter, D_l (mm)	0.686
Liquid jet velocity, u_l (m/s)	2.57
Liquid jet viscosity, μ_l (Pa·s)	3.33×10^{-4}
Liquid jet density, ρ_l (kg/m^3)	786
Liquid jet temperature, T_l (K)	300
Liquid jet Reynolds number, Re_l (-)	4161
Gas jet diameter, D_g (mm)	10
Gas jet velocity, u_g (m/s)	48
Gas jet viscosity, μ_g (Pa·s)	1.81×10^{-5}
Gas jet density, ρ_g (kg/m^3)	1.20
Gas jet temperature, T_g (K)	300
Gas jet Reynolds number, Re_g (-)	31823
Liquid-gas surface tension, σ (N/m)	2.37×10^{-2}
Ambient pressure, P (MPa)	0.1
Aerodynamic Weber number, We (-)	80

the combustion domain at the ACC plane at a fixed time step determined by satisfying the step interval of the combustion computation, which are explained in the following section. When these cold Lagrangian fuel droplets flow out of the nozzle and face the hot pilot gases, combustion occurs after the evaporation and mixing with the combustion products from the pilot that is in the stoichiometric condition and has a velocity of 1.5 m/s. Two different gas velocity profiles: (1) a uniform flat gas velocity that equals to 48 m/s; (2) a gas velocity profile extracted from the atomization computation, are performed to study the influence of different inlet gas velocity profiles.

The flamelet calculations for the flamelet library generation are conducted with FlameMaster code [28]. The numbers of grids set for $\tilde{Z}$, $\widetilde{Z''^2}$, $\tilde{C}$, and $\widetilde{\Delta h}$ are $100 \times 20 \times 100 \times 10$. The reaction mechanism for acetone/air combustion proposed by Pichon et al. [29] is employed, which consists of 81 species and 416 reactions.

The computational costs for single realization of atomization and combustion simulations, performed on the Kyoto University Supercomputer (Cray XC40), are around 430k core·hours (840 hours in real time using 512 cores), and 250-350k core·hours (230-340

hours in real time using 1088 cores), respectively.

4.4 Results and discussion

4.4.1 Atomization and E-L transformation

In the experiments of the dense sprays, it is difficult to acquire confident droplet size distribution owing to the diagnostics limitation. In fact, Lowe et al. [4] reported that large numbers of ligaments and irregular shaped objects are formed before secondary breakup. Those ligaments and irregular shaped objects are considered to more likely increase the turbulence in the flow field. Although such liquid ligaments and irregular shaped objects are also observed in the present simulation, those are forced to be transformed into Lagrangian sphere droplets using a E-L tagging method owing to the limitation of the consideration of those shapes. The influence of this will be discussed later.

The E-L tagging method is used to recognize the dispersed Eulerian components generated by the primary breakup during the atomization process and transfer their properties into the Lagrangian droplets, which are later directly placed in the computational domain to replace the Eulerian components. The E-L tagging method is explained in detail in Chapter 2, but the details are different. In Chapters 2 and 3, the evaporation effects of droplets have to be considered such that the Eulerian droplets must be transformed into Lagrangian droplets while they are generated, thus increasing the computational cost. However, in this chapter, the droplets profiles should be recorded once it passes a downstream cross-section, that is, the ACC plane as shown in Fig. 4.1(b), in the atomization computational domain. Therefore, the E-L transformation is triggered only if the Eulerian droplet passes through the ACC plane. A buffer region is created at the upstream of the ACC plane, and the Eulerian components in this buffer region that can pass through the ACC plane within one sampling time interval are transformed into Lagrangian droplets and then saved in the database for subsequent combustion. Because the computational time interval used for the combustion simulation is 1×10^{-5}

s, and that for the atomization simulation is 5×10^{-8} s, the sampling time interval is thus set as 200 steps of the atomization computation, that is, 1 step of the combustion simulation.

Figs. 4.2 and 4.3 show comparisons of the position, size, and axial velocity between the Eulerian components and the transformed Lagrangian droplets. Generally, a good agreement is observed. Specifically, it can be seen that the Lagrangian droplets with a red color match the large Eulerian components in both the droplet position and size. A good match is also shown for the small droplets with a green color. Such an agreement of the axial velocity profiles can also be found in Fig. 4.3. Therefore, the present E-L tagging method can work properly to transform Eulerian components into the Lagrangian droplets.

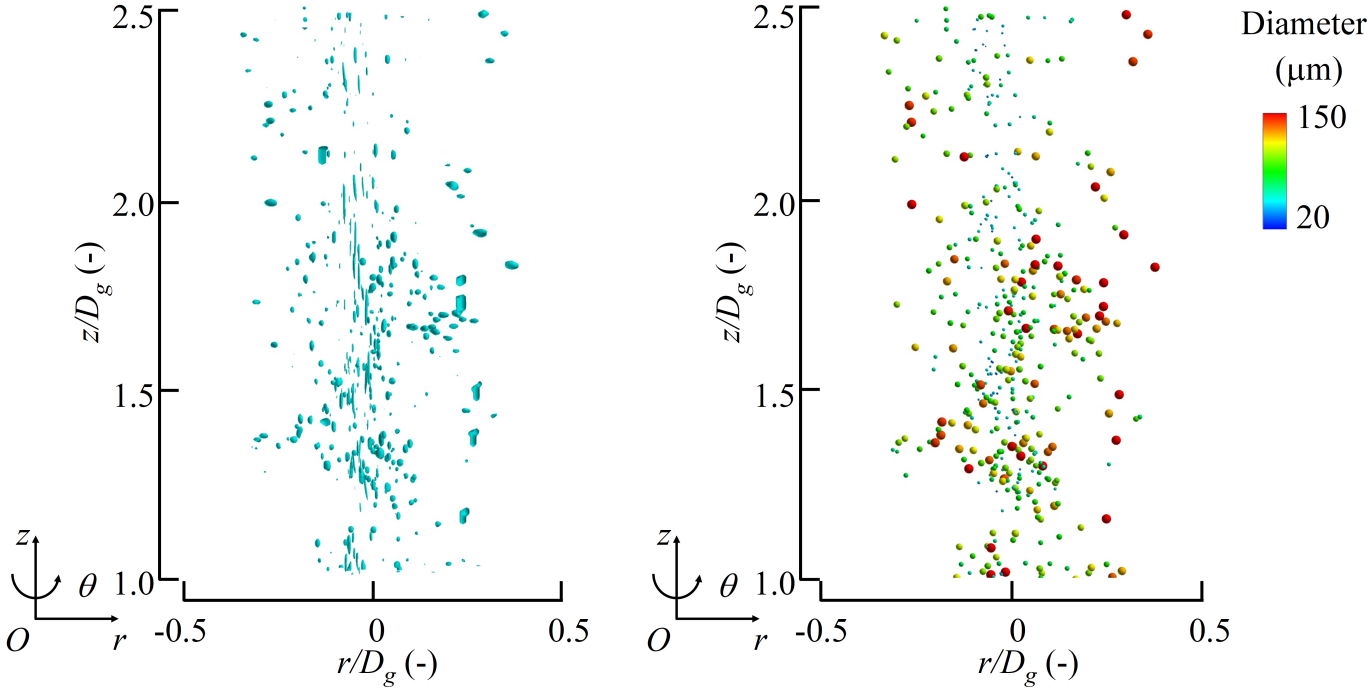

(a) Eulerian components

(b) Lagrangian droplets

Figure 4.2: Comparison of droplet position and size distributions between Eulerian components and Lagrangian droplet at $1.0 \leqslant z/D_g \leqslant 2.5$ and $-0.5 \leqslant r/D_g \leqslant 0.5$ (Lagrangian droplets are colored and scaled by diameter size).

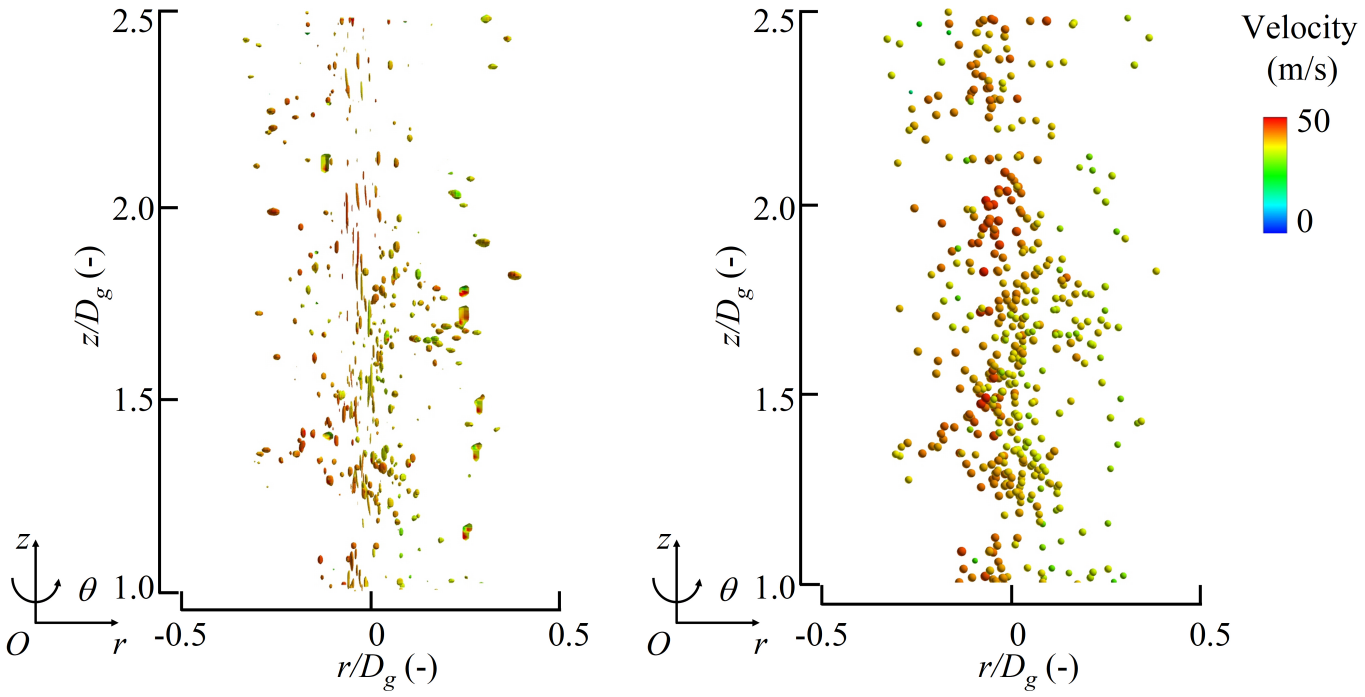

(a) Eulerian components

(b) Lagrangian droplets

Figure 4.3: Comparison of axial velocity and position distributions between Eulerian components and Lagrangian droplets at 1.0$\leqslant z/D_g \leqslant$2.5 and -0.5$\leqslant r/D_g \leqslant$0.5 (Eulerian components and Lagrangian droplets are colored by velocity).

4.4.2 Atomized droplets database

4.4.2.1 Database concept and droplet size distribution

To confidently build a database serving as the inlet boundary conditions for the combustion computation, the critical factors affecting the atomization properties should be carefully checked. The present E-L tagging method includes three important parameters, i.e., the downstream distance from the fuel nozzle to the ACC plane, Z_0, the threshold value of the E-L tagging method, and the total sampling time for recording the droplets profiles. Regarding the downstream distance Z_0, with a smaller Z_0, where the liquid jet is not fully developed, the E-L tagging method cannot transform the ligaments and irregular shaped objects into larger Lagrangian blobs, which is unrealistic, resulting in mass loss; however, with a larger Z_0, where less ligaments exist there and the Eulerian droplets are easily transformed into the Lagrangian droplets, the E-L tagging method also loses its accuracy owing to the numerical diffusion since the cells might hold

diffused VOF values and the unexpected transformed Lagrangian droplets. Therefore, two different ACCs, i.e., one is 5 mm upstream of the pilot outlet (ACC1) and another is 5 mm downstream of the pilot outlet (ACC2), which are shown in Fig. 4.1(b), are exhibited to check the confidence of the position. On the other hand, considering the threshold values used in the E-L tagging method, a smaller threshold, which can recognize the tiny Eulerian droplets, increases the risk of numerical error caused by numerical diffusion, some of which are simply numerical noise and referred to as fake droplets. However, a larger threshold neglects those droplets with a small scale in comparison to the local grid size, losing realistic small droplets, which have a significant influence on the subsequent evaporation and combustion properties. Thus, three different thresholds, ψ_{cri} = 0.1, 0.05, and 0.01, are selected and their validities are examined. Hence, four different databases can be acquired, as presented in Table 2. Note that the atomization simulation is only calculated once under the condition shown in Table 1, and the droplet databases are obtained during the simulation by setting different ACCs and thresholds.

Table 4.2: Databases acquired in atomization simulation.

Database	ACC plane	Threshold for E-L transformation	volumetric particle loading
A1	ACC1	0.1	7.40
A2	ACC2	0.1	9.28
A3	ACC2	0.05	9.84
A4	ACC2	0.01	11.22

Fig. 4.4 shows the atomization behavior in the front view and at the cross-sections of ACC1 and ACC2, the colored surface of which is the iso-surface of the E-L tagging method threshold of 0.1, i.e., the liquid-phase volume fraction of the grids is larger than 10%. The liquid column starts to show instability around the downstream at z/D_g = -2.25, and twists at approximately z/D_g = -1.75. When it passes z/D_g = -1.5, a breakup behavior can be observed. The liquid column becomes discontinuous, and

smaller droplets and some ligaments and irregular shaped objects can be found around the z/D_g = -1.0. Beyond z/D_g = -0.5, most of the visible liquid phase is due to dispersed droplets, which tend to flow away from the center axis. By comparing the cross-sections of ACC1 and ACC2, the existing droplets are found to be denser at ACC1, and the downstream droplets at ACC2 reach further in the radial direction.

Fig. 4.5 shows the droplet profiles in different databases, plotted with droplet diameters which are binned over 10 µm interval for droplets up to 50 µm, 20 µm interval for droplets from 50 to 150 µm, and 50 µm interval for droplets with size above 150 µm. For Fig. 4.5(a), with the ACC plane going downstream and increasing the threshold of the E-L tagging method, the peak of the PDF value changes from 70 to 30 µm. By comparing the droplet size distributions of A1 and A2 in three different clusters, i.e., 0-50 µm, 50-150 µm, and 150-200 µm, there are few differences between both cases, indicating occurrences of further breakup. Moreover, the threshold of the E-L tagging method seems to have a more significant influence on the droplet size distribution than the ACC position by comparing the differences between A2 and A4 as well as A1 and A2. By applying a larger threshold, more droplets with the diameter less than 50 µm seem to be captured with the value of 0.99. By comparing the total droplet volume of different databases shown in Fig. 4.5(b), all databases show a similar total droplet mass, which means that almost of the Eulerian components are captured by the present E-L tagging method. In addition, one thing worth noting is that for a large Lagrangian droplet, which might be comparable to the mesh size, the mass and momentum interactions between gas phase and the Lagrangian droplet are decided by the surrounding cells instead of the local cell such that the Lagrangian droplet could be still considered as a point by the PSI-Cell method.

Because this study is focused on dense spray, the volumetric particle loading of droplets in the computational domain is further checked, as shown in Table 2. Here, the ratio of droplet distance and droplet diameter is presented instead of simple volume fraction, which can refer to as S/d in Elghobashi's work [30], where, S indicates the distance between the centers of two neighboring droplets, and d denotes the diameter

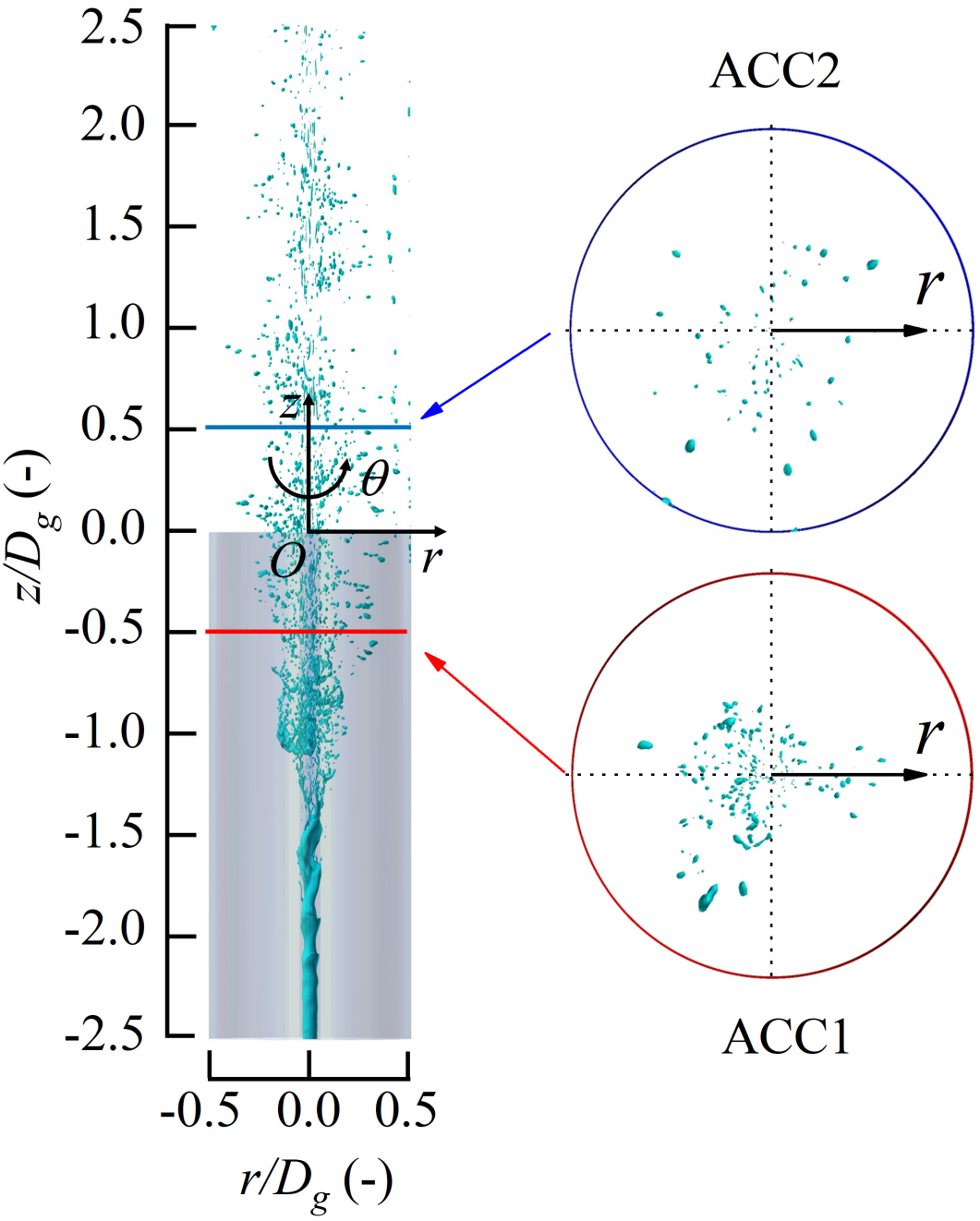

Figure 4.4: Atomization behavior and the Eulerian components distributions at ACC1 and ACC2 ($\psi_{cri} = 0.1$).

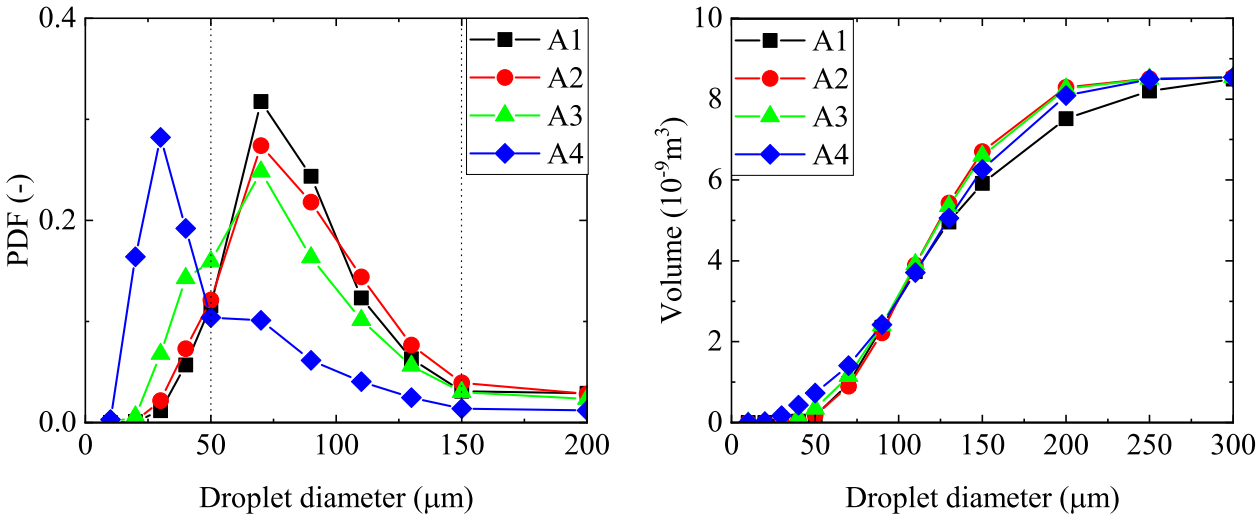

(a) PDF

(b) Accumulated volume

Figure 4.5: Droplet size distribution in terms of (a) PDF and (b) accumulated volume of different atomization databases (A1-A4).

of droplet. With $S/d \geqslant 10$, the two-way coupling method could be employed in this study instead of four-way coupling. When the ACC plane is set further downstream, the droplets can reach further in the radial direction, which can refer to the cross-sections of ACC1 and ACC2 in Fig. 4.4, and thus A2 shows a larger value than A1, indicating a more dilute spray compared with A1.

4.4.2.2 Droplet spatial and temporal size distributions

In traditional combustion simulations, the sizes of droplets issued from the inlet boundary are often given using a simple atomization model or a presumed droplet size distribution. In this study, on the other hand, those are induced from a database resulting from the atomization computation. Therefore, the sampling time of atomization computation should be carefully discussed. To obtain a symmetrical flame structure without any preferences in any directions, the spatial distribution of the droplets must be checked such that the position profile should be spatially homogeneous without any biases in any directions. For example, many more larger droplets can be found in $\pi \leqslant \theta < 3\pi/2$ and fewer droplets can be found in $0 \leqslant \theta < \pi/2$ at ACC1, and larger droplets are observed on

the right side at ACC2, as shown in Fig. 4.4, thus the droplets distribution shows some preferences if the sampling time is insufficient.

The complexity of the azimuthal homogeneity analysis increases if the droplet size is further considered. Fig. 4.6 shows the Sauter mean diameter (D_{32}) and arithmetic mean diameter (D_{10}) radial distributions obtained from the different databases. The droplet size for either D_{32} or D_{10} increases as the droplets flow further away from the central axis, which means that the droplet size has a strong correlation with the radial distribution, and thus it is sufficient to base the analysis for azimuthal homogeneity on investigating the droplet size with different angles θ in the radial plane. The droplet size can be used to represent the radial distance between the droplet and the center axis, and the angle θ can be used to represent different radial directions. In addition, referring to the experimental study [4] based on the Sydney Burner of N-AF8-25 and N-AF8-80, which only supplies the D_{32} distributions along the center axis (see Fig. 12), D_{32} is always less than 60 µm. Given that the database of A4 holds the D_{32} value less than 60 µm, whereas those of other three cases are larger than 60 µm, the database A4 provides a better droplet size distribution according to the experiment.

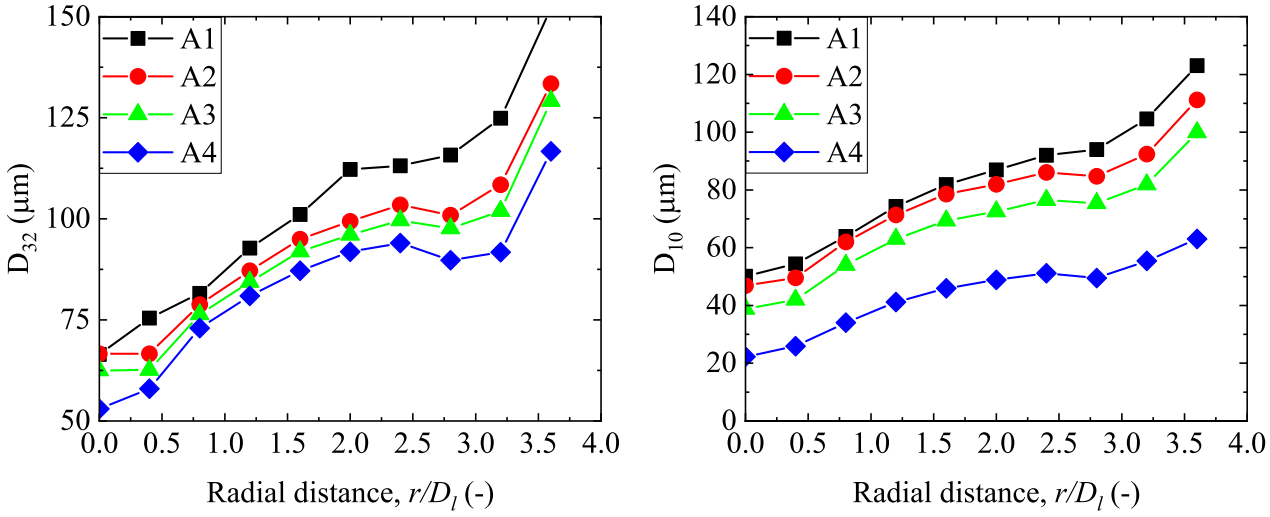

(a) D_{32} (b) D_{10}

Figure 4.6: Radial distributions of droplet size in (a) D_{32} and (b) D_{10} for different atomization databases (A1-A4).

To obtain a sufficient number of reliable data for a homogeneous analysis, the sampling time and interval are discussed. The sampling interval is set 1×10^{-5}s, which is 200 steps for the atomization computation and 1 step for the combustion computation, and thus the combustion simulation can simply read the data in a step-by-step manner. Fig. 4.7 shows the time variations of droplet volume through ACC1 plane and through each quadrant of ACC1 plane, from the 120,000th step, in which the liquid jet is thought to be fully developed and starts to steadily breakup, to the 300,000th step, which is thought to be long enough for sampling. Five periods can be observed in Fig. 4.7(a) showing that the atomization process holds a periodic characteristic with breakup and non-breakup periods. In Matas's study [31, 32], the frequency of the liquid jet breakup is found to have a strong relation to the gas and liquid velocities as well as the nozzle size, and the empirical correlations are shown as follows.

$$f = (\sqrt{\frac{\rho_g \delta_l}{\rho_l \delta_g}} u_g + u_l)/D_g, \tag{4.23}$$

$$\delta = v_0/max(\frac{dv}{dr}). \tag{4.24}$$

where δ is the thickness of the vorticity layer, v denotes the radial velocity, and v_0 is the radial velocity measured near the Sydney Burner nozzle, e.g., $z/D_g = 0$. The thickness of the vorticity layer of liquid and gas phases, δ_l and δ_g are directly acquired in the simulation. By this correlation, the calculated result is 547 Hz, and the mean period shown in Fig. 4.7(a) is simply calculated as 556 Hz. Therefore, the present detailed numerical simulation and the E-L tagging method are considered to be reasonable to reproduce the atomization phenomena. Fig. 4.7(b) shows the variations of droplet volume through each quadrant of ACC1 plane, and it could be observed that the droplet volume of each quadrant shows totally different values in different breakup periods. For example, for the quadrant of $3\pi/2$-2π, it holds larger values in the later time in each breakup period except for the 3rd period between 3-5 ms. Fig. 4.8 also shows the time variations of D_{32} and D_{10} through each quadrant of ACC1 plane in each a half breakup period. It could be observed that the values of D_{32} and D_{10} in each a half breakup period are totally different such that the droplet sampling time for acquiring a homogeneous distribution

need to be further checked.

By comparing the D_{32} and D_{10} distributions in Fig. 4.6, the droplet size has a strong correlation with the radial distance, that is, the closer the droplets to the center axis, the smaller the droplets are. Therefore, the angle θ in the radial plane and the droplet size can be used to analyze the droplet spatial distribution by the Chi-square homogeneity check, the detail of which can be found in Appendix A.

Table 4.3: Chi-square homogeneity check for the database A1.

A1	0-$\pi/2$	$\pi/2$-π	π-$3\pi/2$	$3\pi/2$-2π	Total
0-50 µm	0.12	0.27	4.88	1.77	7.04
50-150 µm	0.11	0.02	0.78	0.16	1.07
150-300 µm	0.56	0.22	0.80	1.32	2.9
Total	0.79	0.51	6.46	3.25	11.01

Table 3 shows the calculated chi-square values of the database A1 with a sampling time starting at the 120,000th step and ending up with the 300,000th step, covering five full-breakup periods. Compared to other cells, there is an odd value particularly larger than the others, which is marked as red in $\pi \leqslant \theta < 3\pi/2$ with a diameter of less than 50 µm. It means that in the region $\pi \leqslant \theta < 3\pi/2$, more droplets with a diameter of less than 50 µm exist compared to the other three regions. Because the number of droplets with diameter of less than 0-50 µm is very small in the database A1 (see Fig 4.5(a), black line), it is reasonable to observe such a bias that some region holds a different number of droplets because the droplets generated by the breakup fluctuate spatially and temporally. However, the total value of this case is 11.01, which is less than the critical value of 12.59, ensuring that the spatial distribution of the droplets has no obvious bias by sampling the five breakup periods from the 120,000th step to the 300,000th step.

Fig. 4.9 shows the total values of each database by employing different sampling times from one to five periods. The total values of A1 and A2 continue decreasing when

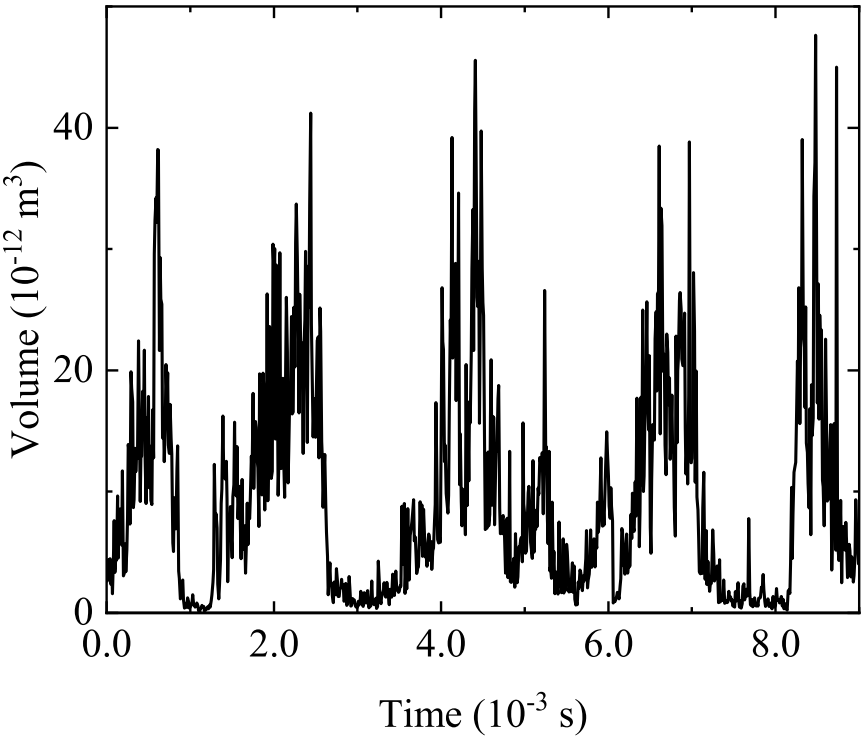

(a)

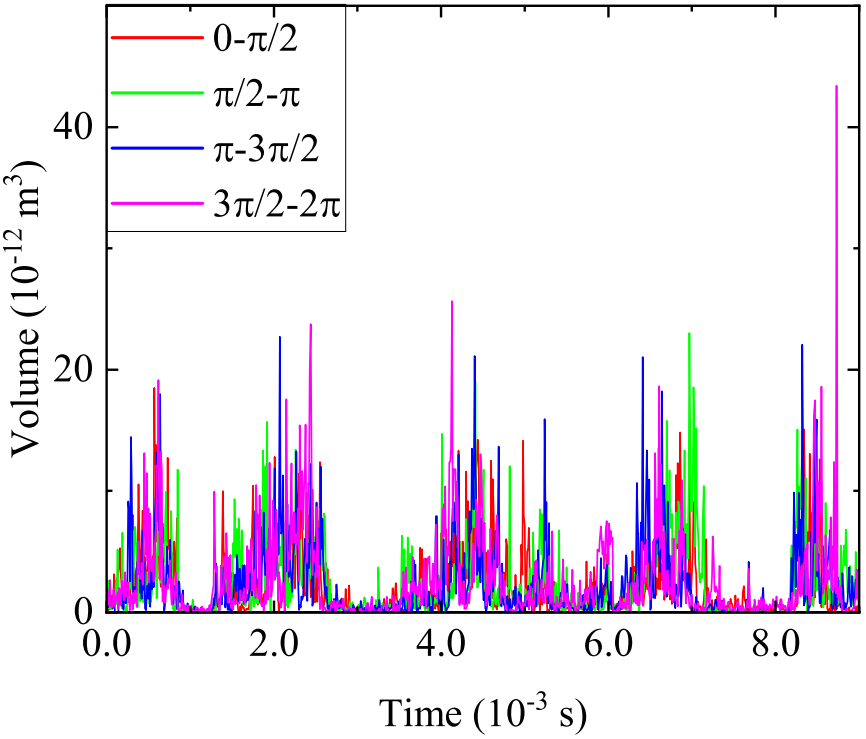

(b)

Figure 4.7: Time variations of droplet volume through ACC1 plane for the database A1: (a) in total, (b) each quadrant.

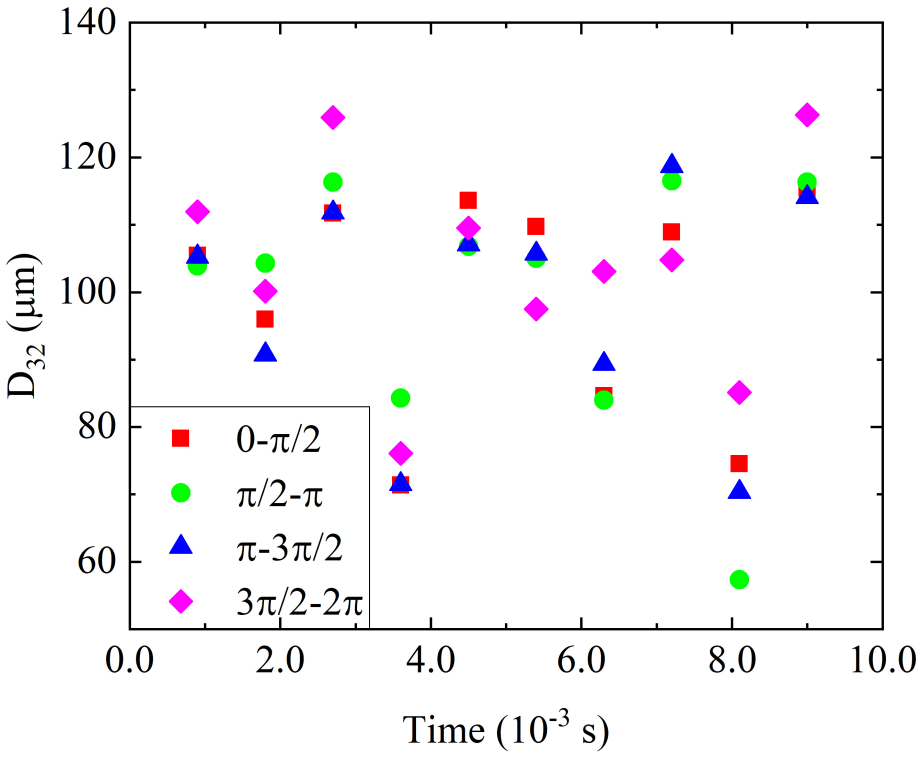

(a)

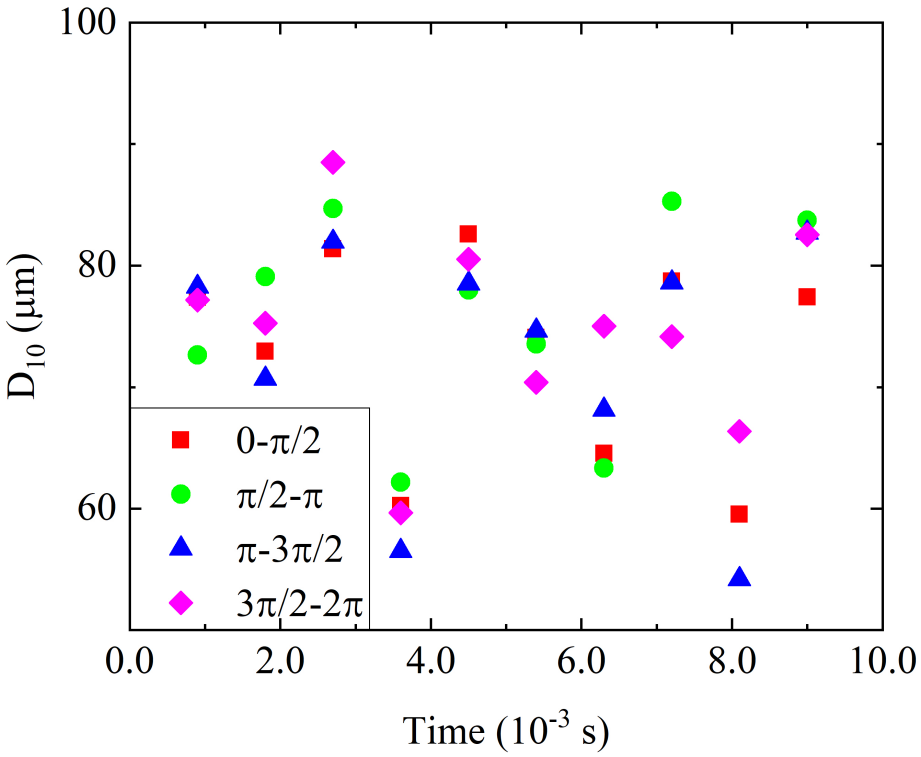

(b)

Figure 4.8: Time variations of D_{32} and D_{10} of droplets through each quadrant of ACC1 plane for the database A1: (a) D_{32}, (b) D_{10}.

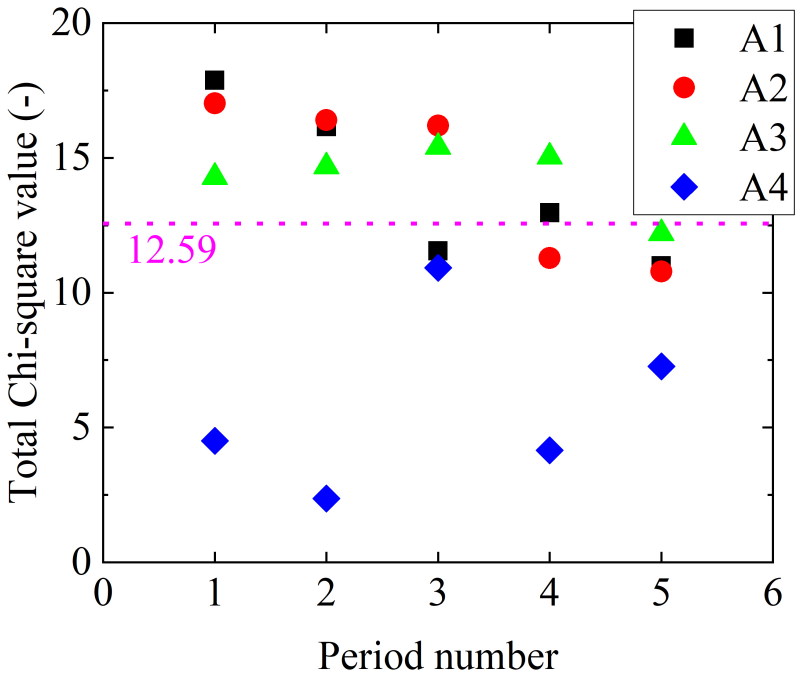

Figure 4.9: Total values of different databases A1-A4 with different sampling time.

the sampling time is increased from one to five periods, out of which the total values of A4 continue fluctuating because the number of small droplets with a diameter of 0-50 µm of A4 is larger than those of the other three cases, thus those odd values (an example is shown in red in Table 3) are decreased such that the total value is much smaller than those of the other three cases. By sampling five breakup periods, all four databases hold reasonable total values to ensure the azimuthal homogeneity, and the sampling time is thus selected to be five breakup periods from the 120,000th step to the 300,000th step.

In total, for the atomization computation, the physical time is 15 ms, in which the first 6 ms is used for the liquid jet development to reach a steady state, and the last 9 ms is used for the droplet database sampling discussed in this section. For the combustion computation, the physical time is 100 ms such that the particle injection is cycled about 11 times.

4.4.3 Combustion characteristics

4.4.3.1 Simulation cases and flame features

As mentioned in Section 3.1, two different configurations, N-AF8-25 and N-AF8-80, are utilized with representative recess distance of 25mm and 80mm. In addition, two different inlet gas velocity profiles, one flat and the other extracted from the atomization computation, are incorporated to study the sensitivity of the dense spray flame to the inlet boundary conditions. Further, considering the computational cost, out of the four databases of A1 to A4 two databases, A1 and A4, are selected to investigate the influence of the droplet inlet boundary conditions on the flame characteristics because A1, A2, and A3 display similar droplet size profiles of D_{32} and D_{10}, whereas A1 holds different gas velocity compared to A2-A4. Therefore, a total of six cases are discussed as shown in Table 4, Fig. 4.10 provides a clear schematic of the conducted six cases. The orange lines depicted in the figure indicate the ACC planes, where the gas velocity profiles and droplets are recorded in the atomization computation and are applied in the combustion computations as the inlet boundary conditions. In addition, the axial distance of the ACC plane Z_{ACC} relative to the pilot outlet, is displayed for a better understanding.

Table 4.4: Conducted cases for combustion simulation.

Case	Velocity profile	Atomization database	Configuration
1	Flat	A1	Dense (N-AF8-25)
2	Atomization	A1	
3	Atomization	A4	
4	Flat	A1	Dilute (N-AF8-80)
5	Atomization	A1	
6	Atomization	A4	

In dense sprays, laser diagnostic measurements are difficult owing to the co-existence of liquid fragments and abundant atomized droplets, which reflect and absorb the light. Therefore, a chirped-probe-pulse femtosecond coherent anti-Stokes Raman spectroscopy

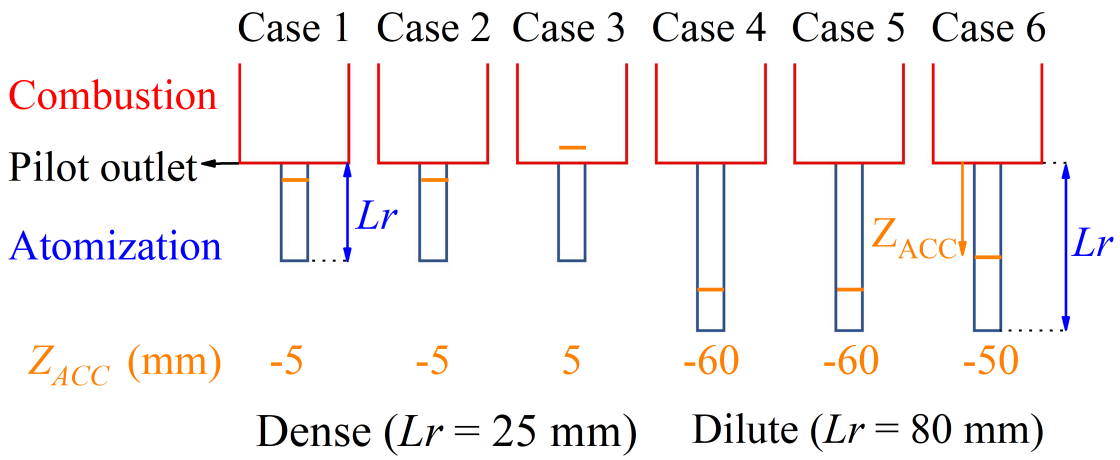

Figure 4.10: Conducted cases and schematic of locations of recess distance, Lr, and ACC planes, Z_{ACC}, for combustion in detail.

(CPP-fs-CARS) with a repetition rate of 5 kHz was employed by Thomas and Lowe [3, 4] to measure the temperature distribution based on the platform of the Sydney Burner, which supplies various temperature profiles ranging from dense to dilute sprays with ethanol and acetone fuels. The temperature distributions in both the dense and dilute sprays with the acetone fuel are considered in this work to validate the proposed numerical simulations.

Fig. 4.11 shows the instantaneous temperature profiles and fuel droplets distribution for Case 3 and Case 6. The double reaction zone, where a premixed core is inside a surrounding non-premixed zone, can be observed. The premixed cores are extended in both the span and axial directions despite the recess distance changes from 25 to 80 mm. Meanwhile, each temperature iso-surface in Case 3 is shorter than that of Case 6, which means that the dilute spray (Case 6) with a longer recess distance can enhance the mixing and combustion processes.

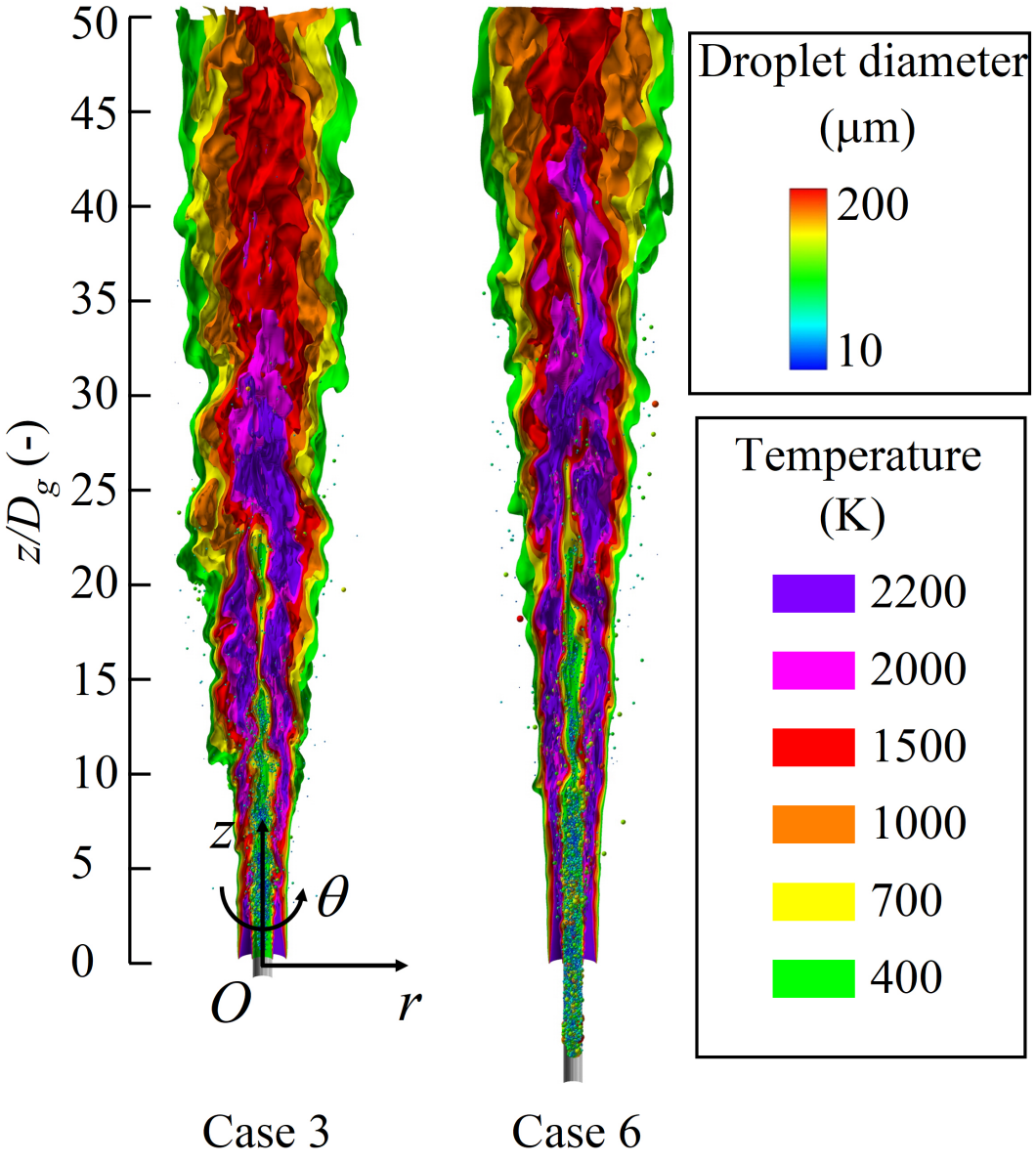

(a) Whole region

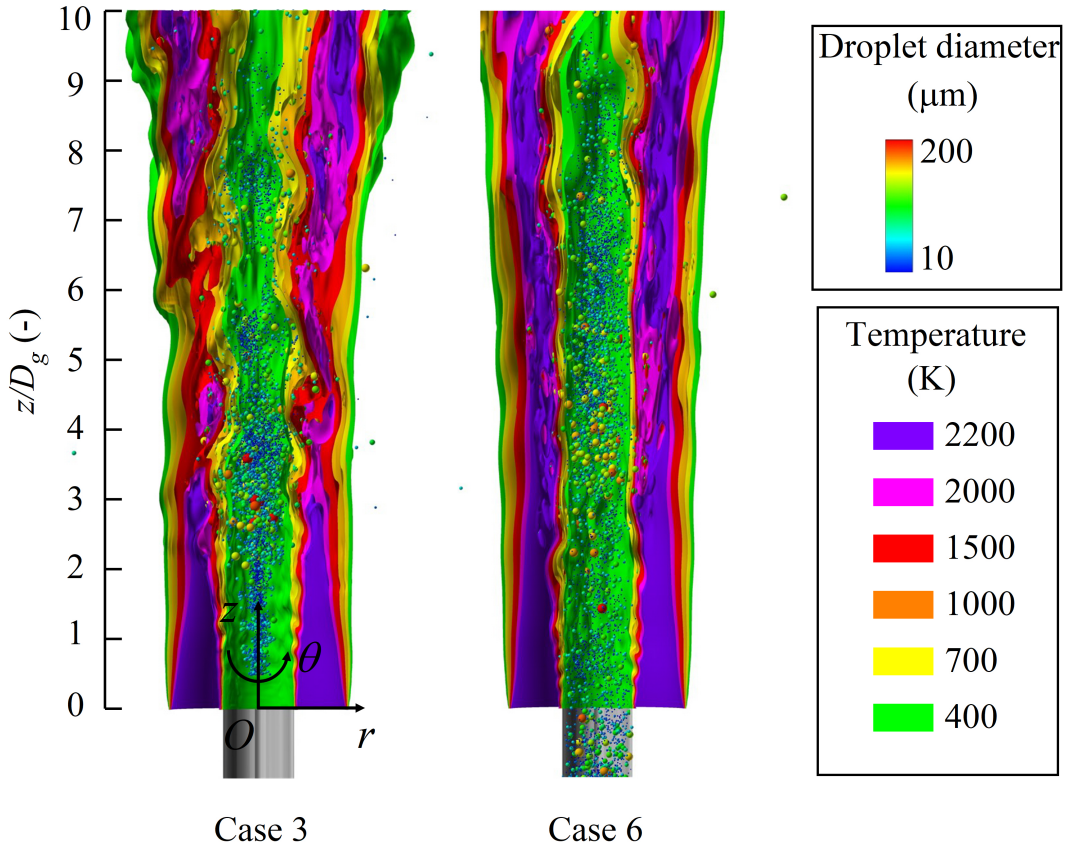

(b) Near nozzle region

Figure 4.11: Instantaneous temperature iso-surface and droplet distribution for Case 3 and Case 6.

4.4.3.2 Comparisons with experiments

Figs. 4.12 and 4.13 show the radial distributions of the time-averaged and RMS of gas temperature at different axial downstream locations, z/D_g = 3, 5, 10, and 20, where the experimental data are compared with simulations of Case 1 to Case 6 detailed in Table 4. The influences of the inflow gas velocity profiles and inflow droplet profiles are discussed.

The computed results of the mean gas temperature depict a symmetric unimodal distribution at different axial locations, and at the downstream of $z/D_g = 20$, the peak temperature is suppressed. However, based on the experiments at $z/D_g = 20$, the symmetric unimodal distribution is absent for the dense case, and is still distinguished in the dilute case. The reason for this difference is thought to be the result of a higher proportion of fragments and filaments presented in the dense case [3, 4], which leads to a less stable and lower mean temperature. By contrast, at the upstream locations of $z/D_g = 3$, the flame is more dominated by the pilot flame such that the reaction zone is less affected by the spray properties and a similar temperature profile is observed for both dense and dilute flame cases. Regarding the simulation results, the atomization velocity presents its priory in comparison to the flat one, showing a good agreement with experiments at the upstream region. Even for the $z/D_g = 10$ of the dilute cases, the temperature distribution still matches very well. For both cases with atomization velocity profiles, the temperature distributions do not show much difference though the D_{32}, D_{10}, and PDF distribution of droplet diameter show a significant difference (see Fig. 4.5(a) and Fig. 4.6(b)). However, some discrepancies can still be observed, i.e., cases with atomization gas velocity and smaller droplets (Case 3 and Case 6) have intermediate values between the cases with flat gas velocity and larger droplets (Case 1 and Case 4), and cases with atomization gas velocity and larger droplets (Case 2 and Case 5). This is because the turbulence generated by the primary breakup during the atomization process of Case 3 and Case 6 (5 mm downstream of the pilot outlet) is weaker than that of Case 2 and Case 5 (5 mm upstream of the pilot outlet), but stronger than the flat ones. In addition, the difference disappears when the recess distance is increased from

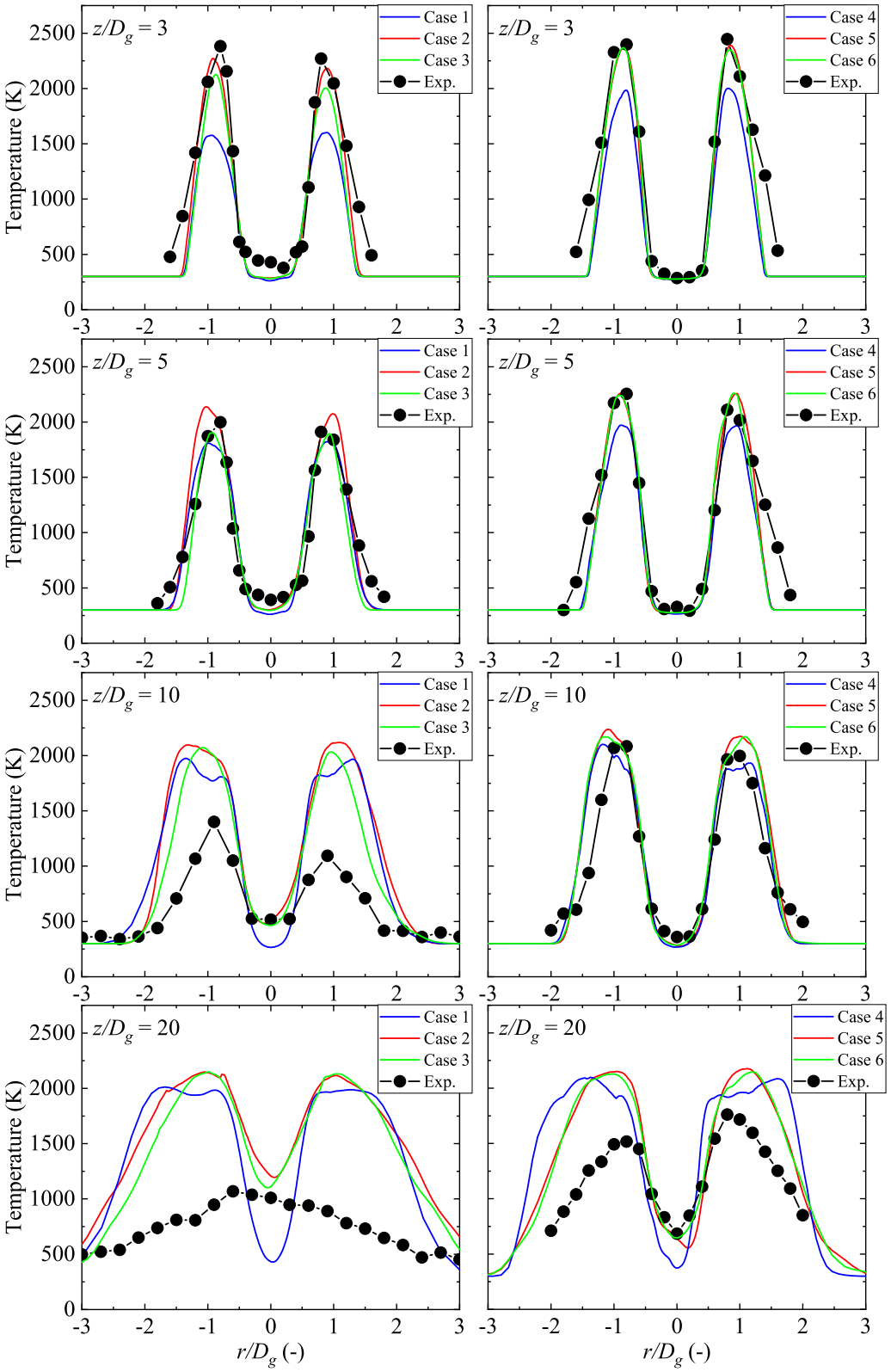

Figure 4.12: Comparison of radial distributions of time-averaged of gas temperature at different axial downstream locations of z/D_g = 3, 5, 10, and 20 between combustion simulation and experiment for Case 1-Case 6. Left is for dense spray and right is for dilute spray.

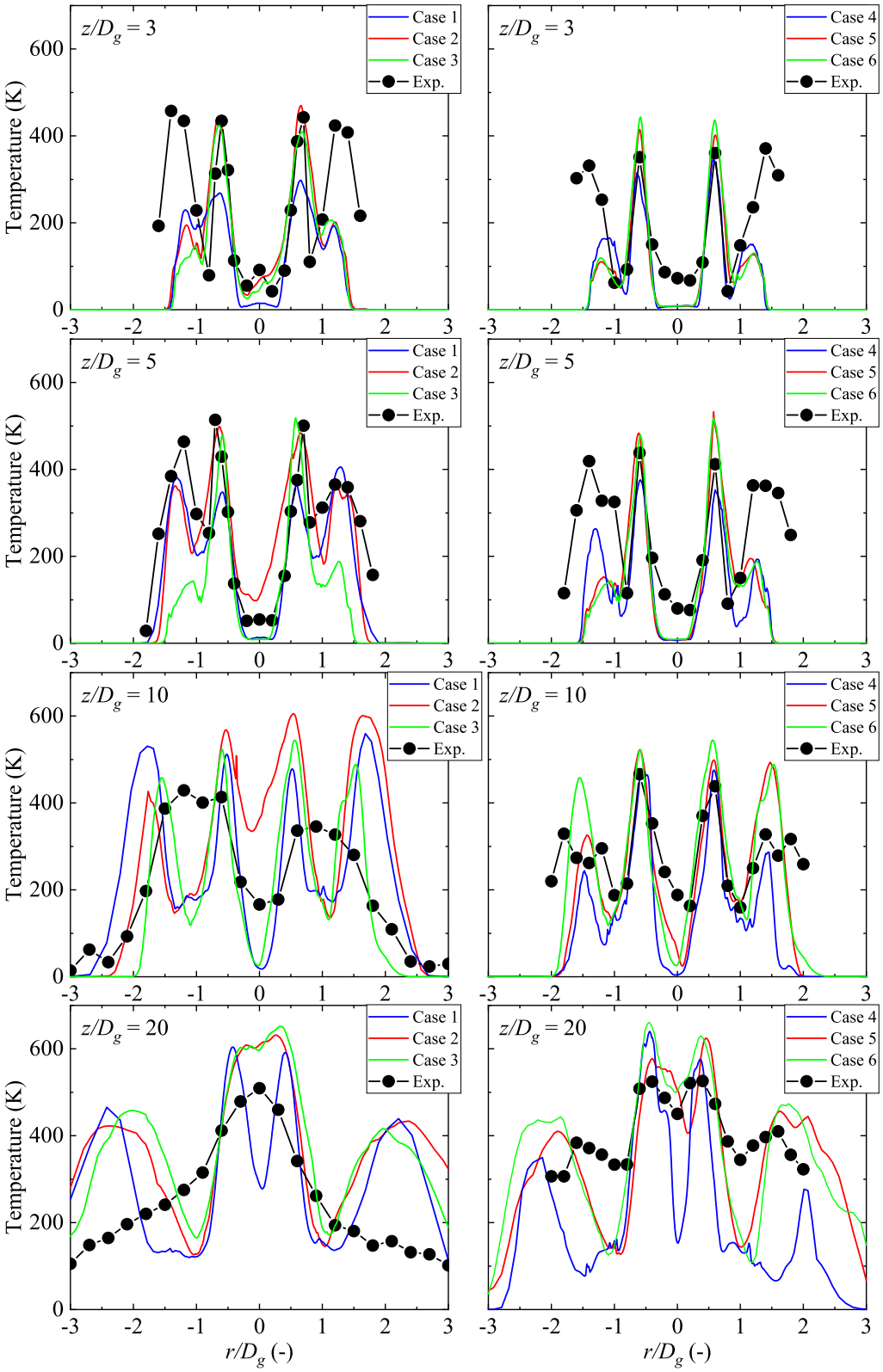

Figure 4.13: Comparison of radial distributions of RMS of gas temperature at different axial downstream locations of z/D_g = 3, 5, 10, and 20 between combustion simulation and experiment for Case 1-Case 6. Left is for dense spray and right is for dilute spray.

25 to 80 mm based on a comparison of the differences between a dense spray (Case 2 and Case 3) and a dilute spray (Case 5 and Case 6) because the ACCs, where the turbulence in the atomization computation is recorded, are 5 mm upstream and 5 mm downstream of the pilot outlet for a dense spray, but are 60 and 50 mm upstream of the pilot outlet for a dilute spray, as shown in Fig. 4.10. Therefore, the difference in turbulence owing to different ACCs finally disappears at the pilot outlet for a dilute spray.

An obvious discrepancy is seen between the simulation results and the experimental data at the downstream location of $z/D_g = 20$ of a dense spray, where the temperatures of simulation are overpredicted. In contrast to which, in a dilute spray, the temperature profiles of simulation match those of experiment very well and only drift away at the downstream location of $z/D_g = 20$, which is still not that obvious compared to that in a dense spray. The good agreement in the upstream region is due to the well-controlled boundary conditions which are also the interest of the present study. In addition, a suitable flamelet model or a better combustion mechanism may help to improve the difference observed in the downstream region for the dilute spray. However, for the great discrepancy in the dense spray, the situation is totally different. According to the experiment [4], a speculation is proposed that the combustion is finished in the downstream location of $z/D_g = 20$ even there exists fuel droplets such that the temperature distribution does not present the symmetric unimodal distribution. On the other hand, the combustion is still happening in the simulation such that an overestimation as well as a totally different structure could be observed. The dense spray region has much more larger ligaments and irregular shaped objects that cannot be consumed, and those larger liquid components generated by the primary breakup easily cause more unpredicted turbulence when they flow downstream and breakup into smaller droplets. Therefore, the local flow field is extremely unstable in the downstream region, which is different from the upstream region where the disturbances of those ligaments and irregular shaped objects have not developed. Therefore, the burning process might not occur much or just be finished, while the fuel is still present there, resulting in a lower local temperature distribution. However, in the present simulation, the larger ligaments and

irregular shaped objects are just simply transformed into Lagrangian droplets, failing to consider the realistic interaction between the gas phase and liquid fuel, as well as the further breakup behavior. Therefore, the Lagrangian droplets continue to be consumed when they reach further downstream, ensuring a continuous burning without any negative influences on the combustion, and thus a higher temperature distribution could be observed. However, the unstable flow field caused by those ligaments and irregular shaped objects may have significant influences on the fuel droplet evaporation and fuel vapor heat release. Another possibility is that the larger ligaments and irregular shaped objects tend to disperse further in the radial direction and thus the heavier ligaments and irregular shaped objects finally fall when they flow out of the flame zones. However, the total energy of the simulation is conserved such that the temperature distribution of the experiment is lower than that of the simulation.

The profiles of the RMS of gas temperature show a twin peak on the both sides of the centerline until $z/D_g = 10$, which is less distinct for the dense case. This twin peak structure is also well-captured by the present study for all six cases, and the Case 3 and Case 6 still have the intermediate values. The computational results show a reasonable match with the experiments near the center axis, and some discrepancies away from the center axis. In the experiment work, the temperature is strongly affected by the pilot flame in the outer space, such that the temperature distribution out of -1.25$\leqslant$ r/D_g $\leqslant$1.25, outside the edge of the pilot flame, presents some discrepancies. In addition, owing to the larger ligaments and irregular shaped objects mentioned in the last paragraph, it is difficult to capture the accurate temperature distributions in the dense spray cases. Therefore, the discrepancies tend to become eliminated when the recess distance is increased from 25 to 80 mm around the nozzle centerline from $r/D_g = -1$ to $r/D_g = 1$, except for the location at $z/D_g = 20$, where the combustion of dense spray in the experiment is considered to be completed.

Figs. 4.14 and 4.15 show the distributions of the time-averaged and RMS of gas temperature until the downstream location of $z/D_g = 50$ for all six cases. It can be seen that, compared to the results on the assumption of a uniform inlet boundary condition,

the use of inlet velocities determined from the atomization computation can enhance the mixing and establish the combustion at the most upstream locations. On the other hand, the profiles of the fluctuating temperature indicate that the differences of droplets in databases A1 and A4 may not have a significant influence on the combustion characteristics when comparing Case 2 and Case 3 as well as Case 5 and Case 6. In addition, the symmetrical flame structures in all cases prove that the droplet databases sampled from the atomization computation have no biases in any directions. This confirms that the proposed sampling method coupling the atomization and combustion computations is successful.

Fig. 4.16 shows the streamwise distributions of the time-averaged droplet sizes (D_{32} and D_{10}) and gas temperature of Case 3 and Case 6 at different radial locations of $r/D_g = 0$, 0.4, and 0.6 in comparison with the experiment results. Due to the limitation of the experiment measurement of Phase Doppler Anemometry (PDA), the measured droplet size is limited to 100 µm. Therefore, the calculations of D_{32} and D_{10} omit the Lagrangian droplets with a diameter of larger than 100 µm. However, the droplet size distributions between simulation and experiment still show large discrepancies, and the discrepancies might result from two reasons from the views of simulation and experiment. From the view of simulation, the E-L transformation utilized in the present study might improperly transform the larger ligaments and irregular shaped objects into Lagrangian droplets leading to an increment in droplet size. From the view of experiment, the PDA has severe criterion to measure sphere droplets and most sphere droplets holds relatively smaller diameter to maintain the shape, which leads to a decrease in droplet size. However, there are still some shared properties for the droplet size in simulation and experiment. Both D_{32} and D_{10} increase from center to side despite increasing the recess distance from 25 to 80 mm. For the dense spray, the D_{32} values increase slightly further downstream from z/D_g = 0.4-20, whereas for the dilute spray, the D_{32} values decrease slightly from z/D_g = 10-20, which also match the experiment results at the radial locations of $r/D_g = 0.4$ and 0.6. The D_{10} values of the simulation keep increasing in a dense spray and keep fluctuating in a dilute spray, whereas the D_{10} values of the

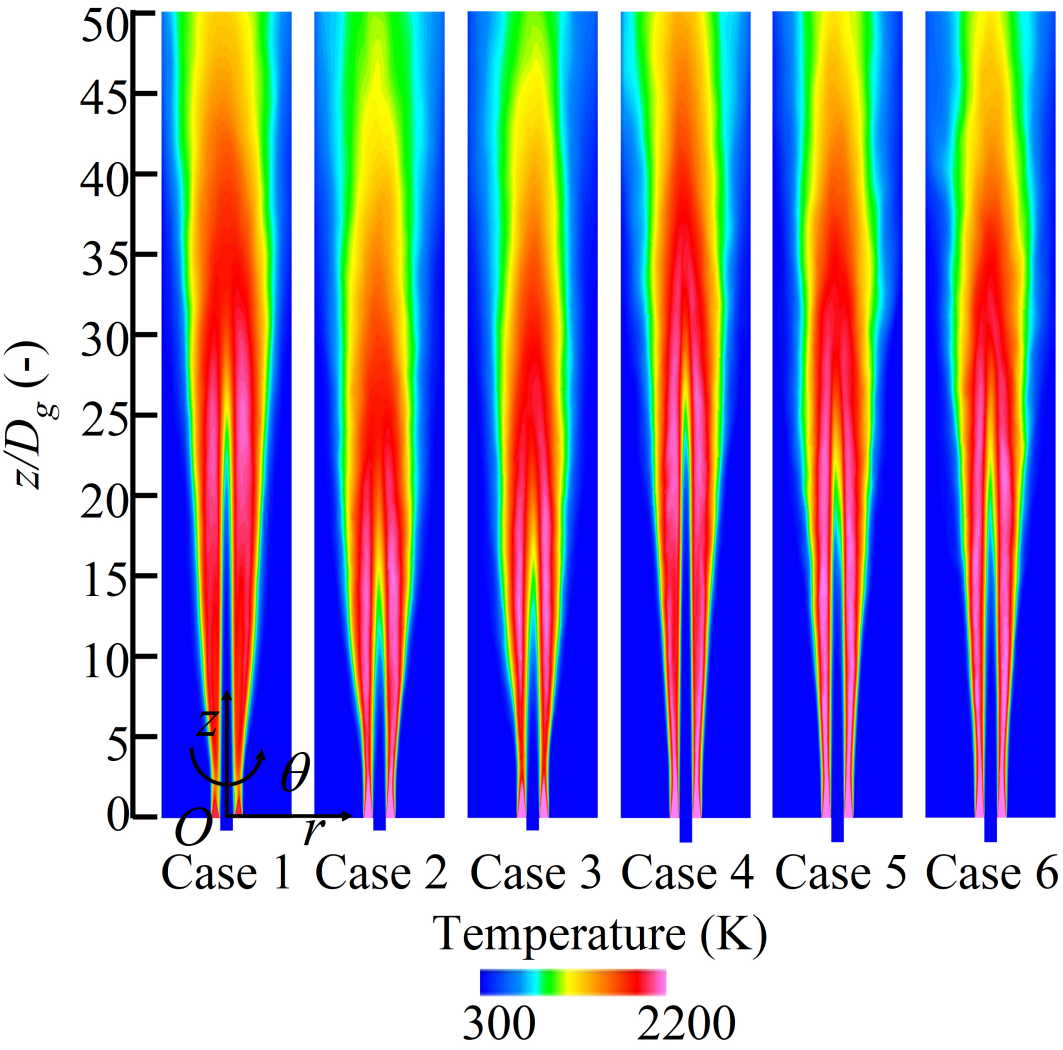

Figure 4.14: Comparison of distribution of time-averaged of gas temperature for Case 1-Case 6.

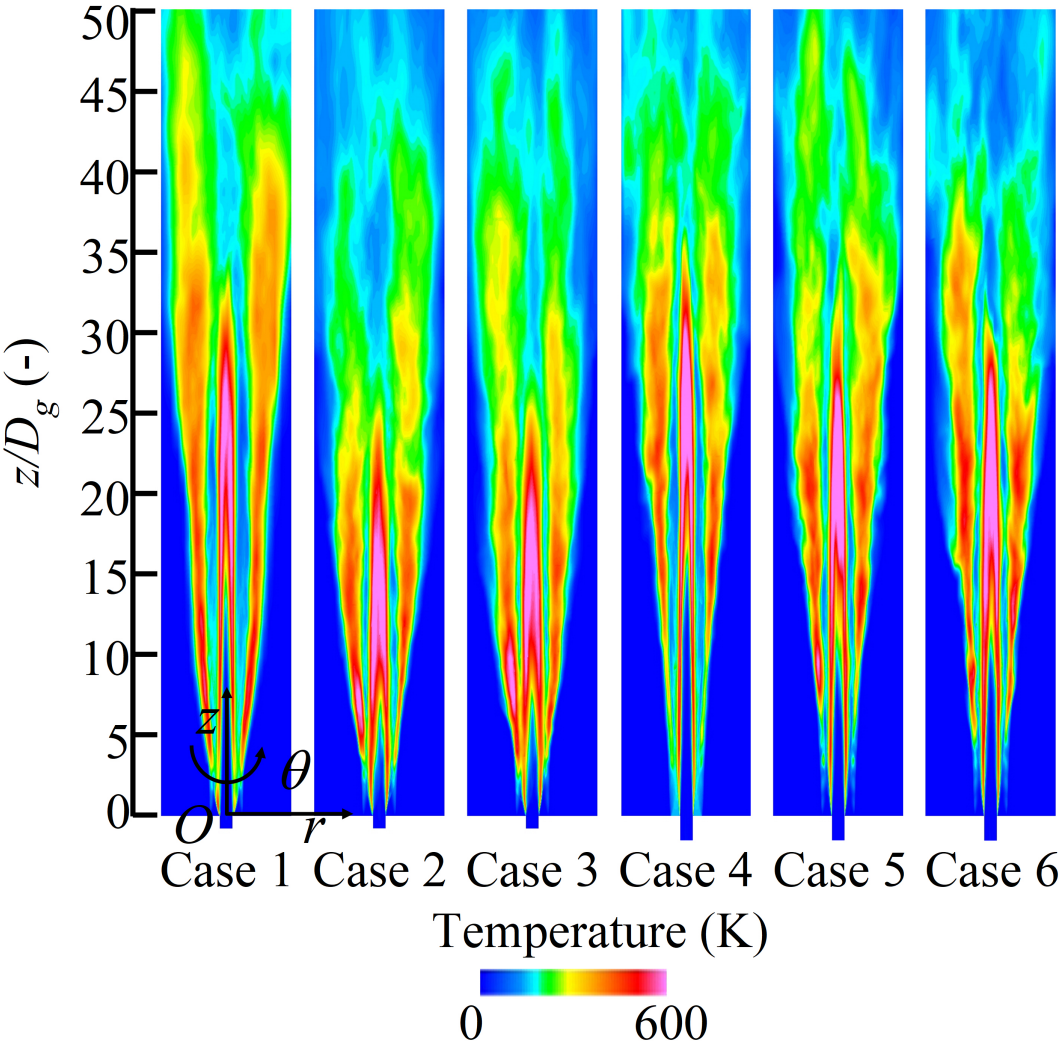

Figure 4.15: Comparison of distribution of RMS of gas temperature for Case 1-Case 6.

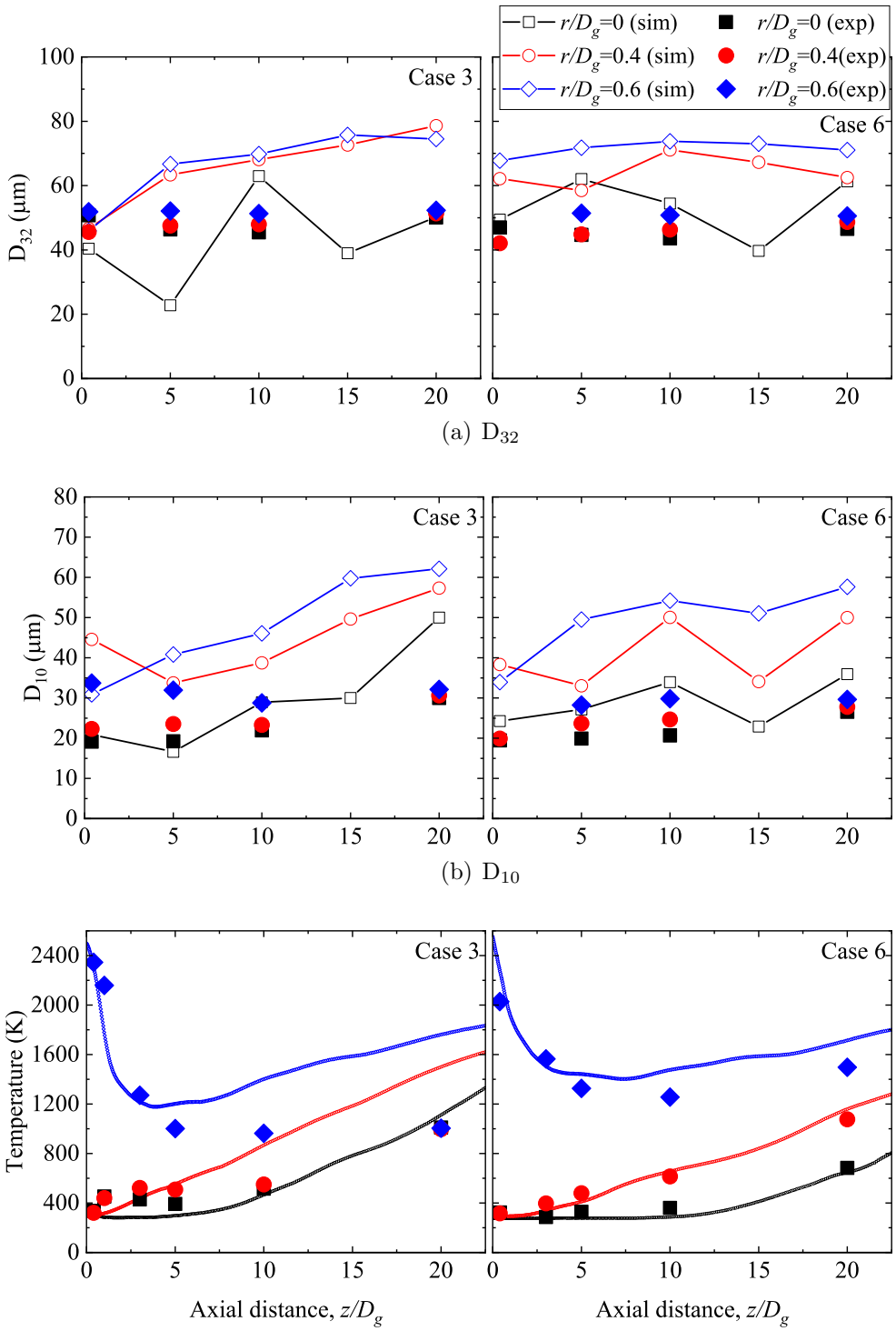

Figure 4.16: Comparison of streamwise distributions of time-averaged droplet sizes (D_{32} and D_{10}) and gas temperature at different radial locations of r/D_g = 0, 0.4, and 0.6 between combustion simulation and experiment for Case 3 and Case 6. Only droplets diameter less than 0.1mm are counted.

experiment keep fluctuating in a dense spray and keep increasing in a dilute spray. This opposite development is considered to be a result of omitting the larger Lagrangian droplets artificially. Since D_{10} is more affected by the portion of small droplets, and the measured droplets in the experiment tend to hold smaller diameter whereas the transformed droplets in the simulation may hold larger diameter, hence it is difficult for the simulation to predict the D_{10} values. Regarding the temperature development along with the axial direction, the dilute spray is considered to have a good agreement with the experiment at different radial locations. Whereas, for the dense spray, even good agreement can be observed at the center axis, it fails to capture the downstream temperatures especially for the outer locations of $r/D_g = 0.6$. This is probably because of insufficiency of the consideration of effect of liquid ligaments and irregular shaped objects existing away from the center axis, as mentioned before.

4.5 Conclusions

In this study, a numerical framework which is a one-way coupling between a VOF simulation and a combustion simulation was proposed, and the validity was investigated for the dense spray flames. Atomization was simulated by a detailed high-resolution VOF simulation, in which both continuum gas and liquid phases were strictly solved in an Eulerian framework, and the Eulerian components of the liquid droplets were transformed into the Lagrangian droplets at a certain downstream cross-section, i.e., sampling cross-section, whose information was stored in the database. Then, the combustion process was solved by a LES/NAPFV adopting the pre-stored database of Lagrangian droplets (i.e., the position, size, and velocity of each droplet) as the inlet boundary conditions. Computations were validated against measurement made in the Sydney Piloted Needle Spray Burner, which can generate both dilute and dense spray flames by varying the recess distance from the liquid fuel jet nozzle to the pilot outlet.

1. Regarding the detailed high-resolution VOF simulation of liquid fuel atomization, the volume flux of the droplets at the exit of the nozzle fluctuates both temporally and spatially, indicating that there exist periods of breakup and non-breakup during the atomization process. The breakup period is found to be in good agreement with an existing empirical correlation, and that the larger droplets tend to disperse away from the central axis compared to the smaller droplets located close to the central axis.

2. Regarding the database of the Lagrangian droplets for the LES/NAPFV of spray flames, three factors, the location of the sampling cross-section, sampling time, and threshold value for an Eulerian-Lagrangian (E-L) transformation, for the droplet database sampling were found to strongly affect the properties of the Lagrangian droplets, and to be critical for the success of the use of the LES/NAPFV of present spray flames.

3. Regarding the LES/NAFPV of two flame cases with different recess distances, the gas temperature and droplet size distributions show good agreement with the

experiments. The spray flame with a longer recess distance, which represents a dilute spray, is considered to have a longer and wider premixed core than that with a shorter recess distance representing a dense spray. This behavior is believed to be due to the enhanced mixing between the evaporated fuel and oxidizer.

4. Regarding the discrepancy in the gas temperature between the simulation and experiment in the dense spray flame, the over-predictions are observed to become more evident when moving downstream. This is considered to be attributed to the fact that for the LES/NAFPV of the dense spray flame, the relatively large and non-spherical liquid components are regarded as the Lagrangian spherical droplets in the present E-L transformation, and therefore, their further breakup and influence on the turbulence development and flame evolution are neglected.

In summary, the numerical framework proposed in this study is capable of reproducing the spray atomization and the gas temperature distributions in dilute spray flames of Sydney Piloted Needle Burner with a relatively low computational cost and without any atomization model or presumed initial droplet size distribution. Some failures of gas temperature distributions in dense spray flames and droplet size distributions are discussed in detail which requires further investigations. The improvement of the E-L tagging method in generating droplet databases for relatively dense sprays merits future work.

Appendix A. Details of Chi square homogeneity check for droplet spatial distribution analysis

The homogeneity analysis for droplet spatial distribution is discussed in details. As mentioned in Section 4.2.2, the angle θ in the radial plane and the droplet size can be used to analyze the droplet spatial distribution. The space can be divided into four mathematical quadrants, i.e., $0 \leqslant \theta < \pi/2$, $\pi/2 \leqslant \theta < \pi$, $\pi \leqslant \theta < 3\pi/2$, and $3\pi/2 \leqslant \theta < 2\pi$, to check the preference in different radial directions, and the droplet size can be divided

into three clusters, i.e., 0-50 μm, 50-150 μm, and 150-300 μm to check the distance bias in a certain radial direction. The Chi-square homogeneity validation is a method generally used to analyze the data homogeneity in different clusters, and the data can be regarded as homogeneous if the accumulated value is satisfied. First, the degree of freedom for the Chi-square is calculated as $df = (\text{row} - 1) \times (\text{col} - 1)$, where df indicates the degree of freedom, row is the number of rows, with three droplet size clusters herein; col is the number of columns, i.e., the 4 mathematical quadrants, as shown in Table 3. Therefore, the degree of freedom is $df = (3 - 1) \times (4 - 1) = 6$. The critical value (with 95% confidence level) under a degree of freedom of 6 can be found to be 12.59 according to the statistics, which means that if the total value of all cells is less than 12.59, then the data can be confirmed to have a 95% possibility to ensure the azimuthal homogeneity of the droplet distribution. The calculation algorithm is very simple, which is briefly introduced. For the cell i in a certain row and column, there is a statistic F_i by counting the number of droplets which satisfy the conditions (i.e., droplet size and angle), and thus a total value of the row or column can be calculated. Based on the statistic of cell i and total values of rows and columns, the expected value of cell i could be calculated as E_i. Then, the total value of all cells, X^2, of one database can be calculated as $X^2 = \sum_{i=1}^{n}((E_i - F_i)^2/E_i^2)$. By using this Chi-square homogeneity check, if the total value is less than the critical value of 12.59, it can be said that the droplets are homogeneously distributed in the four mathematical quadrants ($0 \leqslant \theta < \pi/2$, $\pi/2 \leqslant \theta < \pi$, $\pi \leqslant \theta < 3\pi/2$, and $3\pi/2 \leqslant \theta < 2\pi$) with smaller droplets close to the center axis and larger droplets away from the center axial such that the database can be considered to have no special preferences existing in a specific direction.

References

[1] J.Shinjo. Recent advances in computational modeling of primary atomization of liquid fuel sprays. *Energies*, 11:2971, 2018.

[2] J. Gounder, A. Kourmatzis, and A. Masri. Turbulent piloted dilute spray flames: flow fields and droplet dynamics. *Combust. Flame*, 159:3372–3397, 2012.

[3] L. M. Thomas, A. Lowe, A. Satija, and A. Masri. Five khz thermometry in turbulent spray flames using chirped-probe pulse femtosecond cars, part i: Processing and interference analysis. *Combust. Flame*, 200:405–416, 2019.

[4] A. Lowe, L. Thomas, A. Satija, R. Lucht, and A. Masri. Five khz thermometry in turbulent spray flames using chirped-probe pulse femtosecond cars, part ii: Structure of reaction zones. *Combust. Flame*, 200:417–432, 2019.

[5] S. Tachibana, K. Saito, T. Yamamoto, M. Makida, T. Kitano, and R. Kurose. Experimental and numerical investigation of thermos-acoustic instability in a liquid-fuel aero-engine combustor at elevated pressure: validity of large-eddy simulation of spray combustion. *Combust. Flame*, 162:2621–2637, 2015.

[6] H. Moriai, R. Kurose, H. Watanabe, Y. Yano, F. Akamatsu, and S. Komori. Large-eddy simulation of turbulent spray combustion in a subscale aircraft jet engine combustor-predictions of no and soot concentrations. *J. Eng. Gas Turbines Power*, 135:091503, 2013.

[7] A. Kishimoto, H. Moriai, K. Takenaka, T. Nishiie, M. Adachi, A. Ogawara, and R. Kurose. Application of a non-adiabatic flamelet/progress-variable approach to large eddy simulation of h2/o2 combustion under a pressurized condition. *J. Heat Trans.*, 139:124501, 2017.

[8] J. Brackbill, D. Kothe, and C. Zemach. A continuum method for modeling surface tension. *J. Comput. Phys.*, 100:335–354, 1992.

[9] S. Muzaferija and M. Peric. Computation of free-surface flows using interface-tracking and interface-capturing methods. *Nonlinear Water Wave Interaction*, 59–100, 1998.

[10] A. Albadawi, D. Donoghue, A. Robinson, D. Murray, and Y. Delauré. Influence of surface tension implementation in volume of fluid and coupled volume of fluid with level set methods for bubble growth and detachment. *Int. J. Multiphas. Flow*, 53:11–28, 2013.

[11] M. Herrmann. A parallel eulerian interface tracking/lagrangian point particle multi-scale coupling procedure. *J. Comput. Phys.*, 229:745–759, 2010.

[12] D. Zuzio, J. Estivalèzes, and B. DiPierro. An improved multiscale eulerian-lagrangian method for simulation of atomization process. *Comput. Fluids*, 176:285–301, 2018.

[13] T. Kitano, K. Kaneko, R. Kurose, and S. Komori. Large-eddy simulations of gas- and liquid-fueled combustion instabilities in back-step flows. *Combust. Flame*, 170:63–78, 2016.

[14] Y. Hu and R. Kurose. Nonpremixed and premixed flamelets les of partially premixed spray flames using a two-phase transport equation of progress variable. *Combust. Flame*, 188:227–242, 2018.

[15] Y. Hu, R. Kai, R. Kurose, E. Gutheil, and H. Olguin. Large eddy simulation of a partially pre-vaporized ethanol reacting spray using the multiphase dtf/flamelet model. *Int. J. Multiphas. Flow*, 125:103216, 2020.

[16] C. Pierce and P. Moin. Progress-variable approach for large-eddy simulation of non-premixed turbulent combustion. *J. Fluid Mech.*, 504:73–97, 2004.

[17] N. Lallemant, A. Sayre, and R. Weber. Evaluation of emissivity correlations for h_2o-co_2-n_2/air mixtures and coupling with solution methods of the radiative transfer equation. *Prog. Energy Combust.*, 22:543–574, 1996.

[18] H. Pitsch and H. Steiner. Large-eddy simulation of a turbulent piloted methane/air diffusion flame (sandia flame d). *Phys. Fluids*, 12:2541, 2000.

[19] D. Lilly. A proposed modification of the germano subgridscale closure method. *Phys. Fluids A*, 4:633–635, 1992.

[20] C. Crowe, M. Sharma, and D. Stock. The particle-source-in cell (psi-cell) model for gas-droplet flows. *J. Fluid Eng. Trans. Asme*, 99:325–332, 1977.

[21] R. Miller, K. Harstad, and J. Bellan. Evaluation of equilibrium and non-equilibrium evaporation models for many-droplet gas-liquid flow simulations. *Int. J. Multiphas. Flow*, 24:1025–1055, 1998.

[22] H. Watanabe, R. Kurose, S. Huang, and F. Akamatsu. Characteristics of flamelets in spray flames formed in a laminar counterflow. *Combust. Flame*, 148:234–248, 2007.

[23] R. Kurose, H. Makino, S. Komori, M. Nakamura, F. Akamatsu, and M. Katsuki. Effects of outflow from the surface of a sphere on drag, shear lift, and scalar diffusion. *Phys. Fluids*, 15:2338–2351, 2003.

[24] J. Wen, Y. Hu, A. Nakanishi, and R. Kurose. Atomization and evaporation process of liquid fuel jets in crossflows: A numerical study using eulerian/lagrangian method. *Int. J. Multiphas. Flow*, 103331, 2020.

[25] T. Kitano, J. Nishio, R. Kurose, and S. Komori. Evaporation and combustion of multicomponent fuel droplets. *Fuel*, 136:219–225, 2014.

[26] T. Kitano, J. Nishio, R. Kurose, and S. Komori. Effects of ambient pressure, gas temperature and combustion reaction on droplet evaporation. *Combust. Flame*, 161:551–564, 2014.

[27] P. O'Rourke and A. Amsden. The tab method for numerical calculation of spray droplet breakup. *SAE paper*, 872089, 1987.

[28] H. Pitsch. Flamemaster: A c++ computer program for 0d combustion and 1d laminar flame calculations. 81, 1998.

[29] S. Pichon, G. Black, N. Chaumeix, M. Yahyaoui, J. Simmie, H. Curran, and R. Donohue. The combustion chemistry of a fuel tracer: Measured flame speeds and ignition delays and a detailed chemical kinetic model for the oxidation of acetone. *Combust. Flame*, 156:494–504, 2009.

[30] S. Elghobashi. Particle-laden turbulent flows: direct simulation and closure models. *Appli. Sci. Res.*, 301–314, 1991.

[31] J.-P. Matas, S. Marty, and A. Cartellier. Experimental and analytical study of the shear instability of a gas-liquid mixing layer. *Phys. Fluids*, 23:094112, 2011.

[32] J.-P. Matas, A. Delon, and A. Cartellier. Shear instability of an axisymmetric air-water coaxial jet. *J. Fluid Mech*, 843:575–600, 2018.

Nomenclature

B_M : Mass transfer number [-]
c_p : Specific heat capacity [J/(K kg)]
C : Progress variable [-]
d : Droplet diameter [m]
D : Diffusion coefficient [m^2/s]
f : Frequency [Hz]
f_1 : Correction of Stokes drag [-]
f_2 : Correction of heat transfer [-]
$F_{\boldsymbol{\sigma}}$: Body force of surface tension [N]
h : Enthalpy [J/kg]
$\boldsymbol{g}$: Gravity [N]
L_V : Latent heat [J/kg]
m : Mass [kg]
N : Number of droplets in a grid [-]
Nu : Nusselt number [-]
P : Pressure [Pa]
Pr : Prandtl number [-]
q : subgrid-scale scalar flux [-]
Q_{rad} : Radiation heat loss [-]
Re : Reynolds number [-]
S : Distance of neighboring droplets [m]
$\boldsymbol{S}$: Rate-of-strain tensor [-]
Sc : Schmidt number [-]
Sh : Sherwood number [-]
t : Time [s]
T : Temperature [K]
u : Axial velocity [m/s]
$\boldsymbol{u}$: Velocity [m/s]
α : Heat loss rate parameter [-]
α_t : Eddy diffusivity [-]
δ : Thickness of vorticity layer [m]
λ : Thermal conductivity [W/(m K)]
μ : Viscosity [Pa s]
ρ : Density [kg/m^3]
σ : Surface tension [N/m]
τ : Response time [s]
$\boldsymbol{\tau}$: Stress tensor [N/m^2]
φ : Flamelet library [-]
χ : Scalar dissipation rate [-]
ψ : VOF function [-]
$\dot{\omega}$: Reaction rate [-]
$\dot{\omega}_C$: Source term of progress variable [1/s]

Subscripts

0 : Initial value
d : Droplet's value
F : Fuel
g : Gas phase value
k : Chemical species k
l : Liquid phase value
m : Compressive value
s : Droplet surface
sgs : Subgrid-scale value
t : turbulent value

Symbols

$-$: Filtered mean value
$\sim$: Favre averaged value

v : Radial velocity [m/s]

V : Volume [m^3]

W : Mole weight [kg/mol]

$\boldsymbol{x}$: Position [m]

Y : Mass fraction [-]

Z : Mixture fraction [-]

Chapter 5

Conclusions

5.1 Summary and conclusions

To investigate the liquid jet atomization, droplet evaporation, and fuel combustion in liquid fuel spray combustion, detailed numerical simulations of the atomization–evaporation process of liquid fuel jets in both steady and oscillating crossflows, and a LES of turbulent dense spray flame coupled with a detailed high-resolution VOF simulation of liquid fuel atomization, were performed.

In Chapter 2, the characteristics of the atomization–evaporation behaviors of liquid fuel jets in steady crossflows under elevated ambient pressure were described. The liquid jet trajectory, primary breakup behavior of the liquid jet, vortex development and morphology, droplet size distribution, and evaporation effects under different breakup mode regimes (i.e., different aerodynamic Weber number conditions) were investigated using a detailed numerical simulation. As the liquid fuel jet, kerosene was used. As the gas of crossflow, air was used under an elevated ambient pressure of 3.0 MPa, which is close to the practical condition of an aircraft engine [1]. For the calculation of the atomization–evaporation process, a CLSVOF method was used to capture the liquid–gas interface, and the CSF model proposed by Brackbill et al. [2] was used to calculate the surface tension of the liquid–gas interface. An E-L tagging method that transforms Eulerian droplets into Lagrangian droplets, proposed by Herrmann [3] and Zuzio et al. [4],

was utilized to reduce the computational cost. A non-equilibrium Langmuir-Knudsen evaporation model was used to consider the evaporation effects of the transformed Lagrangian droplets.

In Chapter 3, the characteristics of the atomization–evaporation behaviors of a liquid fuel jet in an oscillating crossflow under an elevated ambient pressure in comparison with that in a steady crossflow were described. The liquid jet trajectory, vortex development and morphology, droplet size distribution, and fuel vapor distribution in the oscillating crossflow were investigated using a detailed numerical simulation. For the oscillating crossflow, the oscillation frequency was set to 500 Hz, which is similar to a previous study on combustion instability [1]. The physical properties of the liquid fuel and carrier crossflow are the same as those in the steady crossflow, and so are the numerical simulation method and settings.

In Chapter 4, the characteristics of the atomization–combustion behaviors of liquid fuel jets in the configuration of Sydney Burner under atmospheric pressure in comparison with the experimental data were described. Acetone and air at atmospheric pressure were used as the fuel and oxidizer, respectively. For the calculation of atomization, an HRIC scheme was implemented in the VOF method to capture the liquid–gas interface. For the calculation of combustion, an NAFPV was used to model the turbulence–chemistry interaction. For the coupling of atomization–combustion computation, the ACC plane was used to save the output of the atomization computation (i.e., the profiles of the transformed Lagrangian droplet and gas velocity) in a database and serve as inlet boundary conditions for the combustion computation.

The main results obtained in this study can be summarized as follows:

1. For the atomization–evaporation process of liquid fuel jets in steady crossflows under elevated ambient pressure. The primary atomization characteristics were reproduced by the present simulation using the CLSVOF method and were strongly affected by the circulation flows generated behind the liquid jet, namely, the bag breakup vortex (BBV) and the shear breakup vortex (SBV). With an increase in the aerodynamic Weber number, the SBV takes the dominant position to pose

more shear breakup than bag breakup, leading to a smaller Sauter mean diameter in the downstream region such that the bag mode regime is shifted to the shear mode regime. In the case of the bag mode regime, the droplets mainly generated by bag breakup are directly transported downstream by the BBV, and thus the liquid jet tip has a higher evaporation rate. In addition, distinct bifurcations can be observed in this situation. In the case of the multimode and shear mode regimes, the SBV is enhanced to transport the droplets generated in the upper regions into the regions in the vicinity of the wall; thus, the region near the wall has a higher evaporation rate. In addition, the SBV traps a large amount of fuel vapor just behind the liquid jet, suppressing the evaporation effect.

2. For the atomization–evaporation process of a liquid fuel jet in an oscillating crossflow under elevated ambient pressure. The breakup behavior, liquid jet trajectory, droplet size, and fuel vapor distributions in the downstream region have the same frequency as the oscillating crossflow. The former three properties also respond to the crossflow velocity rapidly; in contrast, the fuel vapor distribution tends to have a half-period time delay. The droplet size distributions, D_{32} and D_{10}, show converse changes because of the SBV behind the jet. For the phase with a higher aerodynamic Weber number, the SBV is enhanced to hold more droplets circulating there, resulting in a high evaporation rate. Therefore, smaller droplets are consumed in advance, leading to a larger D32 and smaller D10 in the downstream region. On the other hand, an enhanced SBV traps more fuel vapor, and thus the weakened SBV could send more fuel vapor out of the domain such that the value of fuel vapor in the downstream region appears a half-period time delay. The smaller mean values of D_{32} and D_{10} , as well as the larger mean value of fuel vapor in the downstream region of the oscillating crossflow compared to those of the steady crossflow, suggest a better atomization–evaporation property.

3. For the atomization–combustion process of liquid fuel jets in the configuration of Sydney Burner under atmospheric pressure. The atomization behaviors were re-

produced by the present simulation using the VOF method and found to fluctuate both temporally and spatially with periods of breakup and non-breakup. In addition, larger droplets tend to be located away from the central axis compared to the small droplets located near the central axis. Three factors—the location of the sampling cross section, sampling time, and threshold value for an E-L tagging method—were found to strongly affect the properties of the Lagrangian droplets and to be critical for the success of the present spray flames. Both dense and dilute spray flames show good agreement with the experiments in terms of the gas temperature and droplet size distributions, except for the downstream region of dense spray flames, where the gas temperature distributions are over-predicted. This is attributed to the fact that the relatively large and non-spherical liquid components are regarded as Lagrangian spherical droplets without considering further breakup and detailed turbulence development as well as flame evolution.

5.2 Suggestions for future research

Conducting research into the following areas could extend the progress made in the current study:

1. In Chapter 2, the atomization–evaporation process of liquid fuel jets in steady crossflows was investigated under elevated ambient pressure through a detailed numerical simulation. To further understand the cross-flow atomization–evaporation process, it is important to investigate and clarify the evaporation process at the liquid–gas interface to accurately capture the fuel vapor for the combustion process.

2. In Chapter 3, the atomization–evaporation process of a liquid fuel jet in an oscillating crossflow was investigated under elevated ambient pressure using a detailed numerical simulation. However, a detailed numerical simulation was performed by assuming that the gas phase is an incompressible fluid without considering the compressibility of the gas phase, resulting from combustion instability. Therefore, a weakly compressible scheme is required for simulating liquid jet atomization in a subsonic crossflow.

3. In Chapter 4, the atomization–combustion process of liquid fuel jets in the configuration of Sydney Burner was investigated under atmospheric pressure. However, the E-L tagging method could not accurately capture the large and non-spherical Eulerian liquid components in the dense spray region. Therefore, it is important to capture more details of irregular liquid components in the atomization computation such that a detailed breakup and turbulence development could be acquired. The VOF method with higher momentum conservation at the liquid–gas interface and less numerical diffusion with the topology scheme is urgent for dense spray flame simulation.

References

[1] S. Tachibana, K. Saito, T. Yamamoto, M. Makida, T. Kitano, and R. Kurose. Experimental and numerical investigation of thermos-acoustic instability in a liquid-fuel aero-engine combustor at elevated pressure: validity of large-eddy simulation of spray combustion. *Combust. Flame*, 162:2621–2637, 2015.

[2] J. Brackbill, D. Kothe, and C. Zemach. A continuum method for modeling surface tension. *J. Comput. Phys.*, 100:335–354, 1992.

[3] M. Herrmann. Detailed numerical simulations of the primary atomization of a turbulent liquid jet in crossflow. *J. Eng. Gas Turbines Power*, 132:061506, 2010.

[4] D. Zuzio, J. Estivalèzes, and B. DiPierro. An improved multiscale eulerian-lagrangian method for simulation of atomization process. *Comput. Fluids*, 176:285–301, 2018.